Mark formation model for optical rewritable recording

PROEFSCHRIFT

ter verkrijging van de graad van doctor
aan de Technische Universiteit Delft,
op gezag van de Rector Magnificus prof.dr.ir. J.T. Fokkema,
voorzitter van het College voor Promoties, in het openbaar te verdedigen
op dinsdag 27 februari 2007 om 10:00 uur

door

Johannes Hermanus BRUSCHE
wiskundig ingenieur

geboren te Leiden

Summary

Mark formation model for optical rewritable recording

Johannes Hermanus Brusche

After more than two decades, the success of optical storage media is undeniable. Blockbuster movies in high definition resolution, high quality audio recordings of thousands of renowned artists, next-generation console and computer games: the modern consumer market is flooded with state-of-the-art digitalized media, stored on a 12 cm diameter disc, which is read out via an optical readout system.

It all started back in 1982 with the introduction of the audio compact disc as the replacement of the vinyl gramophone record. Since then, as technology advanced and the demand for larger storage space increased, the proved concept of the compact disc has led to several successors, among which are the digital versatile disc (DVD) and the Blu-ray disc.

Besides prerecorded read-only discs, there also exist write-once and rewritable versions for each optical storage format. In contrary to prerecorded discs, the surface of recordable and rewritable discs contains an outward spiraling groove. This groove is needed to guide the laser beam during recording. Furthermore, these discs consist of various layers. High power laser pulses are applied to locally alter the material properties of a specific material contained in one of these layers. For write-once discs, the active recording layer consists of a organic dye material, which locally decomposes as a result of the laser light. For rewritable discs, the recording layer contains a so-called phase-change material. Inside the phase-change layer, the laser pulses cause amorphous regions to be formed in the crystalline background. These regions are called marks. The same laser, but at a reduced power level, can be used to initiate a recrystallization of the amorphous regions, thereby erasing the recorded data.

In this dissertation a numerical model is proposed for the melting com-

ponent of the mark formation process in optical phase-change recording. That is, latent heat is taken into account, but the effects of recrystallization are not embedded in the current model. Even though, in general, phase-change materials are alloys, and thus melt along a melting trajectory, we assume that melting occurs at a melting point. However, the presented model is formulated such, that it can be extended to so-called mushy region problems without much effort.

The temperature distribution in the recording stack, at any given instance during the recording process, can be numerically obtained by solving a time dependent heat diffusion problem for the temperature. As long as the maximum temperature does not exceed the melting temperature of the phase-change material, this exercise is rather straightforward, even inside a complex composite domain, such as a recording stack. However, as soon as the melting temperature is exceeded somewhere inside the computational domain, an interface separating the liquid and solid material is introduced. This interface is exactly where the latent heat comes into the equation: at the interface position, the temperature remains fixed at the melting temperature, until all the energy required to complete the phase transition, i.e., the latent heat, is used up. As such, not only a new unknown is introduced to the mathematical formulation (the interface position), but in addition, the problem has become highly nonlinear.

A broad spectrum of numerical methods for resolving these so-called Stefan problems is available from the literature. Nonetheless, only a limited number of these methods are potentially adaptable to our particular problem formulation, due to stringent requirements that are essential to perform 'realistic' recording simulations. Besides that the method should be applicable to three-dimensional complex composite domains, it should also be robust. Moreover, the method has to be able to capture multiple separate moving fronts and the balance between accuracy and computational load should be feasible.

In this work, a temperature based method, in which the temperature is the single dependent unknown, is shown to be the most suitable approach. The key feature of the particular temperature based method that we apply, is that, within a finite element framework, the integrals over an element undergoing phase-change are taken to be equal to the sum of the individual contributions from the solid and liquid subdomains this element contains. Because in general no explicit regularization of the enthalpy function is carried out, the energy balance in the weak form is exactly satisfied in discrete sense.

The finite element meshes, that are required to ensure an accurate resolution of the approximated temperature field, consist of millions of elements for most industrially relevant simulations. Intuitively, the element density is preferably the highest near the moving interface. Therefore, an adaptive local mesh refinement procedure has been added to the melting model. In

this way, besides that the position of the moving interface is resolved more rigorously, computer memory can be utilized more efficiently.

Finally, several results are presented for DVD and Blu-ray recording simulations. Of special interest are the effects of the polarization of the incident light and the stack configuration on the shape and size of the region that melts due to a laser pulse. Moreover, it is investigated under which circumstances latent heat can be important for the modeling of the recording process.

Samenvatting

Markformatie model voor optisch herschrijfbare dataopslag

Johannes Hermanus Brusche

Na ruim twee decennia is het succes van optische dataopslagmedia onmiskenbaar. *Blockbuster* films in *high definition* resolutie, hoge kwaliteit geluidsopnames van duizenden beroemde artiesten, *next-generation* spelcomputer en pc-spellen: de hedendaagse consumptiemaatschappij wordt overspoeld met vooruitstrevende gedigitaliseerde media, vastgelegd op een schijfje van 12 cm diameter, welke uitgelezen wordt via een optisch leessysteem.

Het begon allemaal in 1982 met de introductie van de audio *compact disc* ter vervanging van de grammofoonplaat van vinyl. Sindsdien, terwijl de technologie vooruitging en de vraag naar meer opslagcapaciteit toenam, heeft het concept van de *compact disc* zichzelf bewezen en geleid tot verscheidene opvolgers, zoals de *digital versatile disc* (DVD) en de Blu-ray disc.

Naast geperste schijfjes, die enkel zijn uit te lezen, bestaan er voor ieder optisch opslagformaat ook schijfjes die eenmalig of meerdere malen zijn te beschrijven. In tegenstelling tot geperste schijfjes bevat een eenmalig of meerdere malen te beschrijven schijfje een spiraalvormige groef. Deze groef is noodzakelijk om tijdens het opnameproces de laserbundel te sturen. Daarnaast zijn deze schijfjes opgebouwd uit verschillende lagen. Laserpulsen met een hoog vermogen worden gebruikt om lokaal de materiaaleigenschappen in een van deze lagen te veranderen. In eenmalig beschrijfbare schijfjes bestaat de actieve opnamelaag uit een zogenaamde organische kleurstof, die uiteenvalt ten gevolge van het laserlicht. In herschrijfbare schijfjes bevat de opnamelaag een zogeheten faseovergangsmateriaal. In de laag die dit materiaal bevat vormen zich amorfe gebiedjes in de kristallijne achtergrond door toedoen van de laserpulsen. Deze gebiedjes worden '*marks*' genoemd. Met behulp van dezelfde laser, echter met

een gereduceerd vermogen, kan een rekristallisatie van de amorfe gebiedjes worden bewerkstelligd, waardoor de geschreven data kan worden gewist.

In deze dissertatie wordt een numeriek model voorgesteld voor de smeltcomponent van het vormingsproces van een *mark* in optische data-opslag op basis van een faseovergang. Dit betekent dat de latente warmte wel wordt meegenomen in het model, maar dat de effecten van rekristallisatie niet worden meegenomen in het huidige model. En alhoewel faseovergangsmaterialen in het algemeen legeringen zijn, en dus smelten over een smelttraject, nemen we aan dat smelten plaatsvindt op een smeltpunt. Niettemin is het gepresenteerde model zodanig geformuleerd, dat het zonder veel inspanning kan worden uitgebreid om toegepast te kunnen worden op zogenaamde *mushy region* problemen.

De temperatuurverdeling in de opnamelaag kan op ieder willekeurig moment tijdens het schrijfproces numeriek worden bepaald door een tijdsafhankelijke warmtediffusievergelijking op te lossen. Zolang de maximale temperatuur de smelttemperatuur van het faseovergangsmateriaal niet overschrijdt, is deze exercitie vrijwel rechttoe-rechtaan, zelfs voor een complex en samengesteld domein, zoals de gelaagde structuur van een herschrijfbaar schijfje. Echter, zodra ergens in het rekendomein de smelttemperatuur wordt overschreden, zal zich een grenslaag vormen die het vaste en het vloeibare materiaal scheidt. Dit is precies waar de latente warmte van belang is: daar waar de grenslaag zich bevindt zal de temperatuur op de smelttemperatuur blijven hangen totdat alle energie die voor de faseovergang noodzakelijk is, dat wil zeggen, de latente warmte, op gebruikt is. Als zodanig wordt niet alleen een nieuwe onbekende aan de wiskundige formulering toegevoegd (de positie van de grenslaag), maar het probleem wordt bovendien sterk niet-lineair.

Een breed scala aan numerieke methoden voor het oplossen van deze zogeheten Stefan problemen is in de literatuur te vinden. Niettemin is slechts een beperkt aantal methoden daadwerkelijk toepasbaar op het door ons geformuleerde probleem. Dit is te wijten aan de stringente eisen, die essentieel zijn om 'realistische' simulaties van het schrijfproces uit te voeren. Zo moet de methode niet alleen toepasbaar zijn voor driedimensionale complexe samengestelde domeinen, ze moet ook robuust zijn. Bovendien moet de methode in staat zijn om verscheidene verschillende bewegende randen te onderscheiden en er moet een evenwichtige balans zijn tussen nauwkeurigheid enerzijds en de rekenlast anderzijds.

In dit werk laten we zien dat een methode waarin de temperatuur de enige afhankelijke variabele is, de voorkeur heeft. De meest kenmerkende eigenschap van de door ons toegepaste methode is dat, binnen het raamwerk van de eindige elementen methode, de integralen over een element dat een faseovergang ondergaat, gelijk gesteld worden aan de som van de individuele bijdragen van de integralen over de vaste en vloeibare deelgebieden van dit element. Omdat in het algemeen geen expliciete regularisatie

van de enthalpiefunctie plaatsvindt, wordt in discrete zin exact aan de energiebalans in de zwakke formulering voldaan.

Het eindige elementen rooster, dat nodig is om een nauwkeurige benadering van het temperatuurveld te garanderen, bestaat voor de meeste industrieel relevante simulaties uit miljoenen elementen. Intuïtief gezien is de elementdichtheid bij voorkeur het hoogst in een omgeving van de bewegende grenslaag. Daarom is een adaptieve lokale verfijningsprocedure toegevoegd aan het smeltmodel. Hierdoor kan niet alleen de positie van de bewegende grenslaag rigoureuzer worden vastgesteld, maar tevens kan het computergeheugen efficiënter worden benut.

Tot slot worden verscheidene resultaten gepresenteerd voor simulaties van het beschrijven van DVD en Blu-ray schijfjes. In het bijzonder is het interessant om na te gaan wat de effecten zijn van de polarisatie van het invallende licht, en de samenstelling van de gelaagde structuur van een schijfje, op de vorm en omvang van het gebied dat smelt ten gevolge van de laserpuls. Bovendien onderzoeken we onder welke omstandigheden latente warmte van belang is voor de modellering van het schrijfproces.

CONTENTS

CHAPTER 1

Introduction

The application of optical rewritable recording dates back to the year 1997, when the compact disc rewritable (CD-RW) was introduced to the consumer market. As opposed to the compact disc recordable (CD-R), which allowed for data to be written only once, the rewritable disc made it possible to write and erase data up to a thousand times. Because of the enormous success of the compact disc as a data storage medium and the growing demand for larger storage capacity, several successors of the CD have been developed in later years. These disc formats, which include the digital versatile disc (DVD) and the Blu-ray disc, all extend on the optical recording concept as developed for the CD.

A prerecorded optical disc is pressed and contains pits that are positioned along an outwards spiraling track. When scanned by a laser beam, these pits give cause to modulations in the reflected light as the beam travels from a pit to a non-pit, or vice versa. The observed modulations are translated into a sequence of ones and zeros, which forms a binary representation of the original data. A recordable disc contains a layer consisting of an organic dye material. This dye can be locally decomposed by means of high power pulses with a laser beam, resulting in a pattern of pits and non-pits, similar to that of a prerecorded disc. This process is irreversible.

The recording stack of a rewritable medium consists of various layers. The actual recording of data, stored as an array of amorphous regions in a crystalline background, takes place in a specific layer of the recording stack. This layer consists of a so-called phase-change material. The amorphous regions, called marks, are created as a result of very short high intensity pulses of a laser beam that is focused on this active layer. The absorbed light intensity is partially transformed into heat, which locally causes the phase-change material to melt. As soon as the laser is switched off, the

1

molten material solidifies. At the same time, recrystallization occurs in those regions where the temperature is below the melting temperature, but still above the recrystallization temperature. Since the cooling down is very rapid (quenching), almost no recrystallization occurs within the molten region, and thus a solid amorphous area is formed. The same laser beam, but at a lower power level, is used to fully recrystallize the amorphous regions. The recorded data is then erased.

Although much is understood about the concept of optical rewritable recording, many open questions remain. In order to gain better insight in for instance the influence of polarization and wavelength of the incident light or the geometry and composition of the stack on the shape and position of a mark, robust (numerical) modeling is essential. As a result, the occurrence of undesirable effects, such as the (partial) erasure of marks in adjacent data tracks (so-called cross-track cross-erasure), can be minimized and an increase in data density can be obtained via optimization.

The final shape and size of a mark are determined by the region that melts due the laser light, solidification and the effects of (re)crystallization. In this thesis, a model is presented for the melting component of the mark formation process. The presented model is part of a general model for phase-change recording, consisting of an optical part, which involves the computation of the electromagnetic field inside the disc, a thermodynamic part, for the computation of the temperature distribution in the disc, and several aspects from materials science, such as the effects of crystallization.

In the proposed model, latent heat, which is the amount of energy that is consumed during a phase transition, is taken into account. To be able to run simulations for industrial applications, such as optical rewritable recording, an adaptive local mesh refinement has been developed. Although our melting model is presented for phase-change materials that melt at a melting point, the model can easily be extended to account for materials that melt along a melting trajectory. We expect that the developed method is a solid basis for the incorporation of, for instance, recrystallization effects.

1.1   Outline of the thesis

In this thesis we investigate efficient numerical methods for the simulation of moving boundary problems due to a phase change, inside complex composite domains. We apply the developed methods to model the melting component of the mark formation process in optical rewritable recording.

The outline of this dissertation is as follows.

- In Chapter 2, the basic aspects of optical rewritable recording are discussed in detail. Besides the principle of phase-change recording, these aspects include the optical system, the structure of a rewritable disc and recording strategies.

- A mathematical model for the melting component of the mark formation process is proposed in Chapter 3. The melting is described by a two-phase Stefan problem. The model is presented as part of a more general model for rewritable recording. The governing equations and interface conditions are discussed, and modeling assumptions are introduced, and motivated.

- In Chapter 4, the optical model is discussed. This model is of great importance, since it provides the input for the melting model. It is demonstrated how the optical model can be combined with a thermal threshold value model, to obtain a preliminary estimate of the size and shape of mark. The combined model is applied to a DVD and a Blu-ray recording stack.

- In Chapter 5, a review of numerical methods for solving two-phase Stefan problems that are available from literature, is presented. The main goal of this study is to evaluate which methods are applicable to moving boundary problems inside complex three-dimensional composite domains. The methods that are considered are based on either an enthalpy formulation, a temperature approach or a level set technique. It is concluded that the level set approach is the least favorable method to solve our Stefan problem.

- In Chapter 6, two enthalpy based methods are evaluated, namely a nonlinear successive overrelaxation approach, and a pseudo-Newton method in which a relaxed linearization of the enthalpy is employed.

- In Chapter 7, a temperature based method is evaluated. A key feature of the discussed method is the use of a so-called discontinuous integration technique.

- Chapter 8 is devoted to the adaptive local space-time mesh refinement procedure, which is an essential feature of our 3D melting model. The refinement algorithm and its implementation are explained in detail.

- In Chapter 9, a variety of numerical results is presented. The performance of the enthalpy and temperature based methods is qualitatively compared, and it is shown that the temperature approach is best suited for our application. The local mesh refinement code is evaluated. Results for DVD and Blu-ray recording simulations are presented.

- Chapter 10 contains several concluding remarks and recommendations for future research.

CHAPTER 2

Phase-change recording

Since the introduction of the audio compact disc (CD), in Japan at the end of 1982 and in other markets at the beginning of the following year, optical storage media have become a major competitor on the portable data storage market. In this chapter, the recordable version of the CD and its successors, in particular rewritable discs, are considered. The main advantage of rewritable discs is that data can be written and erased many times. This is achieved by means of a local, solid-to-solid phase transformation inside the recording layer, induced by a short high power light pulse obtained by focusing a laser beam. We will consider the various aspects of the phase-change recording process in more detail in Sections 2.2-2.6. In the concluding section, future developments within the framework of optical rewritable recording are addressed.

2.1   A brief history of optical recording

After the enormous success of the CD and the CD read only memory (CD-ROM), a growing consumer demand for recordable optical storage media was eventually answered in 1990 with the introduction of the CD recordable (CD-R). With its storage capacity of 650 megabytes, equal to that of the CD/CD-ROM, it enabled people to make backup copies or to create their own data.

In 1997 the limitation of recording only once was overcome by the introduction of the CD rewritable (CD-RW), which allowed rewriting up to a thousand times. In the same year, a race between manufactures, which focused on larger data capacity and higher transfer rates, led to the introduction of the digital versatile disc (DVD). The need for a new storage medium had grown due to the forthcoming of high quality MPEG-2 encoded video material, and the increased data traffic over the Internet. With a storage ca-

5
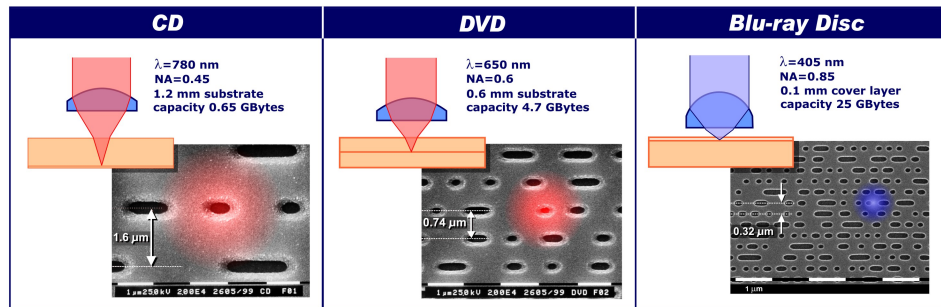
Figure 2.1: *Differences between selected pressed optical discs [32].*

pacity of 4.7 gigabytes, and even 8.5 gigabytes for the dual layered version, in combination with a maximum data transfer rate of around 11 megabits per second, the DVD easily fulfilled the newly imposed demands. Moreover, the possibility to play CDs with the DVD players (backward compatibility) and the rapidly growing amount of film titles that became available, made that the growth in popularity of the DVD even surpassed that of the CD.

Besides the read-only version of the DVD, also several single time recording (DVD+R) and multiple time recording (DVD+RW and DVD random access memory (DVD-RAM)) versions were introduced to the general public.

Currently, the Blu-ray disc[1] (BD), developed by Philips, Sony, and other companies, and the high definition versatile disc (HD DVD), developed by Toshiba and various other companies, are battling to become the new standard in optical storage.

Since the specifications and means of data storage of these so-called next-generation DVDs are very different, the success of either recording medium will depend heavily on the support by major companies, that use these types of storage media for their products, world wide. This applies in particular to the movie, games and game consoles industry. For details concerning the two formats, and the consortia supporting them, we refer to the web sites of the Blu-ray disc association [27] and HD DVD promotion group [30].

2.2 The principle of phase-change recording

Before any type of information, e.g., a movie, music or computer software, can be stored on an optical disc, the data representing this information is first transformed into a binary sequence of 'zeros' and 'ones'. The way in which this binary data is stored on an optical disc, greatly depends on the

---

[1]The former digital video recording disc (DVR) standard, developed within the framework of high-definition television (HDTV) by Philips and Sony around 1999
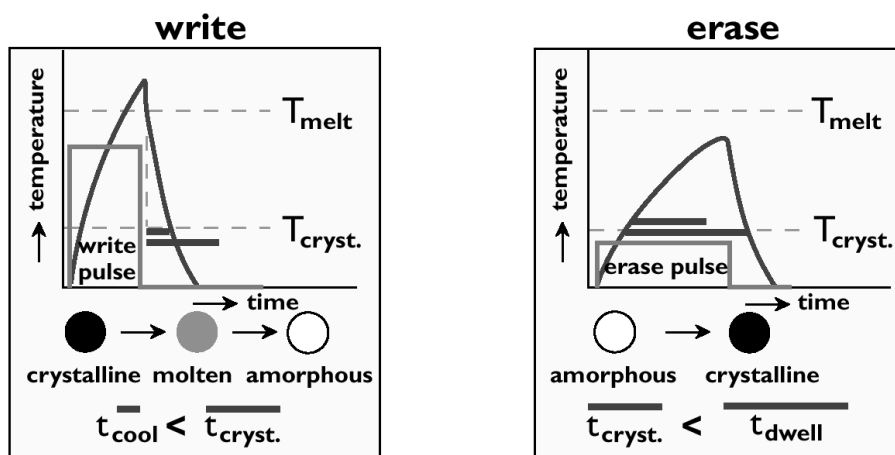
Figure 2.2: *The write and erase process illustrated [32].*

type of medium. Read-only discs, such as the audio DVD and BD-ROM, are pressed, leaving a concentric spiraling pattern of pits (and non-pits) of various sizes along the surface of the disc; see Figure 2.1. During readout, modulations in the reflected light, induced by the pits and non-pits can be detected, and can be interpreted as a binary representation of the recorded data. Write once media contain a layer that consists of an organic dye material. Locally, the dye is irreversibly decomposed by means of high energy laser pulses. The differences between decomposed and intact dye affect the readout laser signal in a similar fashion as for the prerecorded discs.

In systems for rewritable discs, the active layer of the optical disc is subject to crystallographic changes upon heating by laser radiation [22]. Application of short high power laser pulses, such that the temperature exceeds the melting temperature T_{melt}, leads to the melting of the (initially) crystalline phase-change material. As a result of rapidly cooling down (quenching), to temperatures below the crystallization temperature T_{cryst}, amorphous regions are created. See Figure 2.2 for an illustration. These amorphous regions are called marks. The quenching procedure prevents the nucleation and growth of the crystalline phase during the cooling down, i.e., the recrystallization of the mark.

Marks are erased by heating the amorphous material to a temperature between its melting temperature T_{melt} and its crystallization temperature T_{cryst}. If we define the crystallization time t_{cryst} to be the time required for an amorphous region to fully regain the crystalline state, then a mark is erased by leaving the spot dwell over the amorphous region for a period longer than the crystallization time of the phase-change material ($t_{\mathrm{dwell}} > t_{\mathrm{cryst}}$). The speed at which data can be erased is therefore dependent on the type of material used in the active layer.

Two kinds of phase-change materials exist, namely nucleation dominated and growth dominated. In the former, small crystalline nuclei inside the amorphous mark start to grow until they impinge upon each other. In the latter, the probability of the occurrence of crystal nuclei is low, but crystal growth is very fast. The crystallization of the amorphous mark is then largely due to the inward growth of the boundary between the mark and the crystalline surrounding.

The most commonly used phase-change materials are stoichiometric[2] SbTe alloys, in particular Ge-Sb-Te [70] and Ag-In-Sb-Te [35]. Due to relatively high crystallization times (t_{cryst} = 100–250 ns), Ag-In-Sb-Te alloys are mainly used in low speed applications such as CD-RW. The various compositions of this alloy allow rewriting between a thousand and ten thousand times. For applications in high-speed recording, such as DVD+RW, Ge-Sb-Te alloys are used (t_{cryst} < 50 ns). The rewritability of these types of compositions ranges between 10^5 and 10^6 times. For the Blu-ray system, doped eutectic[3] SbTe alloys have also been studied [6], and issues like their stability and cyclability have been addressed [7].

2.3   The structure of a rewritable disc

Optical rewritable discs are composed of various layers. At least one of these layers consists of a phase-change material. In Figure 2.3 the recording stack for a typical Blu-ray disc is illustrated. Since this configuration contains only one recording stack, the disc is called a single-layered disc.

For rewritable discs, the surface of the substrate, and subsequently the layers of the recording stack on top of the substrate, contain a concentric, outwards spiraling groove. This groove is needed to guide the optical system during the writing process. In absence of the groove, the accurate positioning of the optical head would be impossible in regions where no data has been recorded, due to a lack of reference points. Because of this grooved configuration, in radial direction, the disc is said to have a (periodic) 'land and groove' structure.

The stack configuration shown in Figure 2.3 is called an IPIM stack [22]. The various layers of the IPIM stack are sputtered on the pre-grooved substrate. On top of the substrate, made of polycarbonate or glass, is a metallic **Mirror** layer. On top of this metallic layer, there are subsequently a dielectric **Interference** layer, the **Phase-change** layer, and another dielectric **Interference** layer.

---

[2]describes a quantitative relationship, usually expressed as the ratio between two or more chemical substances undergoing a physical or chemical change; the point at which the chemical reaction ends or stabilizes [28]

[3]alloy or solution with components distributed in the proportions necessary to minimize the melting point [28]
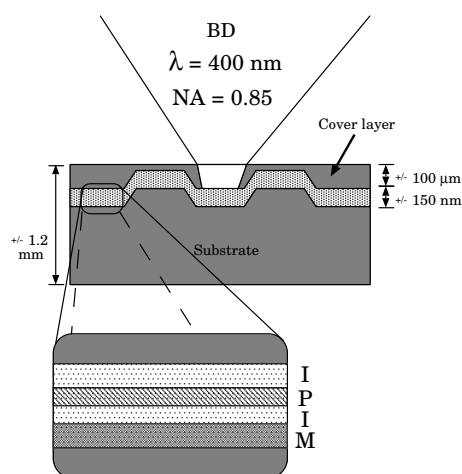
Figure 2.3: *An illustration of a typical cross section of a Blu-ray disc, showing the position of the IPIM recording stack. The recording stack is placed relatively close to the discs surface in order to preserve a small spot diameter. The thickness of the layers are not to scale.*

The dielectric layers, often a mixture of ZnS and SiO_2, and the metallic layer, for instance consisting of aluminum or silver, protect the phase-change layer from environmental influences. Their thickness is chosen such that the optical contrast between the crystalline and amorphous state of the phase-change material is optimal. The dielectric layer between the phase-change layer and the cover is relatively thick. In this way, the cover is protected from thermal damage during writing. The dielectric layer between the phase-change layer and the metallic layer is relatively thin, so that sufficient heat can reach the metallic layer and quenching is made possible. Since the metallic layer acts as a heat sink during quenching, it must be sufficiently thick. The life time of a disc depends on the composition of the layers of the recording stack.

Besides the optical and thermal properties mentioned, the layers must consist of materials of mechanically good quality, to avoid or delay the appearance of defects, e.g., pinholes and micro-cracks. These defects are induced by material flow and thermal deformation during repeated heating and quenching.

Stacks used in dual-layer discs, which allow for an increase in data capacity, have been studied for DVDs, and for the Blu-ray system [68]. The two recording stacks are optically accessed from one side of the disc, see Figure 2.4. To ensure that a sufficient amount of light can reach the second recording stack, L1, there is a practical requirement of 50% transparency for the first recording stack, L0. A conventional non-transparent metal layer can thus not be used in L0. As a result of the omission of a metal layer in the first recording stack, a slow cooling behavior is observed in L0. Several improvements have been proposed to improve the thermal behavior

Figure 2.4: *Sketch of the dual-stack phase-change disc. For a DVD stack, L0 is the first recording stack, L1 is the deep recording stack. Both recording stacks are optically accessed from the top side. The thickness of the different layers are not to scale.*

of L0 stacks, such as additional transparent heat sinks [68], or thin semi-transparent metal layers, such as silver alloys [1]. A drawback of these solutions, is the decrease of sensitivity of the stack with respect to write power.

It is not surprising that in the stacks used in dual-layer discs, thermal interference between the recording stacks needs to be avoided. This is achieved by taking the so-called spacer layer, that separates both recording stacks, thick enough. The thermal behavior of the two stacks can then be studied independently.

2.4   The optical system

The various data storage discs mentioned in the previous sections all have in common that the reading, and if applicable, the writing, of data on the disc is done optically. For both reading and writing, the same optical system is used, but with different power levels of the laser beam.

In Figure 2.5, the setup of an optical head of an optical system is shown. The optical head contains a laser diode, a collimating lens, a polarizing beam splitter (PBS), a quarter wave plate, an objective lens and a detection system. The collimating lens is used to transform the diverging linearly polarized beam, emitted by the laser diode, into a parallel beam. After passing through the PBS and the quarter wave plate, the light is circularly polarized. Finally, the objective lens focuses the beam on the optical disc.

The light that is reflected by the metallic layer of the disc is collimated by the objective lens on its way back through the optical system. The quarter wave plate then converts the dominantly circularly polarized reflected light into a linear polarized beam such that the polarization is perpendicular to

Figure 2.5: *Setup for an optical system.*

that of the incident beam. The PBS finally redirects the reflected beam onto the detection system. During the read-out of data, the detection system can determine whether a 'zero' or a 'one' is read, based on a priori knowledge about the differences between the reflected intensities when the spot is focused on a pit or a non pit (for pre-recorded discs), on a decomposed or intact dye material (for write once media) or on the amorphous or crystalline state of phase-change material (for rewritable media) [12]. The read-out of a rewritable disc requires that the contrast between the reflectivity of the crystalline and the amorphous state is sufficiently high to overcome the noise caused by the different physical and electronic components.

For all optical storage discs it holds that the binary data is stored on a concentric, outwards spiraling track. To ensure a consistent read-out of the disc, the focused spot must be kept centered on this track. When the optical head moves away from the track's center, an asymmetry in the reflected field is induced. Whenever such an asymmetry is detected, the optical head is guided such that the beam is again focused on the center of the track. This procedure is called tracking.

Due to diffraction by the finite aperture of the lens, the diameter D (in air) of a focused spot is non-zero and given by [26]:

$$D \approx \frac{\lambda}{\text{NA}},\tag{2.1}$$

where λ is the wavelength of the incident light, and NA is the numerical aperture of the objective lens. The NA is the sine of the angle between the outer ray and the principle axis of the objective lens times the index of refraction n of the medium in-between the lens and the cover. In case of air, $n = 1$. The focal depth (or depth of focus) δ of a spot, can be defined as the range (in image space) over which the focused spot diameter remains below an arbitrary limit, see Figure 2.7. In an imaging system, the depth of focus would be the distance (in object space) over which the system delivers
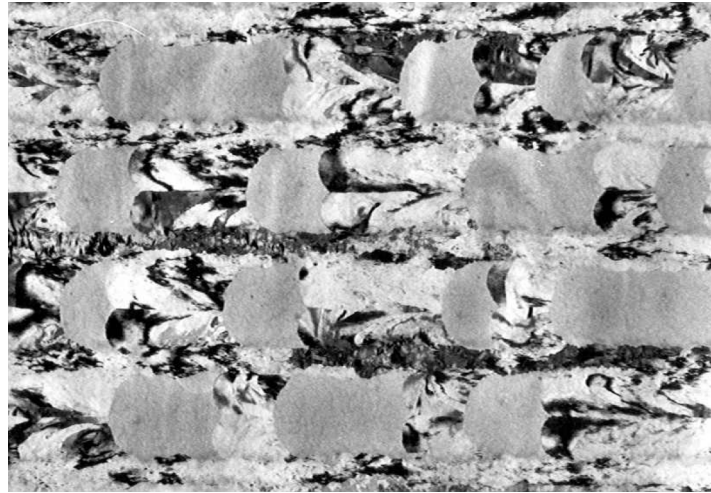
Figure 2.6: *Transmission electron microscopy image of recorded amorphous marks in a crystalline background [46].*
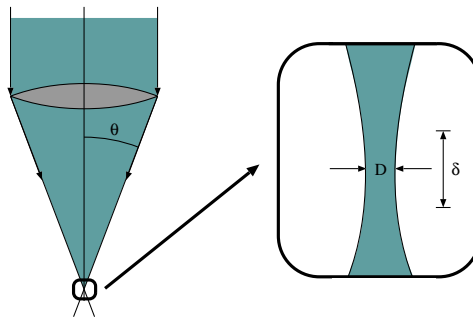
Figure 2.7: *The NA of a lens is given by $n \sin(\theta)$, where n is the index of refraction of the medium in-between the lens and the cover.*

a sharp image. The focal depth (in air) is given by:

$$\delta \approx \frac{\lambda}{\text{NA}^2}. \tag{2.2}$$

An overview of some specific values of optical and mechanical parameters mentioned in this section, for a selection of optical recording media, is listed in Table 2.1. Note that the diameter of the spot is always larger than the track pitch. Consequently, part of the incident light will inevitably fall onto adjacent tracks, so that (partial) cross-track erasure can become problematic.

The focal depth is especially of interest during the writing process, because it is important that the largest part of the energy of the incident light reaches the recording layer. But, due to internal reflections, it is very difficult to choose the proper focal plane. However, Table 2.1 suggests that the system is not sensitive to the precise position of the focal plane, because

the focal depth is at least a factor four larger than the thickness of the recording stack. It is therefore sufficient to ensure that the recording stack is positioned at a distance of approximately $\frac{\delta}{2}$ for a spot in air.

2.5 Recording strategies

Several methods have been proposed for writing data on rewritable discs (for instance, see Reference [66], Chapter 1.5). In the early nineties, recording strategies such as 'pulse position' recording and 'mark edge' recording have been studied. When pulse position recording is used, all amorphous marks have the same length and the information is stored in the lengths of the spaces between the written marks.

With mark edge (or 'pulse-width') recording, the written marks vary in length, which allows for information to be read from both the length of the amorphous marks, as well as the length of the crystalline spaces between the marks. During the writing of each mark, the power of the spot is kept at a constant high power level. Due to the accumulation of heat during melting, the recorded mark tends to have a teardrop shaped distortion.

With 'multi pulse' recording, each mark is formed by a sequence of successive short high power laser pulses, generating overlapping amorphous dots as shown in Figure 2.6. In between the pulses, the laser power is set to a low level, so that after each laser pulse the molten material is quenched and the accumulation of heat is avoided. When no marks are written the laser power is switched to an intensity level which is high enough to crystallize the material and erase possible earlier written marks. Since this method of multi-pulse recording enables the system to overwrite old marks directly, it is called a direct overwrite (DOW) method; see Figure 2.8.

The most commonly used schemes for writing the amorphous marks are groove recording, and land-groove recording. In case of groove recording, the marks are only written in the grooves of the disc. When the land-groove

Table 2.1: *An overview of several optical and mechanical properties of a selection of recordable and rewritable media. The values given for the track pitch (TP) and the thickness of the recording stack (Δ) are averaged values. The specified wavelengths are in air.*

	capacity [GB]	λ [nm]	NA [-]	D [nm]	TP [nm]	δ [nm]	Δ [nm]
CD(-R/-RW)	0.65	780	0.50	1560	1500	3120	≈ 250
DVD(-R/+RW)	4.7	650	0.65	1000	740	≈ 1540	≈ 250
BD	23.5/25	405	0.85	≈ 470	320	≈ 550	≈ 150
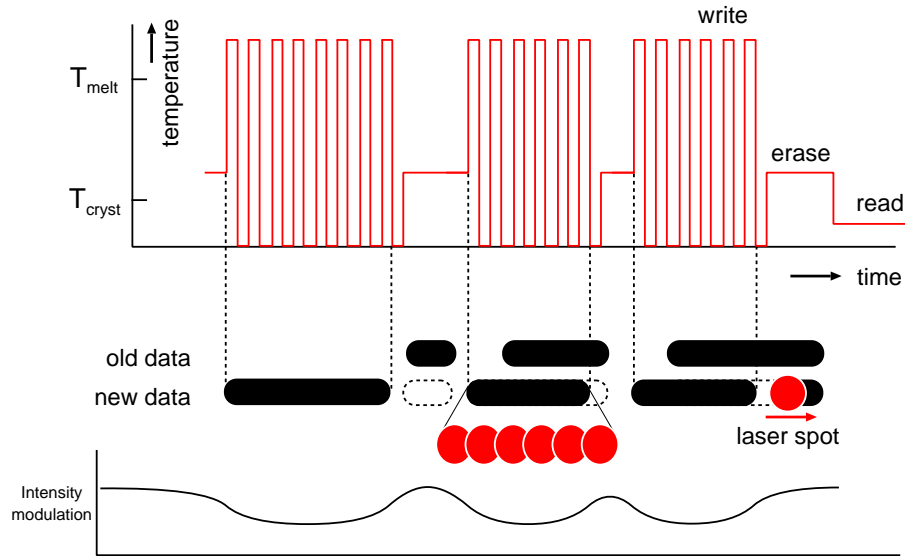
Figure 2.8: *The direct overwrite strategy. The intensity of the high power laser is set to such a level that during the recording of new data, existing old data is erased. During reading, modulations in the intensity of the reflected light are measured [32].*

scheme is used, the marks are also written on the lands. The distance between adjacent grooves is called the groove pitch, and the distance between adjacent tracks is called the track pitch. Thus, for groove recording, the track pitch and groove pitch are equal, whereas in case of land-groove recording, the groove pitch is twice the track pitch. We refer to Table 2.1 for the averaged values of the track pitch for a selection of disc types.

2.6 Some remarks on high density recording

As has been mentioned in Section 2.1, research and development in the field of recordable and rewritable discs focuses on both the increase of data storage capacity as well as data transfer rates. An increase of capacity (or bit density), can be realized by either reducing the track pitch, i.e., the radial density, or using smaller mark lengths (linear density). The average mark length depends on the wavelength λ of the laser light and the numerical aperture of the objective lens. By reducing the spot diameter D, as defined by (2.1), smaller marks can be written, and detected, thus increasing the linear density. A consequence of the reduced mark size, is that the track pitch can be scaled down as well.

To achieve a high radial density, a narrow track pitch is preferred. It is then very important to control thermal cross-track cross talk, but also optical cross talk. Optical cross talk occurs when during reading the laser light is also reflected on adjacent tracks, causing distortions in the detected

light intensity. It has been shown that by tuning the groove depth, optical cross talk can be reduced to an acceptable level [48].

The occurrence of thermal cross-track cross talk during writing is a serious problem, because thermal diffusion from the central track, and light absorption in adjacent tracks, can cause partial erasure of existing marks on the adjacent tracks. The temperature distribution has been shown to be dependent not only on the geometry of the grooved structure and the configuration of the recording stack, but also on the wavelength and polarization of the light. Furthermore, differences have been observed between land and groove recordings [53].

The choice of the recording scheme is another way of influencing a disc's radial density. When land-groove recording is used, the radial density can be increased, but controlling the above mentioned cross talk phenomena then becomes much more problematic.

Recording speed is limited by the (re)crystallization time of the active material. During writing, pulse duration and intensity are to be taken such that the crystalline material melts within a period of time shorter than the crystallization time to prevent (complete) recrystallization. In addition, the individual amorphous dots should be sufficiently close together to form a mark. During erasure, the spot should remain sufficiently long above an amorphous region to keep it at a temperature above the crystallization temperature for at least the crystallization time. An increase of transfer rate can thus be realized by optimization of the composition of the active material. The reduction of the bit length, by decrease of the spot size, also enables faster recording speeds since smaller marks imply shorter (re)crystallization times.

2.7 The future of optical storage

The quest for faster recording speeds and larger storage capacities does not end with the Blu-ray disc and the HD DVD. Potential successors of these recording media are intensively being researched. A so-called fourth generation optical rewritable recording system, that builds on the concept of data storage in one or more recording stacks, is called near field recording. This new type of optical recording allows for the evanescent waves in the air gap between the lens and the surface of the disc, that decay within a fraction of the wavelength of the blue laser light, to contribute to the total intensity of the spot. This feat is achieved by use of a so-called solid immersion lens which is kept at close distance ($\leq$ 20 nm) from the surface of the disc by an actuator. The effective NA that can be achieved in this way is 1.9. In addition, the recording layer is positioned at about 60 nm from the disc's surface. The target storage capacity, for a CD sized near field recording disc, is approximately 300 gigabytes [72].

(a)   (b)
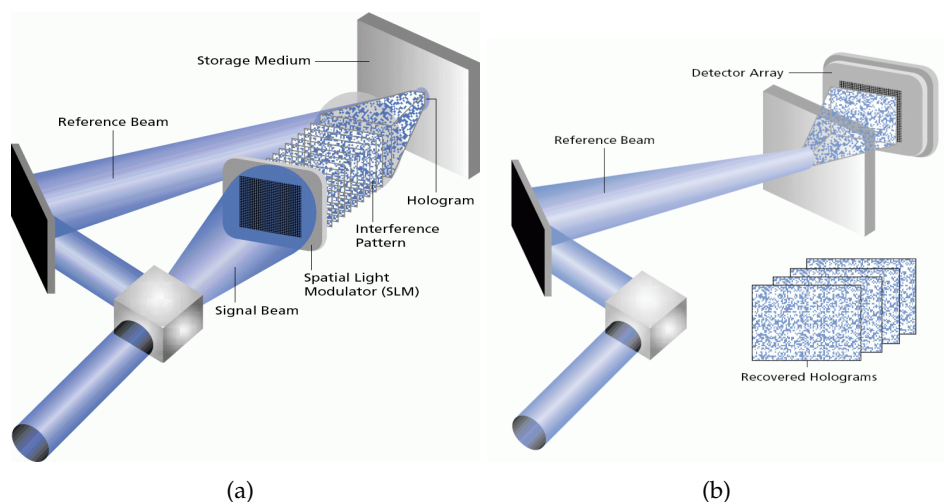
Figure 2.9: *Overview of the HVD optical system. (a) Write, (b) read [31].*

A novel optical recording method is based on holographic storage, for instance see Reference [31]. To record data, first a single laser beam is split into two beams. One beam carries the data, the other beam is a reference beam. The hologram is formed at the location inside the recording medium, where the two beams interfere. The binary data is translated into a grid of pixels of a device called a spatial light modulator (SLM), that either block or transmit light. When the light of the signal beam traverses through the SLM, it is thus encoded with the 'checkerboard' pattern of the pixel grid; see Figure 2.9. Because the SLM can consist of millions of pixels, the number of bits that can be recorded simultaneously, can be accordingly large. Moreover, many different holograms can be written in the same volume of material, by varying the reference beam angle, wavelength or the position of the recording medium.

The deflections of the reference beam off the recorded hologram are projected onto a detector. The projected data is then used to reconstruct the stored information. Because the data stored in the hologram is read out in parallel, fast data transfer rates of 10's to 100's megabytes per second, can be obtained. Moreover, this technology does not require very fast rotation of the medium, to get very high transfer rates, and the shape of the media is not limited to that of a disc. Altogether, this makes that the Holographic Versatile Disc (HVD) can become a serious competitor in the future optical recording market.

CHAPTER 3

Mathematical model for phase-change recording

In the previous chapter we touched upon the general basic concepts of phase-change recording. In this chapter, a mathematical model for rewritable recording is discussed. Of particular interest is the modeling of the melting component of the mark formation process, for which a moving boundary formulation is presented in Section 3.4. Model assumptions are addressed in Section 3.2.

3.1   Review of the optical recording principle

Before discussing the modeling aspects of recording of data for rewritable optical discs, let us briefly recall how this process works. In optical rewritable recording, binary data is written by applying short high power pulses with a laser beam that is focused on the phase-change-layer of the disc. As a consequence of the heating, the phase-change-material melts and the crystalline structure of the material is broken down. After the laser is switched off, the temperature rapidly drops from above the melting temperature to below the crystallization temperature (quenching). Because the stack design and material properties are taken such that the duration of the cooling down is shorter than the crystallization time of the phase-change material, recrystallization is limited, and an amorphous solid region remains. A sequence of amorphous dots, written shortly one after another, forms a mark.

3.2 Model assumptions

Obviously, the recording of data for rewritable optical discs is a complicated interaction of various physical processes. In the modeling of the phase-change recording process, three different parts can be distinguished, namely, an optical part, related to the computation of the light distribution inside the disc; a thermodynamics part, related to the distribution of heat in the recording stack; and the modeling of the melting and (re)crystallization, for which knowledge of materials science is important.

From a modeling point of view, the complexity of the process of recording presents several challenges that need to be addressed. Although the recording process is complex in itself, the major challenge lies in the mutual dependence of the various physical parameters, associated with these processes. For example, the focused laser beam (locally) causes a rise of temperature in the disc. As a result, the characteristics of the materials in the stack change. Not only the thermal properties, such as the thermal conductivity, are modified, but also the optical characteristics, such as the index of refraction and the absorption coefficient, are affected.

Another difficulty is that the recording process takes place on a submicrometer scale, which means that many phenomena should be taken into account. Consequently, sophisticated, and often complicated, models are required. For instance, the polarization of the incident laser light can be expected to play a significant role in optical recording, and therefore a rigorous vector diffraction model based on Maxwell's equations is required in the calculation of the light intensity in the stack.

To obtain a feasible global model for the process of data recording, a selection of sensible simplifications are to be introduced. The first assumption that is made, is that the optical parameters of the materials inside the disc, are temperature independent. The major benefit of this decoupling, is of course that the optical and the thermal model can be evaluated separately (black box principle). It also implies that, even though the thermal model is time dependent owing to the rotation of the disc, and the application of multiple laser pulses, the optical problem can be approximated by a time-independent formulation. The practical advantage is that the optical problem needs to be evaluated only once for each simulation. However, as a consequence, we do not discriminate between the amorphous and crystalline state in the optical model.

The actual process of the writing of an amorphous mark consists of a complicated mixture of melting, solidification and (re)crystallization (cf. Figure 2.2). We restrict ourselves to the accurate modeling of the melting component of the mark formation process, even though we are aware that, besides the melting, (re)crystallization plays a major role with respect to the final shape and size of the mark (see for instance Meinders et al. [45]). The key motivation for this choice is, that the proper modeling of the melting

stage of the mark formation process is already challenging in itself. Besides, the melting model is also applicable to many other melting and solidification processes in industry, such as for instance food processing or the steel industry. However, a preliminary study regarding crystallization kinetics has been performed, of which the results can be found in Appendix A. For a detailed study on the determination of the crystallization kinetics in fast-growth phase-change materials, we refer to Meinders and Lankhorst [43].

To obtain the light distribution inside the disc, the diffraction model by Brok and Urbach [8] for a 3D spot, incident on a 2D periodic multi-layered recording stack, is used. In Brusche [9], this model has been successfully extended to a 3D region of interest within the framework of optical rewritable recording. Similar to the model by Yeh et al. [71], the model by Brok and Urbach is based on a plane wave expansion of the spot. But the sampling of the spot is such, that the plane waves can be divided into sets that, for the given period of the grooved structure (grating), consist of waves that are orders of each other. This reduces the number of scattering problems that have to be solved considerably. The superposition of the plane waves in each set yields a quasi-periodic incident field, whose interaction with the periodic grating can be computed by solving a single boundary value problem. This boundary value problem is derived on a 2D computational box that is one period wide. Instead of approximative absorbing boundary conditions, exact radiation conditions for the scattered near field are used. The total electromagnetic field is obtained by coherently adding all scattered fields relating to all quasi-periodic incident fields.

When the light distribution in the recording stack is determined, the amount of energy that is absorbed in the absorbing layers of the stack, can be computed from the electromagnetic field. It is in general assumed that all of the absorbed light is converted into heat. That is, the absorbed energy is considered to be the single driving force for the temperature model. For more details on the optical model that is used in our phase-change recording model, we refer to Chapter 4.

Table 3.1: *Numerical values for the specific heat c and thermal conductivity κ.*

	c [J/cm^3/K]	κ [W/cm/K]
substrate	1.7	0.0022
phase-change (amorphous)	1.285	0.0017
phase-change (crystalline)	1.285	0.005
phase-change (liquid)	1.285	0.005
dielectric	2.005	0.006
metallic mirror	2.45	0.25
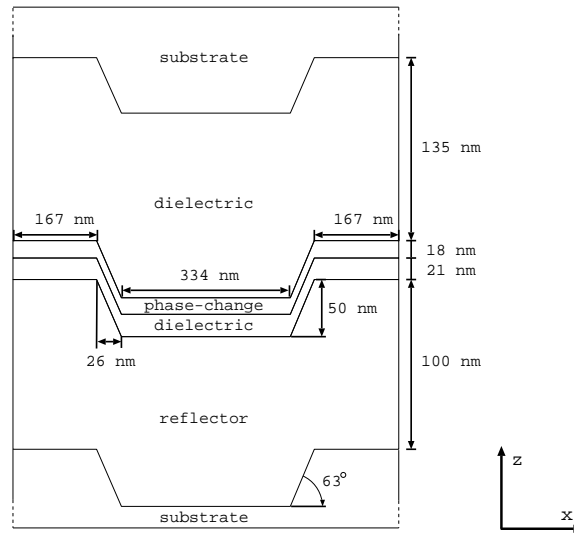
Figure 3.1: *The geometry of a grooved DVD stack. The groove depth and inclination angle have been exaggerated.*
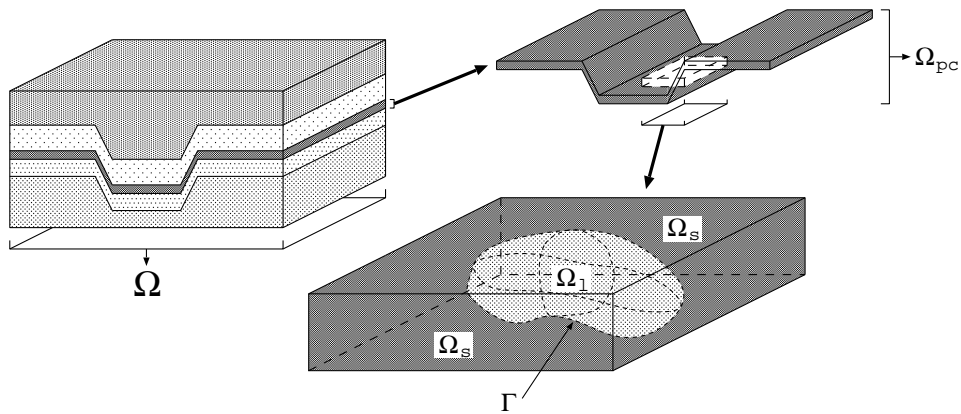
Figure 3.2: *The computational domain.*

3.3   The melting model

The most basic model that can be used to obtain a preliminary estimate of the regions that melt due to the absorption of the laser light is a *temperature threshold value model*. That is, we solve the heat diffusion equation for the temperature rise above ambient, using the absorbed energy distribution obtained from the optical model as source term, and check in which regions of the domain the temperature has become higher than the melting temperature of the recording material.

   In practice, the phase transition from solid to liquid is not instantaneous, and a certain amount of energy is needed to complete the transformation.
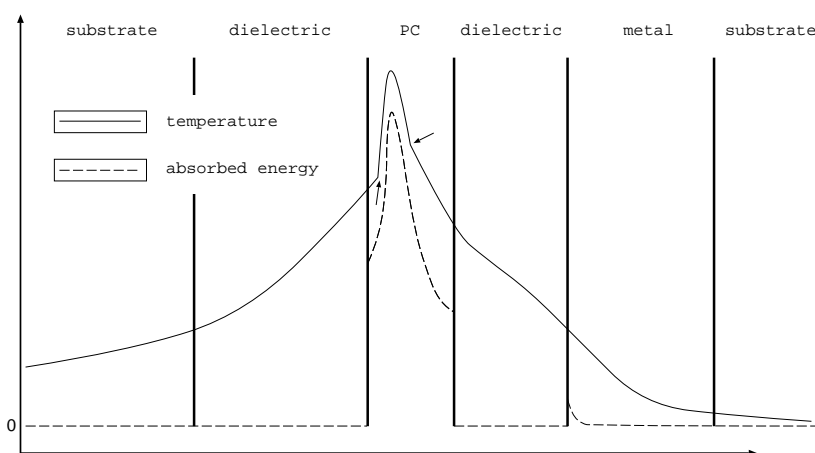
Figure 3.3: *Sketch of the absorbed energy and temperature profile across the interfaces of a Blu-ray disc. The arrows indicate jumps in the gradient of the temperature at the interface between the solid and liquid state.*

The amount of Joule needed for a volume of 1 cm^3 of solid material to become fully liquid, is expressed by a quantity called the latent heat. The inclusion of the latent heat, in an isolated environment, is expected to be important, as the following example illustrates. Consider the values of the specific heat of the phase-change material, as listed in Table 3.1, and the latent heat of the solid-to-liquid transition $L = 418.9$ J/cm^3, as given in Reference [52]. Then, based solely on the specific heat $C \approx 1$ J/cm^3/K, an upper bound can be given for the effect of latent heat on the rise in temperature above ambient: the melting of 1 cm^3 is approximately equal to heating up that same volume by about 400 K, which is 40% of the maximum temperature of 1000 K as reported in Reference [52]. To obtain a more accurate estimate, more information is needed about, for instance, the intensity and distribution of the heat source, and consequently, the final volume of the molten region. For a specific recording stack, it appears that the effect of latent heat can be as little as approximately 1% [42].

3.4 A moving boundary problem formulation

The melting of a phase-change material can be described as a moving boundary problem. Depending on the composition of the phase-change material, the melting occurs either at a melting *point T_m*, or along a melting *trajectory*. The interface between the solid and the liquid phase is 'sharp', in case of a melting point. These so-called isothermal problems can be described as a two-phase Stefan problem. For a non-isothermal problem, a region in which the material is neither solid nor liquid separates the solid and liquid state. This region is called the mushy region, and the material

contained in this region is referred to as the mushy phase. Mushy problems can be modeled as a multi-phase Stefan problem (the mushy phase is sometimes further subdivided). In this thesis, it is assumed that the phase-change materials that are considered, are all of the isothermal type. However, the presented model can be extended to mushy region problems without much difficulty.

Let Ω be a prescribed subdomain of $\mathbb{R}^n$ with fixed outer boundary $\delta\Omega$, see Figure 3.2. The domain Ω consists of one or more disjunct, possibly composite, subdomains, each containing a different material. At least one of these subdomains, Ω_{pc}, contains a phase-change material. It is assumed that the density ρ, latent heat L, heat capacity c, and thermal conductivity κ are constant for each material. To distinguish between the various values of the physical parameters for the different materials, we introduce a subscript p for each parameter ξ, such that:

$$\xi_p = \begin{cases} \xi_s, & T \leq T_m, \text{inside } \Omega_{pc}, \\ \xi_l, & T > T_m, \text{inside } \Omega_{pc}, \\ \xi_{material}, & \text{elsewhere.} \end{cases} \qquad (3.1)$$

For most applications it is assumed that initially, i.e., at $t = t_0$, the whole domain Ω is solid and that Ω_{pc} is fully crystalline. From a certain time t_m, $t_0 \leq t_m \leq t_e$, Ω_{pc} is composed of two disjunct, possibly composite, subdomains $\Omega_s(t)$ and $\Omega_l(t)$, occupied by the solid and liquid phases of the phase-change material, respectively. These subdomains are separated by an unknown surface $\Gamma(t)$, to be determined.

The two-phase Stefan problem for the melting process inside a recording stack is given by:

$$\rho_p c_p \frac{\partial T(\boldsymbol{x}, t)}{\partial t} = \kappa_p \Delta T(\boldsymbol{x}, t) + q(\boldsymbol{x}, t), \qquad \forall \boldsymbol{x} \in \Omega \setminus \Gamma(t), t \geq t_0 \qquad (3.2a)$$

$$\rho_p L v_n = \left[\kappa_p \frac{\partial T(\boldsymbol{x}, t)}{\partial \boldsymbol{n}} \right], \quad T(\boldsymbol{x}, t) = T_m, \qquad \text{for } \boldsymbol{x} = \Gamma(t), t \geq t_m \qquad (3.2b)$$

$$T(\boldsymbol{x}, t_0) = \bar{T}_1(\boldsymbol{x}), \qquad \forall \boldsymbol{x} \in \Omega \qquad (3.2c)$$

where $\boldsymbol{n}$ denotes the unit normal vector on the moving interface pointing from the solid domain into the liquid domain, and v_n is the velocity of the moving interface. By $[\varphi]$ we denote the jump in φ defined as:

$$[\varphi] = \lim_{\substack{\boldsymbol{x} \longrightarrow \Gamma(t) \\ \boldsymbol{x} \in \Omega_s(t)}} \varphi(\boldsymbol{x}, t) - \lim_{\substack{\boldsymbol{x} \longrightarrow \Gamma(t) \\ \boldsymbol{x} \in \Omega_l(t)}} \varphi(\boldsymbol{x}, t). \qquad (3.3)$$

On the complementary parts $\delta\Omega_i, i = 1, 2, 3$ of the fixed outer boundary $\delta\Omega = \bigcup_{i=1}^3 \delta\Omega_i$, one or more of the following boundary conditions are imposed:

1. A Dirichlet condition on $\delta\Omega_1$:

$$T = \bar{T}_2(x). \tag{3.4}$$

2. A Neumann condition on $\delta\Omega_2$:

$$\kappa_p \frac{\partial T}{\partial n}(x) = \bar{q}(x), \tag{3.5}$$

   where $\bar{q}(x)$ is a given normal heat flux.

3. A radiation-type boundary condition on $\delta\Omega_3$:

$$\kappa_p \frac{\partial T}{\partial n}(x) = \bar{\alpha}(T), \tag{3.6}$$

   where $\bar{\alpha}(T)$ is a function of temperature.

Figure 3.3 shows a sketch of a typical absorbed energy and temperature profile across the interfaces of a Blu-ray stack. Note that the absorbed energy is discontinuous across the interfaces between different materials. Furthermore, in general almost all of the light energy is absorbed in the phase-change layer and the maximum amount of energy is absorbed near the interface between the phase-change layer and the first (and thickest) dielectric layer. In contrary to the absorbed energy, the temperature is continuous across all interfaces. A peak in the temperature is observed where the absorbed energy reaches its maximum value. Furthermore, the gradient of the temperature is discontinuous at the phase boundary, due to the latent heat used for the phase transition (as described by the Stefan condition (3.2b)). This two-phase Stefan problem is therefore a (highly) nonlinear problem.

3.5 Conclusions

Rewritable recording can be described as a complex interaction of phenomena studied in optics, thermodynamics and materials science. By assuming that these phenomena can be decoupled in the sense described in this chapter, optical and thermodynamical models can be studied more or less independently.

The optical model consists of finding the light distribution inside the disc. For this, a modified version of the diffraction model by Brok and Urbach [8] for a 3D spot, incident on a 2D periodic multi-layered recording stack, is used. In Chapter 4, the adopted optical model is discussed in detail, where it is applied in combination with a temperature threshold value model for the melting component of the formation of a mark.

Although a temperature threshold value model can provide a good 'upper bound' of the size and shape of a mark to be formed, it is expected that the inclusion of latent heat results in more accurate predictions. We therefore propose a two-phase Stefan formulation for the melting of the phase-change material. We believe that the presented model is a solid basis for the incorporation of for instance (re)crystallization effects.

CHAPTER 4

The optical model and temperature threshold value model

One of the main modeling assumptions that was introduced in the previous chapter considered the decoupling of the optical and thermal components of the phase-change recording process. Furthermore, in Section 3.3 it was indicated that preliminary information about a mark, such as estimates of the size and shape, can be obtained using a relatively inexpensive temperature threshold value model. Moreover, it was mentioned that an adapted version of the diffraction model by Brok and Urbach [8] can be applied to obtain the electromagnetic field distribution in a recording stack.

This chapter consists of a reprint of an article published in the Journal of the Optical Society of America, part A [10], in which the adapted diffraction model is combined with a temperature threshold value model. The combined model is applied to a selection of 3D land and groove configurations, for the DVD and Blu-ray recording format.

However, a critical note must be made with respect to the results presented in the article. At the time of the publication, it was acknowledged that the temperature values that had been found were rather high. But because the shape of the temperature profiles for the DVD test cases were almost identical to those in Reference [53], it was assumed that these differences could be explained by the fact that no latent heat was taken into account. Recently, it became apparent that the deviation was for the largest part due to an incorrect scaling of the relative permittivity in the computation of the absorbed energy. Therefore, the correct numerical results are presented here. Consequently, parts of the text have been revised accordingly.

In Chapter 9 the results of the temperature threshold model will be compared with those obtained using the melting model proposed in Chapter 3.

4.1   Introduction

For rewritable optical storage media such as the rewritable compact disc, the rewritable digital versatile disc, and the Blu-ray Disc, data storage is based on two distinct states of a phase-change (PC) material. By application of short high power pulses with a laser beam that is focused on the storage layer, submicrometer-sized amorphous marks are formed in a crystalline background. After the marks have been written, they can be detected by monitoring intensity variations in the reflected light of the same focused laser beam at a much lower power level.

To increase the storage capacity and the data transfer rates of PC optical discs, modeling of the recording process is important. By use of numerical simulations, insight can be gained into the effects of the polarization of the laser spot, the effects of the spot size and the spot shape on the mark formation, and the differences between land recording and groove recording. Furthermore, the groove geometry and the stack can be optimized. Other phenomena that can be studied by modeling are the occurrence of optical and thermal cross-track cross-talk.

The model of the recording process for PC optical discs can be divided into three parts. In the first part the electromagnetic (EM) field distribution is calculated within the disc. From this field the light absorption in the medium can be derived. It is in general assumed that all of the absorbed light is converted into heat. Then, in the second part, the temperature distribution in the medium is computed by solving the heat equation. The third part is the modeling of temperature induced mark formation or erasure in the PC layer. In this paper only the first two parts of the model will be considered.

Because the feature sizes of the grooved structure of the medium are of the order of the wavelength of the laser spot, the polarization of the incident light cannot be neglected. A rigorous vector diffraction model based on Maxwell's equations is thus required in the calculation of the light intensity in the stack.

Many vector diffraction models have been considered by other authors to derive the EM field distribution in grooved multilayered stacks. These methods have been developed in the context of the optical readout of prerecorded digital versatile discs. Judkins and Ziolkowski [37] used the finite-difference time-domain method with absorbing boundary conditions and with a Lorentz dispersion model to incorporate conducting metals of which the real part of the electric permittivity is negative. Liu and Kowarz [38] applied the finite-difference frequency-domain method by using Higdon's absorbing boundary conditions and a preconditioned conjugate gradient method to solve the discretized system of equations. Marx and Psaltis [41] used a Lippmann-Schwinger type of integral equation to solve the diffraction problem for a two-dimensional (2D) incident beam.

In the above-mentioned papers the authors considered the interaction of
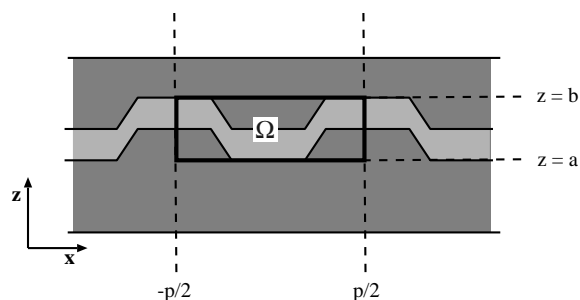
Figure 4.1: *Schematic visualization of the unit cell* Ω *in a cross section of an optical disc.*

a 2D incident beam with 2D grooved geometries. Yeh et al. [71] studied the more general problem of a three-dimensional (3D) spot that is incident on a 2D periodically grooved structure. We will call this type of model a two-and-a-half dimensional ($2\frac{1}{2}$D) model. The incident spot is expanded into plane waves, and a scattering problem is solved for every incident plane wave by use of a coordinate transformation to transfer the diffraction problem on the grooved structure to a configuration consisting of flat interfaces but with inhomogeneous materials (Chandezon's method).

Recently some authors published models that combine the calculation of the 3D EM field distribution, due to a 3D incident spot, with the computation of the 3D temperature distribution. Peng and Mansuripur [53] used a finite-difference time-domain algorithm formulated in a 3D curvilinear coordinate system in order to determine the EM field distribution in a PC optical recording stack and to study thermal cross-track cross-talk effects. From the EM field, the energy that is absorbed by the medium is calculated. This absorbed energy is converted into heat and is used as the source term in the thermal diffusion equation. To obtain the temperature distribution in the medium, Peng and Mansuripur solved this equation numerically by using the alternating-direction implicit finite-difference technique. Nishi et al. [50] used a finite-difference time-domain model based on the Lorentz dispersion model published by Judkins and Ziolkowski [37] to compute the 3D absorbed energy distribution.

In this paper we also present a model in which we combine an optical model and a thermal model. To calculate the EM field in a multilayered recording stack, we will use the $2\frac{1}{2}$D model by Brok and Urbach [8]. In that paper, similar to Yeh et al. [71], the diffraction of a 3D incident spot on a 2D configuration, by means of a plane-wave expansion of the spot, was also considered. But the sampling is done such that the plane waves can be divided into sets that, for the given period of the grating, consist of waves that are orders of each other. This considerably reduces the number of scattering problems that has to be solved. The superposition of the plane waves in each set yields an incident field that is, apart from a phase shift,

periodic. The interaction of this incident field with the periodic grating can be computed by solving a single boundary-value problem (BVP). This BVP is derived on a 2D computational box that is one period wide and is called a unit cell. Instead of approximative absorbing boundary conditions, exact radiation conditions for the scattered near field are used. The solution of the BVP is computed with the finite-element method (FEM). To calculate the absorbed EM energy in a 3D neighborhood of the unit cell that is illuminated by the spot and that is relevant for the heat diffusion problem, one must first extend the solution of the BVPs from the unit cell to this 3D region by using the property that the fields are, apart from a phase shift, periodic. After this, the extended fields are added coherently to compute the total EM field in the 3D region of interest.

In our model, both the total EM field and the temperature distribution are calculated with the FEM. All finite-element computations are performed with the SEPRAN [58] finite-element package. Besides the fact that a lot is known about its mathematical properties, the FEM has certain advantages over other methods. The main advantage is that all kinds of geometries, such as bumped layers, can be simulated. The shape of the interfaces is not restricted, and kinks are permitted. Furthermore, the presence of metals with negative real electric permittivity does not cause any problem. For configurations that are of the order of the wavelength such as in the problem studied in this paper, a relative error in the total field, measured in the energy norm, of less than 1%, requires a mesh of approximately 20 elements per wavelength (measured in the material). However, when the configuration is many wavelengths large, more elements per wavelength are needed to prevent the accumulation of phase errors.

Owing to the fact that the 3D scattering problem is solved by expanding the incident field into fields that are periodic apart from a phase shift and by solving for each of these incident fields a 2D problem on the unit cell, the systems of equations to be solved are sufficiently small for a direct method (Gaussian elimination) to be applied. By the use of a direct method, it is guaranteed that the correct solution is always obtained.

In the present model of the recording process, the spot is considered to be turned on continuously for a given period of time. For a given stack geometry, the absorbed energy in the medium is derived and used as heat source in the thermal diffusion equation. Changes in the optical properties of the medium due to the heating by the spot are not taken into account.

The content of this paper is as follows. In Section 4.2 we consider the scattering of an arbitrary 3D incident field by a one-dimensional diffraction grating. In particular, we discuss how the solutions of the scattering problems on the unit cell are extended to the 3D region of interest for the thermal problem. In Section 4.3 we discuss how the acquired absorbed energy distribution, i.e., the heat source, is integrated into the 3D thermal diffusion model. We conclude this paper with a benchmark study in which we com-

pare our model qualitatively for a stationary spot with that of Peng and Mansuripur. Finally, we consider land and groove recording for the Blu-ray Disc.

4.2   Scattering of a focused spot by a one-dimensional diffraction grating

Consider a periodic grating structure as shown in Figure 4.1. With respect to a Cartesian coordinate system (x, y, z) the grating is assumed to be p periodic in the x direction and translation invariant parallel to the y axis. The z axis coincides with the optical axis of the illumination system. All materials are nonmagnetic; hence the magnetic permeability $\mu = \mu_0$ everywhere. Let the 2D unit cell Ω be the region in the plane $y = 0$ defined by

$$\Omega = \left\{ (x, z) \Big| -\frac{p}{2} < x < \frac{p}{2}, a < z < b \right\}. \tag{4.1}$$

The planes $z = a$ and $z = b$ are chosen such that $z < a$ and $z > b$ are half-spaces in which the electric permittivity ϵ is constant and such that Ω has minimal area.

Let the electric field $\mathbf{E}^i$ of the incident spot be given in a certain plane $z = z_i$ above the grating. Let $\mathcal{F}(\mathbf{E}^i)(k_x, k_y, z_i)$ be the Fourier transform of $\mathbf{E}^i$ with respect to x and y in the plane $z = z_i$:

$$\mathcal{F}(\mathbf{E}^i)(k_x, k_y, z_i) = \int_{-\infty}^{\infty} \int_{-\infty}^{\infty} \mathbf{E}^i(x, y, z_i) \exp[-i(k_x x + k_y y)] \, dx \, dy. \tag{4.2}$$

The inverse Fourier transform yields

$$\mathbf{E}^i(x, y, z_i) = \frac{1}{4\pi^2} \int_{-\infty}^{\infty} \int_{-\infty}^{\infty} \mathcal{F}(\mathbf{E}^i)(k_x, k_y, z_i) \exp[i(k_x x + k_y y)] \, dk_x \, dk_y, \tag{4.3}$$

which corresponds with a plane-wave expansion of the incident field with wave vectors $\mathbf{k}$ of which k_x and k_y are the components along the x and y axis, respectively. The time dependence is given by the factor $\exp(-i\omega t)$, which is omitted from all formulas.

We will always choose the branch of the complex square root $z^{1/2}$ such that the cut is along the negative real axis and such that, for positive real z, $z^{1/2} > 0$ and $(-z)^{1/2} = +iz^{1/2}$. Because all waves of the incident field are propagating downward and since the time dependence of the fields is assumed to be given by $\exp(-i\omega t)$, it follows that the z component of the wave vectors $\mathbf{k}$ in the plane wave expansion of the incident field is given by $k_z = -\left[\omega^2 \epsilon_0 \mu_0 \epsilon_u - (k_x^2 + k_y^2) \right]^{1/2}$, where ϵ_u is the relative electric permittivity

of the material in the upper homogeneous half-space $z > b$. The incident field in any other plane $z =$ constant is thus given by

$$\mathbf{E}^i(x, y, z) = \frac{1}{4\pi^2} \int_{-\infty}^{\infty} \int_{-\infty}^{\infty} \mathcal{F}(\mathbf{E}^i)(k_x, k_y, z_i)$$
$$\times \exp\{i[k_x x + k_y y + k_z(z - z_i)]\} \, dk_x \, dk_y. \quad (4.4)$$

We rewrite this as follows:

$$\mathbf{E}^i(x, y, z) = \frac{1}{4\pi^2} \int_{-\infty}^{\infty} \int_{-\infty}^{\infty} \mathcal{F}(\mathbf{E}^i)(k_x, k_y, z_i) \exp\{i[k_x x + k_y y + k_z(z - z_i)]\} \, dk_x \, dk_y$$

$$= \frac{1}{4\pi^2} \sum_{m=-\infty}^{\infty} \int_{-\infty}^{\infty} \int_{-\pi/p + 2\pi m/p}^{\pi/p + 2\pi m/p} \mathcal{F}(\mathbf{E}^i)(k_x, k_y, z_i)$$
$$\times \exp\{i(k_x x + k_y y + k_z(z - z_i))\} \, dk_x \, dk_y$$

$$= \frac{1}{4\pi^2} \sum_{m=-\infty}^{\infty} \int_{-\infty}^{\infty} \int_{-\pi/p}^{\pi/p} \mathcal{F}(\mathbf{E}^i)\left(k_x + \frac{2\pi m}{p}, k_y, z_i\right)$$
$$\times \exp\left\{\left[i\left(k_x + \frac{2\pi m}{p}\right)x + ik_y y + k_z^m(z - z_i)\right]\right\} \, dk_x \, dk_y$$

$$= \int_{-\infty}^{\infty} \int_{-\pi/p}^{\pi/p} \mathbf{E}^i_{k_x, k_y}(x, z) \exp[i(k_x x + k_y y)] \, dk_x \, dk_y, \quad (4.5)$$

where

$$k_z^m = -\left[\omega^2 \epsilon_0 \epsilon_u \mu_0 - (k_x + 2\pi m/p)^2 - k_y^2\right]^{1/2},$$

and

$$\mathbf{E}^i_{k_x, k_y}(x, z) \exp[i(k_x x + k_y y)] = \frac{1}{4\pi^2} \sum_{m=-\infty}^{\infty} \mathcal{F}(\mathbf{E}^i)\left(k_x + \frac{2\pi m}{p}, k_y, z_i\right)$$
$$\times \exp\left[i\left(k_x + \frac{2\pi m}{p}\right)x + ik_y y + ik_z^m(z - z_i)\right]. \quad (4.6)$$

The field $\mathbf{E}^i_{k_x, k_y}(x, z)$ is p-periodic with respect to x and is independent of y. The field (4.6) depends harmonically on y and is, apart from a phase shift, p periodic in x.

Since the incident field satisfies the source-free Maxwell equations in the upper half-space,

$$\nabla \times \mathbf{E}^i = i\omega\mu_0 \mathbf{H}^i, \quad (4.7)$$

$$\nabla \times \mathbf{H}^i = -i\omega\epsilon_0\epsilon_u \mathbf{E}^i, \quad (4.8)$$

we have

$$\mathcal{F}(\mathbf{H}^i)(k_x, k_y, z) = \frac{\mathbf{k}}{\omega\mu_0} \times \mathcal{F}(\mathbf{E}^i)(k_x, k_y, z). \quad (4.9)$$

For the magnetic field component of the incident spot $\mathbf{H}^i$, we can therefore write

$$\mathbf{H}^i(x, y, z) = \int_{-\infty}^{\infty} \int_{-\pi/p}^{\pi/p} \mathbf{H}^i_{k_x, k_y}(x, z) \exp[i(k_x x + k_y y)] \, dk_x \, dk_y, \qquad (4.10)$$

where

$$\mathbf{H}^i_{k_x, k_y}(x, z) \exp[i(k_x x + k_y y)] =$$

$$\frac{1}{4\pi^2} \sum_{m=-\infty}^{\infty} \frac{\mathbf{k}^m}{\omega \mu_0} \times \mathcal{F}(\mathbf{E}^i)\left(k_x + \frac{2\pi m}{p}, k_y, z_i\right)$$

$$\times \exp\left[i\left(k_x + \frac{2\pi m}{p}\right)x + ik_y y + ik_z^m(z - z_i)\right].$$

$$(4.11)$$

Here $\mathbf{k}^m = \left(k_x + 2\pi m/p, k_y, k_z^m\right)$. We have thus written the electric and magnetic components of the incident spot as an integral over k_x and k_y of the fields

$$\mathbf{E}^i_{k_x, k_y}(x, z) \exp[i(k_x x + k_y y)], \qquad (4.12)$$

$$\mathbf{H}^i_{k_x, k_y}(x, z) \exp(i(k_x x + k_y y)], \qquad (4.13)$$

where $\mathbf{E}^i_{k_x, k_y}(x, z)$ and $\mathbf{H}^i_{k_x, k_y}(x, z)$ are p periodic in x. The integral extends over $\mathbb{B} \times \mathbb{R}$, where $\mathbb{B}$ is the one-dimensional Brillouin zone, defined by

$$\mathbb{B} = \left\{k_x \,\middle|\, -\frac{\pi}{p} < k_x < \frac{\pi}{p}\right\}. \qquad (4.14)$$

Let $\epsilon(\mathbf{r})$ denote the relative (in general, complex-valued) electric permittivity at position $\mathbf{r} = (x, y, z)$. Then ϵ is p periodic with respect to x and independent of y. It then follows from Bloch's theorem that for each of the incident fields (4.12), (4.13), the corresponding scattered fields are, apart from a phase shift, p periodic in x and harmonic in y for the same k_x and k_y as the incident field. Hence the total EM field can, similarly to the incident and the scattered fields, be written as an integral:

$$\mathbf{E}^{\text{tot}}(x, y, z) = \int_{-\infty}^{\infty} \int_{-\pi/p}^{\pi/p} \mathbf{E}^{\text{tot}}_{k_x, k_y}(x, z) \exp[i(k_x x + k_y y)] \, dk_x \, dk_y, \qquad (4.15)$$

$$\mathbf{H}^{\text{tot}}(x, y, z) = \int_{-\infty}^{\infty} \int_{-\pi/p}^{\pi/p} \mathbf{H}^{\text{tot}}_{k_x, k_y}(x, z) \exp[i(k_x x + k_y y)] \, dk_x \, dk_y. \qquad (4.16)$$

where $\mathbf{E}^{\text{tot}}_{k_x, k_y}(x, z)$ and $\mathbf{H}^{\text{tot}}_{k_x, k_y}(x, z)$ are p periodic in x and independent of y.

It is shown in Reference [8] that the field $\mathbf{E}^{\text{tot}}_{k_x,k_y}(x,z)$, $\mathbf{H}^{\text{tot}}_{k_x,k_y}(x,z)$ can be derived from the solution of a BVP on Ω with right-hand side derived from the incident field $\mathbf{E}^{i}_{k_x,k_y}(x,z)$, $\mathbf{H}^{i}_{k_x,k_y}(x,z)$. At interfaces between different materials across which ϵ is discontinuous, the tangential components of $\mathbf{E}^{\text{tot}}_{k_x,k_y}$ and $\mathbf{H}^{\text{tot}}_{k_x,k_y}$ are continuous. For every (k_x,k_y), the corresponding BVP consists of a coupled system of two linear second-order partial differential equations in terms of the axial components $\hat{\boldsymbol{i}}_y \cdot \mathbf{E}^{\text{tot}}_{k_x,k_y}$ and $\hat{\boldsymbol{i}}_y \cdot \mathbf{H}^{\text{tot}}_{k_x,k_y}$ only, with exact radiation conditions on the lower and upper boundaries $z = a$ and $z = b$, respectively, and two periodic boundary conditions on the boundaries $x = \pm p/2$. This BVP is equivalent to the Maxwell equations for the given (k_x,k_y). The radiation boundary conditions are derived by using a plane-wave expansion of the reflected and the total fields in the upper and lower half-spaces. These boundary conditions are nonlocal, since they are formulated in terms of Fourier series. The series have infinitely many terms because they contain contributions not only of the propagating plane waves but also of the evanescent waves. The series converge slowly so that a direct numerical summation would be time-consuming. However, as has been explained in Reference [65], the general term of the series can be expanded asymptotically in terms of inverse powers of the Fourier index m, and the sum of the series that is thus obtained can be summed analytically. The series whose terms consist of the remainders of the asymptotic expansion still have to be summed numerically, but these series converge much faster than the original series. In this way, a very efficient implementation of the radiation boundary conditions is obtained.

We remark here that the expressions given in Brok and Urbach [8] for the nonlocal boundary conditions are correct only if the dielectric permittivity is continuous across the upper and lower boundaries of the computational domain. But in the more general case that the computational domain is chosen such that ϵ is different on both sides of these boundaries, the expressions should actually be slightly modified. In the computer code that was used to obtain the results described in Brok and Urbach [8] and in the present paper, the correct more general expressions were implemented.

The advantage of the formulation in terms of the axial field components $\hat{\boldsymbol{i}}_y \cdot \mathbf{E}^{\text{tot}}_{k_x,k_y}$ and $\hat{\boldsymbol{i}}_y \cdot \mathbf{H}^{\text{tot}}_{k_x,k_y}$ is that these components are always tangential to all interfaces; hence they are continuous everywhere. Therefore, in the FEM, one can use standard (so-called H^1) linear elements. A drawback of this approach is the loss of accuracy when the other field components are computed, since they must be obtained by differentiation of the axial components.

The incident field is computed with the package DIFFRACT [21] for a TE or a TM polarized plane-wave or a Gaussian beam that is focused by a positive lens of high numerical aperture (NA). TE means that the electric

field of the plane-wave or Gaussian beam that is incident on the lens is parallel to the grooves, and TM means that the magnetic field is parallel to the grooves. In the calculation of the field in the focal plane $z = z_i$, the rotation of the field vectors is taken into account by use of the theory of Ignatowsky [34] and Richards and Wolf [55]. The focused spot therefore is not perfectly TE or TM polarized, but is only predominantly TE or TM polarized. DIFFRACT gives only the E_x^i and E_y^i components of the incident field, whereas to solve our BVPs we need the E_y^i and H_y^i components. Both E_x^i and E_y^i can be written as a superposition of plane waves in the plane $z = z_i$, as in Equation (4.3). It then follows from $\mathcal{F}(\mathbf{E^i}) \cdot \mathbf{k} = 0$ that

$$\mathcal{F}(E_z^i) = -\frac{1}{k_z}\left[k_x \mathcal{F}(E_x^i) + k_y \mathcal{F}(E_y^i)\right]. \tag{4.17}$$

The magnetic incident field $\mathbf{H}^i$ and, in particular, H_y^i are then found with Faraday's Law [Equation (4.7)].

The double integrals (4.5) and (4.10) with $z = z_i$ are discretized on a grid (k_x^i, k_y^j) in $\mathbb{B} \times \mathbb{R}$. The fast Fourier transform (FFT) is used to compute the amplitudes $\mathcal{F}(\mathbf{E}^i)\left(k_x^i, k_y^j, z_i\right)$. We choose the mesh distance Δk_x of the FFT grid such that $2\pi/p$ is a multiple of Δk_x, i.e., such that

$$\frac{2\pi}{p} = \nu \Delta k_x, \tag{4.18}$$

for some integer ν. Then, for every grid point (k_x^i, k_y^j) that is in $\mathbb{B} \times \mathbb{R}$, we find that the points that are the higher orders of (k_x^i, k_y^j) can be written as

$$\left(k_x^i + \frac{2\pi m}{p}, k_y^j\right) = \left(k_x^{\nu m}, k_y^j\right), \tag{4.19}$$

where m is an integer (see Figure 4.2). We conclude that, owing to the fact that Δk_x is chosen such that $2\pi/p$ is a multiple of Δk_x, the higher orders of a grid point of the FFT grid that is in $\mathbb{B} \times \mathbb{R}$ are also in the FFT grid.

Therefore the FFT grid of the spot is divided into the following sets:

$$\left\{\left(k_x^i + \frac{2\pi m}{p}, k_y^j\right), \quad m \text{ integer}\right\}, \tag{4.20}$$

where (k_x^i, k_y^j) is a grid point that is inside $\mathbb{B} \times \mathbb{R}$. The sum of plane waves in each set is, apart from a phase shift, p periodic in x, and therefore this sum can be taken as an incident field for the BVP corresponding to (k_x^i, k_y^j). In this way the number of BVPs that have to be solved is minimum and equal to the number of grid points of the FFT grid that are inside the set $\mathbb{B} \times \mathbb{R}$.
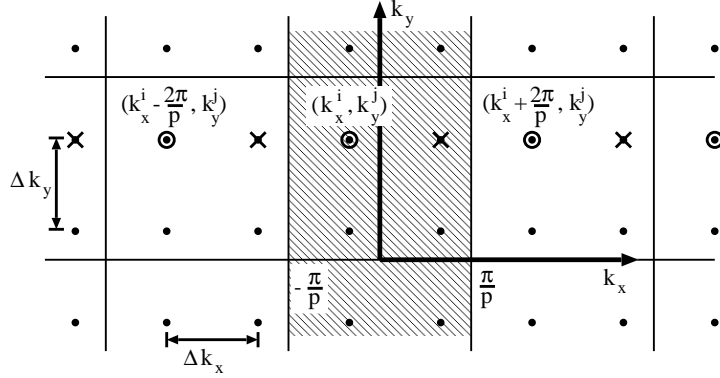
Figure 4.2: *Section of (k_x, k_y) space showing a fragment of the Brillouin zone $\mathbb{B} \times \mathbb{R}$ (hatched). The grid distance Δk_x is taken such that $2\pi/p$ is a multiple of Δk_x (in the figure $2\pi/p = 2\Delta k_x$). For clarity, the spacing in k_y direction, Δk_y, is chosen equal to Δk_x. The encircled points, on the one hand, and the crossed grid points, on the other hand, are sets of grid points that are each other's order.*

For every pair (k_x^i, k_y^j) in $\mathbb{B} \times \mathbb{R}$, the BVP is solved with the FEM. A triangular grid is generated for the unit cell, and piecewise linear basis functions are used for the interpolation of the solution. For sufficient accuracy, around twenty mesh points per wavelength (measured in the material) are taken. The resulting large matrix is complex valued and, in general, nonsymmetric and non-Hermitian and is partially nonsparse owing to the nonlocal boundary conditions at $z = a$ and $z = b$. Because the matrix is relatively small, a direct solver is used.

The formulas (4.15) and (4.16) for the total EM field do not only apply to points in the unit cell but are also valid for arbitrary (x, y, z). For all positive and negative integers μ, ν, the total EM field in a strip S,

$$S := \left\{ (x, y, z) | \left(\mu - \frac{1}{2} \right) p \le x \le \left(\mu + \frac{1}{2} \right) p; \; y = \nu \Delta y \right\}, \qquad (4.21)$$

is given by

$$\mathbf{E}^{\text{tot}}(\bar{x} + \mu p, y, z) = \int_{-\infty}^{\infty} \int_{-\pi/p}^{\pi/p} \mathbf{E}_{k_x, k_y}^{\text{tot}}(\bar{x}, z)$$
$$\times \exp[ik_x(\bar{x} + \mu p) + ik_y \nu \Delta y] \, \mathrm{d}k_x \, \mathrm{d}k_y, (4.22)$$

$$\mathbf{H}^{\text{tot}}(\bar{x} + \mu p, y, z) = \int_{-\infty}^{\infty} \int_{-\pi/p}^{\pi/p} \mathbf{H}_{k_x, k_y}^{\text{tot}}(\bar{x}, z)$$
$$\times \exp[ik_x(\bar{x} + \mu p) + ik_y \nu \Delta y] \, \mathrm{d}k_x \, \mathrm{d}k_y, (4.23)$$

where $-p/2 < \bar{x} < p/2$. Hence the extension of the total EM field from the unit cell to other cells in the plane $y = 0$ and in other planes $y = \nu \Delta y$ requires that the fields corresponding to every (k_x, k_y) in $\mathbb{B} \times \mathbb{R}$ are multiplied by the
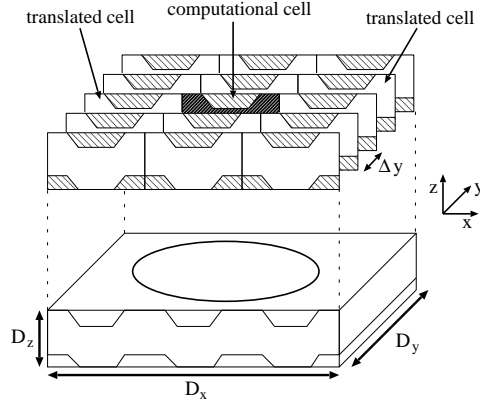
Figure 4.3: *Extended geometry. The cell on which the BVPs are formulated is called the computational cell. The extended region is taken large enough to contain at least the region in which the intensity of the laser spot is essentially nonzero.*

factor $\exp[i(k_x \mu p + k_y \nu \Delta y)]$ for appropriate integers μ and ν. Subsequently, the integrals (4.15) and (4.16) over $\mathbb{B} \times \mathbb{R}$ have to be computed. Note that owing to the (k_x, k_y) dependency of the exponential multiplication factor, the extension to a 3D region of interest cannot be done after the total EM field in the unit cell has been calculated. Instead, each periodic solution must be extended separately, and after that the integral must be computed.

To be more specific, the following procedure has been implemented. The total EM field for the unit cell is extended to a region Λ_{opt} with dimensions $(D_x, D_y, D_z = b - a)$ that are so large that outside of Λ_{opt} the spot can be considered to be negligible. For the discretization in the y direction, a sufficiently small step size Δy is chosen; see Figure 4.3.

The unit cell on which the BVP is formulated will from this point onwards be referred to as the computational cell. For every pair (k_x^i, k_y^j) in $\mathbb{B} \times \mathbb{R}$, the corresponding BVP is solved on the computational cell with as incident field $\mathbf{E}_{k_x^i, k_y^j}^i (x, z)$, $\mathbf{H}_{k_x^i, k_y^j}^i (x, z)$. For fixed k_y^j the solutions corresponding to all k_x^i are extended to the neighboring cells that are in the same plane $y = 0$ as the computational cell by means of multiplication by the appropriate factor $\exp(ik_x^i \mu p)$, after which the extended fields are added coherently. The thus obtained accumulated field in the plane $y = 0$ corresponding to the fixed k_y^j is then extended to the cells in y direction by multiplication by the factor $\exp(ik_y^j \nu \Delta y)$. This procedure is carried out for all k_y^j, and, by coherent summation of all these extended fields, the total EM field in all cells of interest in a neighborhood of the spot is obtained.

We assume that, in those layers of the recording stack that are absorbing, the absorbed EM energy in Λ_{opt} is transformed entirely into heat. Hence the rate Q (Jm^{-3}) at which heat is generated per unit volume, owing to the

absorption of light, is given by

$$Q(\mathbf{r}) = \frac{1}{2}\omega\epsilon_0 \text{Im}\left[\epsilon(\mathbf{r})\right]|\mathbf{E}^{\text{tot}}(\mathbf{r})|^2, \qquad (4.24)$$

where $\text{Im}\left[\epsilon(\mathbf{r})\right]$ denotes the imaginary part of the relative electric permittivity at position $\mathbf{r}$.

4.3   Thermal model

The use of a $2\frac{1}{2}$D optical model is limited by the fact that changes in the optical properties of the medium and thus in the absorbed energy distribution, owing to the heating of the laser spot, cannot be taken into account in the 3D thermal model because these changes are 3D. The effect of these changes on the light distribution in the stack and, in particular, on the absorbed energy is, in general, small.

   The laser spot is contiguously turned on between $t = 0$ and $t = t_e$. The disc rotates at the speed v (meters per second). In the thermal model a 3D computational box Λ_{temp} with dimensions (L_x, L_y, L_z) is used. The chosen coordinate axes are parallel to the axes of the coordinate system used in the optical model but, in contrast to the latter, are attached to the disc. Hence the coordinate system used in the heat problem moves with speed v along the grooves in the positive y direction with respect to the coordinate system of the optical model. In the x direction the computational box Λ_{temp} consists of a grooved structure of equal width as the extended region Λ_{opt} of the optical model. This structure is further extended ungrooved to the exterior of Λ_{temp}.
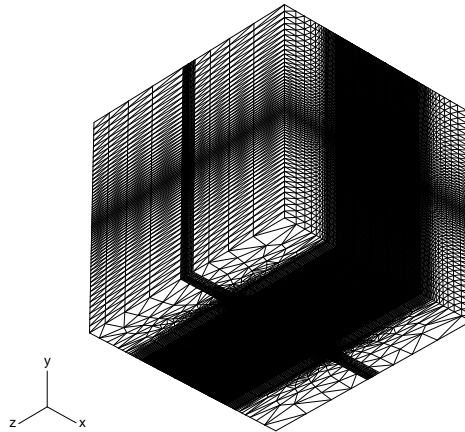
Figure 4.4: *Tetrahedral mesh used in the thermal calculations. In the region in which the absorbed energy is mapped, the grid size is taken of the same order in size as that of the triangular mesh of the optical model.*

The temperature rise above ambient in the disc, $T(\mathbf{r}, t)$ (degrees Celsius), satisfies the heat diffusion equation:

$$\rho c \frac{\partial T}{\partial t} - \nabla \cdot [\kappa \nabla T] = Q(x, y + vt, z), \tag{4.25}$$

where κ [W/m°C] is the thermal conductivity, ρ [kg/m^3] is the density, and c [J/kg°C] is the specific heat. These quantities are in general different in different layers of the optical disc but are taken constant in each layer. Hence they are assumed to be independent of temperature in the temperature range of interest. Note that by choosing the coordinate system to move with the disc, no additional convection term is introduced, but the source term becomes time-dependent. The heat problem is taken to be adiabatic, and therefore we take as boundary condition

$$\frac{\partial T}{\partial n} = 0, \tag{4.26}$$

where n denotes the outward-pointing unit normal at any of the outer surfaces of Λ_{temp}. The dimensions of Λ_{temp}, in particular the lengths of the ungrooved continuations in x direction, are chosen large enough to ensure that the choice of boundary conditions does not influence the solution.

In Equation (4.25) it is assumed that the temperature rises because of the total generated heat. In fact, a considerable fraction of Q is latent heat, which does not contribute to the rise in temperature but instead is used for the solid-to-liquid transition during melting of the PC material.

The diffusion problem [Equations (4.25) and (4.26)] is 3D and time dependent. It could, in principle, be reduced to a set of uncoupled time-dependent problems on the unit cell Ω by Fourier expanding Q and T in terms of functions that are periodic in x apart from a phase shift, as was done for the optical problem. But since the diffusion problem is a BVP for a single real-valued function, the time-dependent 3D problem can just as well be efficiently solved directly on the 3D region.

On the region Λ_{temp} a mesh is generated, consisting of tetrahedral elements whose size increases toward the edges; see Figure 4.4. The coarseness is taken such that, in the subregion Λ_{opt} of Λ_{temp}, the fineness of the tetrahedral mesh is approximately of the same order in size as that of the triangular mesh used in the EM field calculation. In points of Λ_{opt} the absorbed energy Q is mapped onto the mesh for Λ_{temp} by means of a linear interpolation; see Figure 4.5. Each nodal point of the tetrahedral grid is first interpolated within the corresponding triangles of two of the expanded cells in planes differing by the distance Δy of the optical mesh, by use of linear basis functions. The obtained interpolated values are then once more linearly interpolated in y direction to find the absorbed energy in the point of interest. In points of Λ_{temp} outside of Λ_{opt}, the absorbed energy is taken equal to zero.
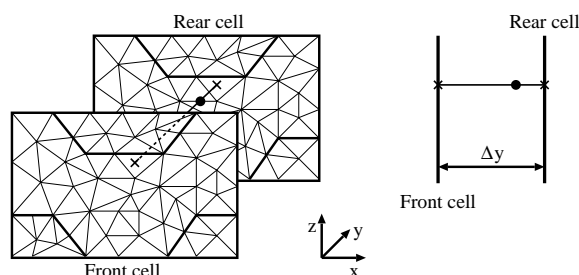
Figure 4.5: *To compute the absorbed energy in a nodal point (●) of the tetrahedral mesh for the thermal model, we first calculate the values in the intersections X with the two enclosing expanded cells of the optical model. These values are linearly interpolated by using the piecewise linear basis functions on the triangles. The absorbed energy in the nodal point (●) is then the linearly interpolated value of the values in the intersection points.*

The temperature problem [Equations (4.25) and (4.26)] is solved by use of the FEM with piecewise linear basis functions. The finite linear system of equations is, for every time step, iteratively solved with the conjugate gradient method. For the time integration the Euler implicit method is used.

4.4 Numerical results

The model described in the preceding sections has been applied to two land-groove configurations. The first configuration is chosen equal to the multilayered stack called 'case C1' by Peng and Mansuripur [53] and is shown in Figure 4.6.

The optical axis coincides with the z axis and is in the middle of Figure 4.6. Hence the center of the spot is at the center of the groove in Figure 4.6, and therefore this case is called groove recording. When the stack is translated over half a period in the x direction, the center of the spot is at the center of the land, and therefore this situation is called land recording. In all simulations the spot is focused in air in the middle of the PC layer, and the disc is at rest.

The track pitch is 720 nm. The groove depth of 50 nm has been exaggerated in order to study to what extent the polarization of the incident spot influences the absorbed energy and the temperature distribution. The material properties of the stack are listed in Table 4.1. The beam that is incident on the aperture of the lens is Gaussian, having its $1/e$ amplitude at the rim of the aperture of the lens. The output power of the laser is 4 mW, of which 86% is captured by the objective lens. The lens has a NA = 0.65 and the wavelength of the incident light $\lambda = 410$ nm.

Before studying a grooved stack, we consider the interaction of a focused spot with an ungrooved version of the multilayer stack. The results of
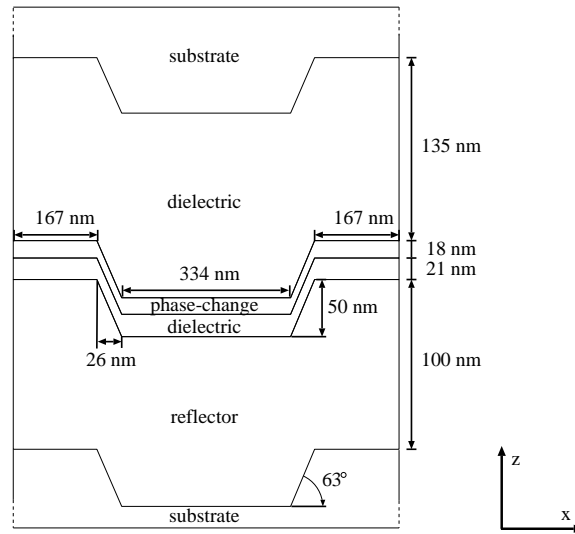
Figure 4.6: *Cross section of the stack as used in configuration C1 according to Peng and Mansuripur [53]. The structure is translation invariant in the y direction.*

the simulations for this configuration are shown in Figures 4.7 and 4.8. In Figure 4.7 the amplitude of the dominant magnetic field component and the absorbed energy distributions are shown for a TM polarized spot, i.e., a spot for which the electric field is predominantly parallel to the x direction. The layers shown in the figures are (from bottom to top) the reflective layer, the first dielectric layer, the PC layer, and, finally, the second dielectric layer. In Figure 4.7a standing waves are clearly visible. It follows from Figure 4.7b that almost all the light is absorbed by the PC layer.

In Figure 4.8a the absorbed energy distribution is shown halfway in the PC layer ($z = 144$ nm) after the extension of the 2D distribution shown in Figure 4.7b and a mapping to the 3D thermal mesh. Figure 4.8b shows the corresponding temperature distributions halfway in the PC layer for TM polarization after $t = 100$ ns.

Table 4.1: *Numerical values for the complex refraction index n, heat capacity ρC and thermal conductivity κ as used in simulations for the configuration of Figure 4.6.*

	n	ρC [J/cm³/°C]	κ [W/cm/°C]
Substrate (polycarbonate)	1.54	1.7	0.0023
Dielectric (ZnS-SiO$_2$)	2.3	2.005	0.0058
PC layer (Ge$_2$Sb$_{2.3}$Te$_5$)	$1.78 + 3.23i$	1.285	0.006
Reflector (Al alloy)	$0.5 + 3.8i$	2.45	0.2

(a) $|H_y|$ (b) absorbed energy
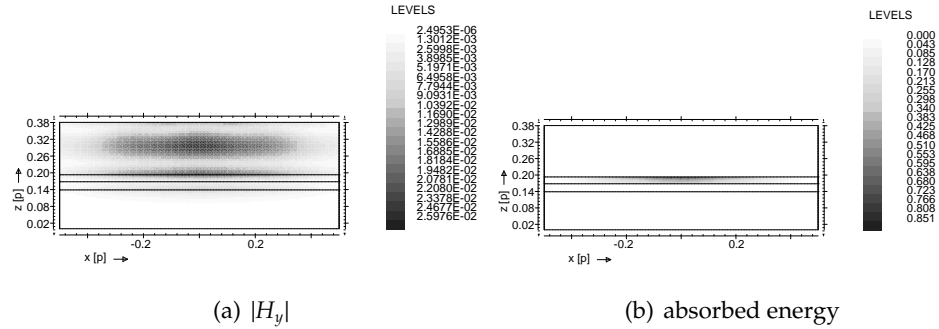
Figure 4.7: *Dominant field components (arbitrary units) and absorbed energy [W/p^3] in the unit cell for a TM polarized spot that is incident on a flat version of the multilayered stack of Figure 4.6. The spot is focused in air in the middle of the PC layer.*

(a)   (b)
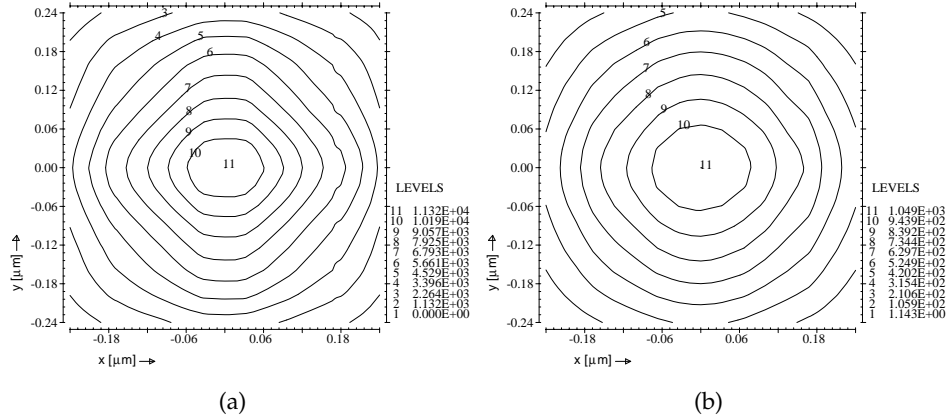
Figure 4.8: *Top view of the absorbed energy [10^4 W/μm^3] and the temperature distribution [°C] halfway in the PC layer for a TM polarized spot incident on a flat version of the stack shown in Figure 4.6. (a) Absorbed energy, (b) temperature distribution.*

Because the multilayer has flat interfaces, the absorbed energy density and temperature distribution in the planes z = constant corresponding to TE polarization are, of course, obtained from those of TM polarization by a counterclockwise rotation over 90 degrees around the z axis.

In Figure 4.9a the temperature distribution is shown in the $y = 0$ plane when a TM polarized spot is incident on the flat multilayer (the $y = 0$ plane contains the center of the spot). Figure 4.9b shows the temperature along the line $x = y = 0$ as a function of the depth coordinate z. It can be seen that there are steep gradients near and within the PC layer. This implies that slightly changing the position of the intersection plane can lead to relatively large differences in the temperature profile. This is important when one compares the results with those found elsewhere in the literature.

(a)   (b)
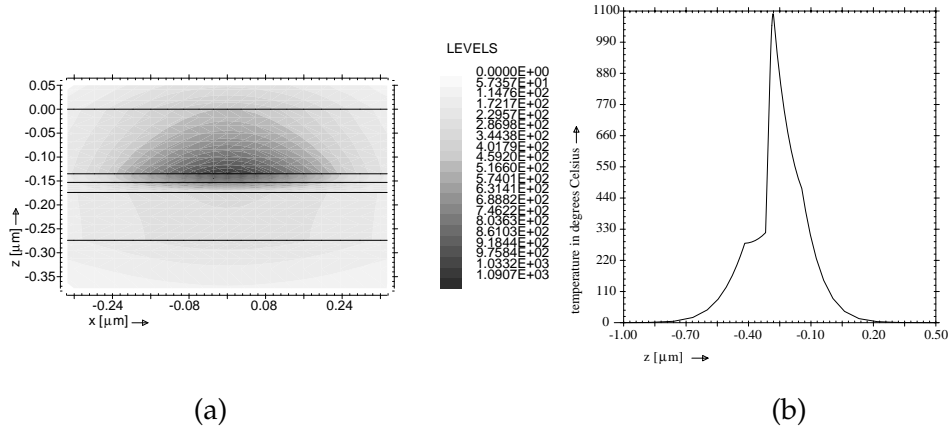
Figure 4.9: *Temperature distribution (°C) for a TM polarized spot (a) in a cross section perpendicular to the groove-direction and (b) a cross section of (a) perpendicular to the interfaces along the optical axis. The stack is that of Figure 4.6 except that the interfaces are flat.*

In Figure 4.10 cross sections through the middle of the PC layer are shown of the absorbed energy distributions for a TE polarized spot and a TM polarized spot that is focused on a groove [Figure 4.10a and 4.10b] and a land [Figure 4.10c and 4.10d] of the configuration shown in Figure 4.6. The cross sectional planes follow the topography of the grooves. The corresponding temperature distributions after the spot has been turned on for 100 ns are shown in Figure 4.11 (these are also cross sections through the middle plane of the PC layer).

Noticeable differences can be observed according to whether the spot is focused on a land or a groove and also between different polarizations. For the absorbed energy of the TE polarized spot, a much smoother profile is found along the edges of the groove than for a TM polarized spot. This holds for both the land- and groove-centered spots. Also, the TM case shows considerably steeper gradients on and near the edges. Besides, a larger number of local maxima are found for the TM polarized spot.

In Figure 4.12 the cross-track temperature distributions in the middle of the PC layer and parallel to the x axis are shown for both polarizations when the focused spot is positioned over either a land or a groove. The sidelobes in the temperature distributions seem to be typical for TM polarized spots. When positioned over a land, both polarizations show steeper gradients near the edges of the groove. When the spot is positioned over a groove, temperatures found on the neighboring lands are higher than temperatures found on the neighboring grooves when the spot is positioned over a land. These higher temperatures of $\approx$ 600 °C imply a possible occurrence of
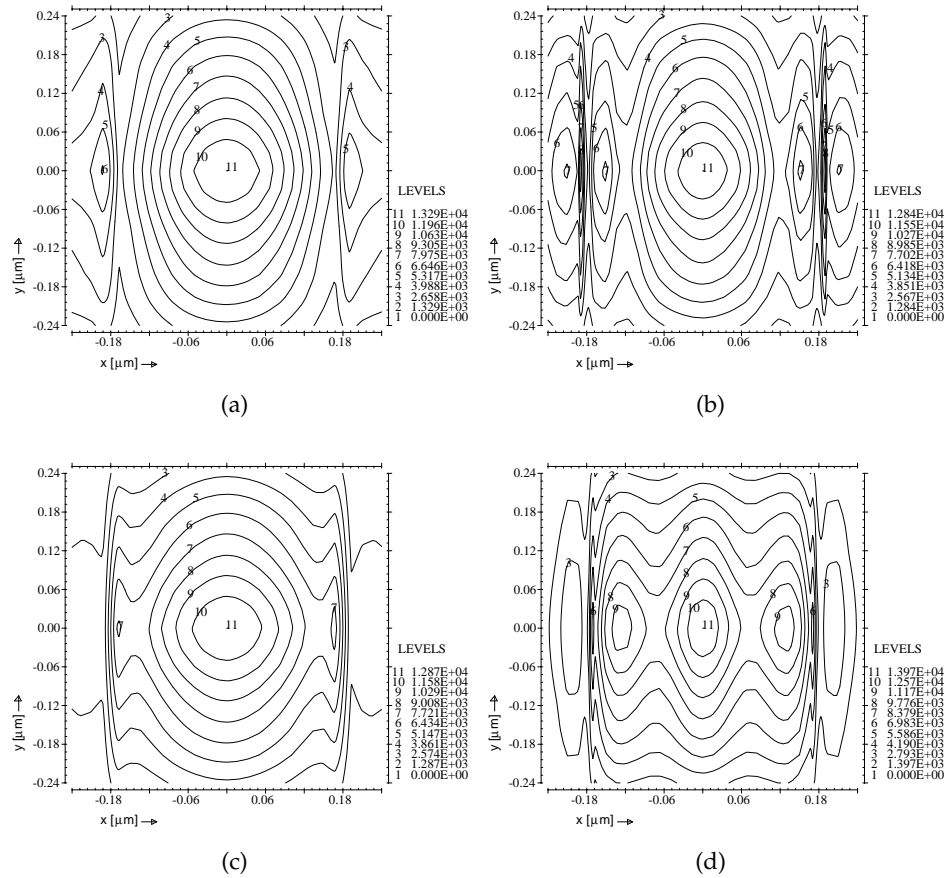
Figure 4.10: *Absorbed energy distributions [10^4 W/μm^3] halfway in the PC layer for a TE and TM polarized spot that is incident on the grooved multilayer of Figure 4.6. Center of the spot is in the groove: (a) TE, (b) TM. Center of the spot is on the land: (c) TE, (d) TM.*

undesirable cross-track cross-talk effects.

The shape of the isotherms as shown in Figure 4.11 and the cross-track temperature distributions of Figure 4.12 are very similar to the corresponding results published by Peng and Mansuripur [53].

In Figures 4.13 and 4.14, temperature distributions are shown in the plane $y = 0$ that is perpendicular to the grooves and contains the center of the spot. In Figure 4.13 the spot is TE polarized, and in Figure 4.14 it is TM polarized. It can be seen that the temperature in the dielectric above the PC layer is quite high.

Finally, we consider the Blu-ray Disc. The numerical values of the physical parameters of the various materials are listed in Table 4.2. In Figure 4.15 a cross section of one period of the multilayer stack of the Blu-ray Disc is shown. The track pitch is only 320 nm. It can be seen that, compared with the stack in Figure 4.6, there is an additional thin layer above the re-
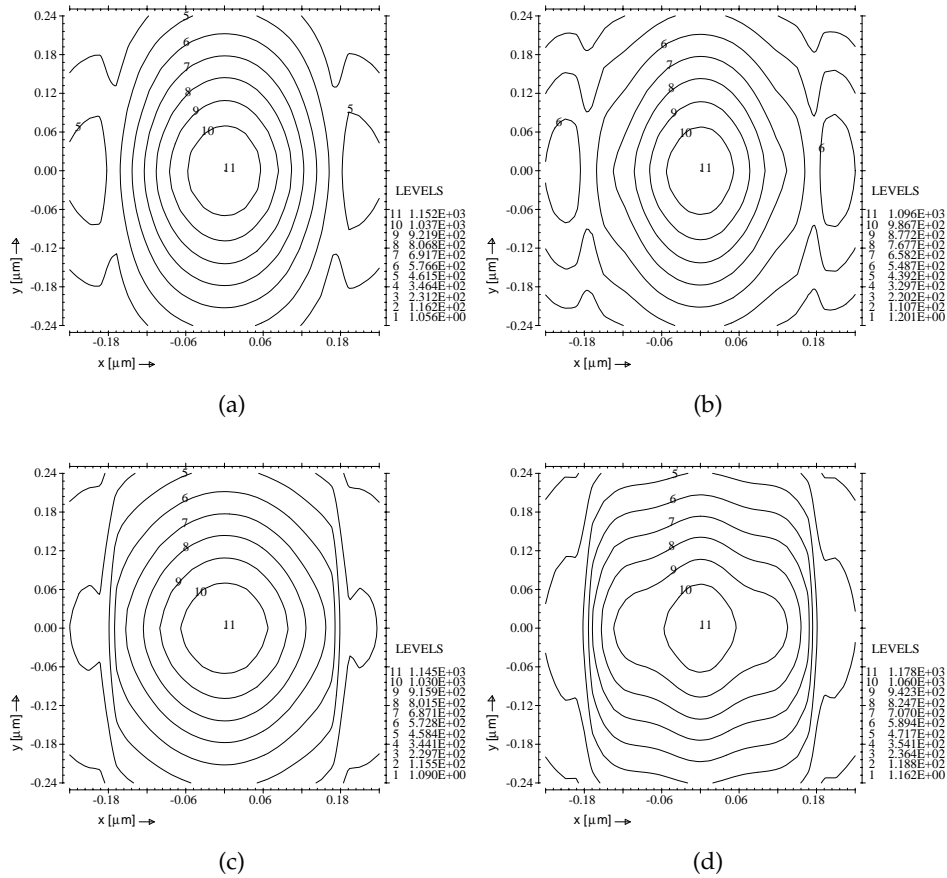
Figure 4.11: *Temperature distributions [°C] halfway in the PC layer for a TE and TM polarized spot that is incident on the grooved multilayer of Figure 4.6. Center of the spot is in the groove: (a) TE, (b) TM. Center of the spot is on the land: (c) TE, (d) TM.*

flector. Furthermore, the PC material and the reflector consist of materials other than in the previous example. The numerical values of the physical parameters of the various materials are listed in Table 4.2. The wavelength is $\lambda = 405$ nm. The output power of the laser is 15 mW. The focusing lens now has NA = 0.85. The spot is again focused in air in the middle of the PC layer. The plane-wave front that is focused by the lens is linearly polarized with the electric field vector parallel to the x direction. Therefore the field of the spot is predominantly TM polarized. Because of the high NA, it is now essential to take the rotation of polarization into account when the light is focused by the lens. As has been remarked before, the spots that we use as an incident field have all been calculated by applying the theory of Ignatowsky [34] and Richards and Wolf [55].

In Figures 4.16 and 4.17 the absorbed energy and temperature distributions after 100 ns are shown in the plane in the middle of the PC

(a)

(b)
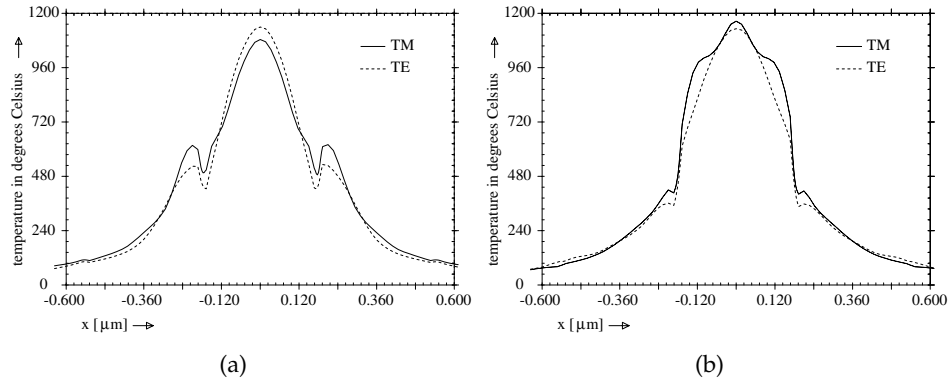
Figure 4.12: *Cross sections of the temperature distributions [°C] halfway in the PC layer as shown in Figure 4.11.*

(a) groove recording

(b) land recording
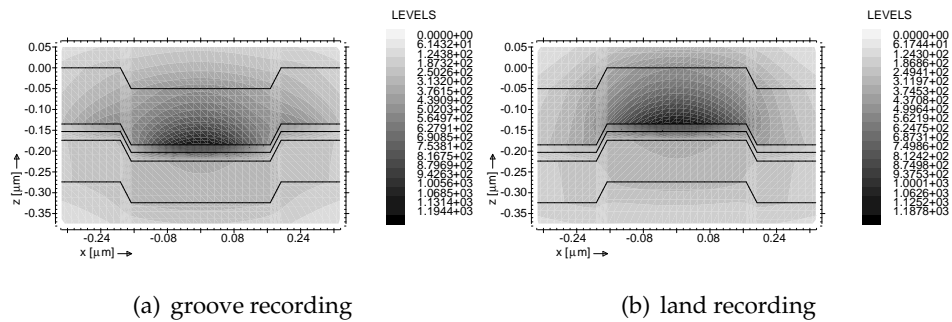
Figure 4.13: *Temperature distribution [°C] for a TE polarized spot in a cross section perpendicular to the groove-direction for the stack of Figure 4.6.*

layer of the Blu-ray Disc (the cross sectional plane follows the topography of the grooves). When the results for groove and land recording in Figures 4.16a and 4.16b are compared to the absorbed energy distributions in Figures 4.10b and 4.10d (for which the incident spot is also predominantly TM polarized), quite large differences can be seen. First of all, owing to the higher NA of the lens, the spots are narrower in the Blu-ray case. Furthermore, for the Blu-ray case the highest absorption values are observed near, or even on, the sloped edges, instead of in the center of the groove or land. In Figure 4.18, cross sections are shown of the temperature in the plane $y = 0$ (this plane contains the center of the spot). The highest temperatures occur for land recording.

(a) groove recording   (b) land recording
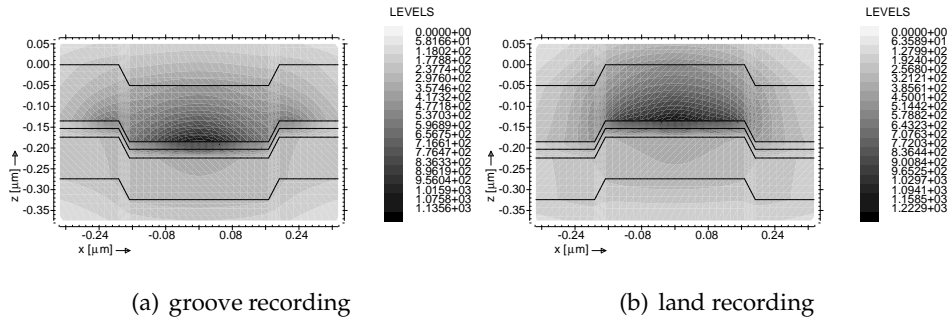
Figure 4.14: *Temperature distribution (°C) for a TM polarized spot in a cross section perpendicular to the groove-direction for the stack of Figure 4.6.*
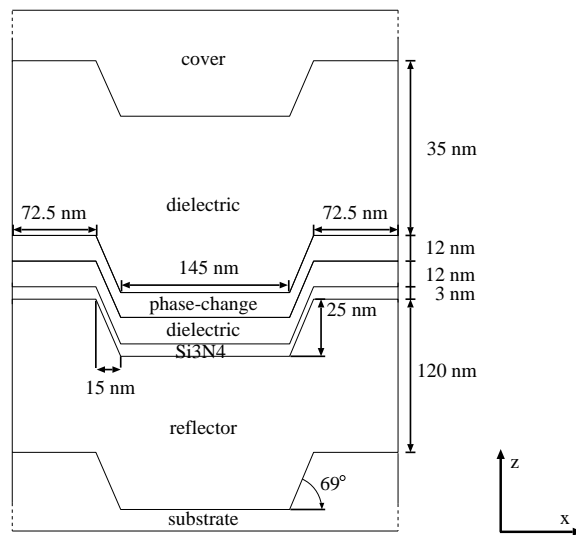
Figure 4.15: *Cross section of the stack as used for the Blu-ray Disc simulation.*

Table 4.2: *Numerical values for the complex refraction index n, heat capacity ρC and thermal conductivity κ as used in the simulations of the Blu-ray Disc.*

	n	ρC [J/cm^3/°C]	κ [W/cm/°C]
Cover	1.55	1.75	0.0025
PC layer (Ge$_6$In$_2$Sb$_{72}$Te$_{20}$)	$1.5 + 3.45i$	1.5	0.05
Dielectric (ZnS-SiO$_2$)	2.3	2.005	0.0058
Si$_3$N$_4$	2.07	1.7	0.08
Reflector (Ag)	$0.173 + 1.999i$	1.9	0.7
Substrate (polycarbonate)	1.62	1.7	0.0023

(a)   (b)
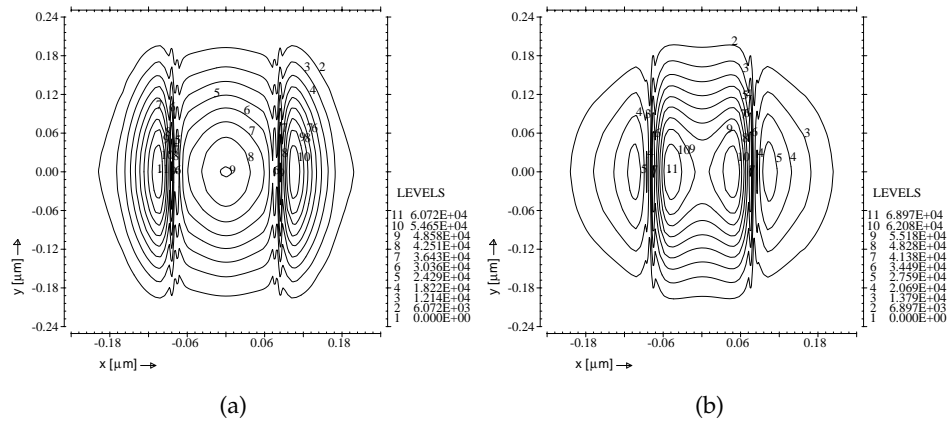
Figure 4.16: *Absorbed energy distributions [10^4 W/μm^3] halfway in the PC layer for a TM polarized spot that is incident on the grooved multilayer for the Blu-ray Disc (stack is shown in Figure 4.15). The NA of the lens is 0.85, the wavelength of the light is 405 nm. (a) Center of the spot is in the groove, (b) center of the spot is on the land.*
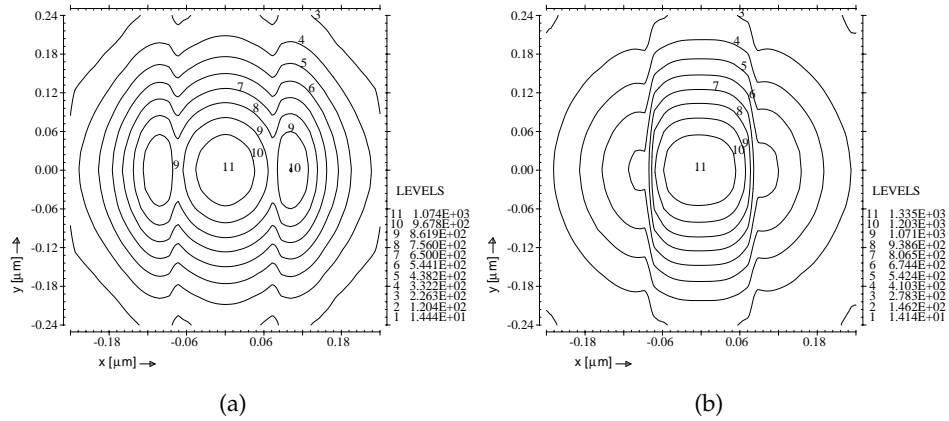
Figure 4.17: *Temperature distributions [°C] halfway in the PC layer for a TM polarized spot that is incident on the grooved multilayer for the Blu-ray Disc of Figure 4.15. (a) Center of the spot is in the groove, (b) center of the spot is on the land.*
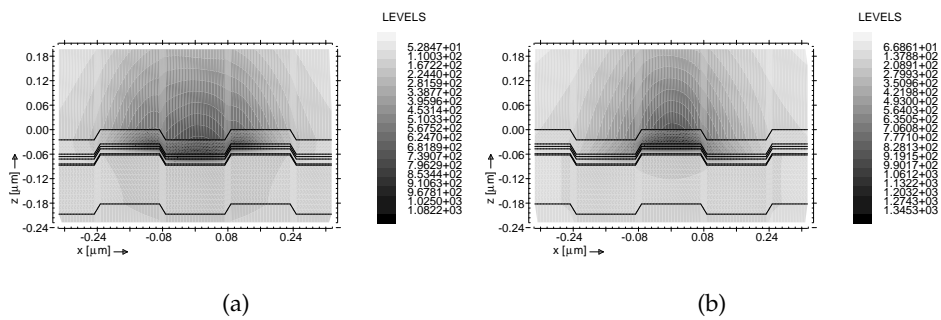
Figure 4.18: *Temperature distribution (°C) for a TM polarized spot in a cross section perpendicular to the groove-direction for the Blu-ray stack of Figure 4.15. (a) Center of the spot is in the groove, (b) center of the spot is on the land.*

4.5   Conclusions

The 2D rigorous diffraction model for the scattering of a 3D incident spot on a 2D periodicly grooved geometry by Brok and Urbach [8] has been successfully modified to obtain the total EM field in a 3D region of interest for optical recording simulations. The optical model has been combined with a 3D thermal model in order to compute the temperature distribution in a grooved multilayer recording stack. The results are found to be in good accordance with results published by C. Peng and M. Mansuripur [53]. Furthermore, results were presented for groove and land recording on a Blu-ray Disc.

CHAPTER 5

Numerical methods for
two-phase Stefan problems

We present a survey of numerical methods for solving melting and solidification problems. Most of the methods mentioned in this chapter have been developed in the general context of phase-change problems and aim at describing the evolution of temperature in time inside a single isolated domain, either implicitly or explicitly keeping track of one (or multiple) interfaces between phases. The goal of this study is to identify a number of numerical techniques that can be used to solve the Stefan problem, as formulated in Chapter 3, inside complex three-dimensional composite domains.

5.1   Introduction

In the past decades, many novel numerical schemes for solving phase-change problems have been developed, and successively improved upon. Although finite volume and finite difference discretizations are still quite popular, (extended) finite element based techniques frequently appear in the recent literature. The excellent paper by Hu and Argyropoulos [33] gives an elaborate review of numerical methods for modeling solidification and melting problems (up until 1996).

The first class of methods they discuss are the fixed grid methods (see also Voller et al. [67] and Basu and Date [4]). Probably the most problematic aspect of the fixed grid methods is the loss of accuracy associated with singularities, which can arise when the moving boundary is too close to a grid point. The mathematical manipulations to resolve this, such as Taylor expansion based interpolations or Lagrange interpolations, are considered to be very lengthy and complicated indeed. However, according to Hu

and Argyropoulos, the major advantage of fixed grid methods is that these methods can efficiently handle problems with multiple phase fronts without much difficulty.

The second class of methods are the variable grid methods. These methods can be either interface-fitting or dynamic. In interface-fitting grid methods, or variable time step methods, a uniform spatial grid, but a non-uniform time step are used. At each new time step, the step size is chosen such that the moving boundary is located on a grid point. In dynamic grid methods, or variable space grid methods, the number of spatial cells are kept constant, and the spatial cells are adjusted in such a way that the moving boundary lies on a particular grid point. Although the adaptive grid overcomes many of the drawbacks of the fixed grid methods, the variable grid methods still mostly suffer from their inherent complexity, in particular for higher dimensional cases.

In Hu and Argyropoulos [33], a selection of methods is discussed that reformulate the phase-change problem in such a way that the Stefan condition (3.2b) is implicitly incorporated in a new set of equations. These equations then hold on the entire region of the fixed domain. They are the apparent capacity method, the effective capacity method, the heat integration method and the source based method. These methods can be quite inaccurate, since in most cases the accuracy is strongly dependent on the time step. The only exception concerning the accuracy issue is the effective capacity method, but unfortunately this method can be very troublesome to implement.

When compared to the previous methods, the enthalpy approach discussed in Section 5.3, according to Alexiades and Solomon [2], Chapter 4.2, can be considered to be the most versatile, convenient, adaptable and easily programmable numerical methods for phase-change problems in one, two or three spatial dimensions. This is mostly due to the fact that the interface location itself is not involved in the computation at all, and both isothermal and mushy problems can be considered. However, there are still problems for which even an enthalpy approach is not suitable. Such is the case for instance for problems involving super-cooling, where the instability of the interface must be studied. Finding a weak formulation is then often impossible, due to the special interface conditions that are imposed. Alternatively, such problems can be solved using a phase-field approach (for instance see Reference [20], Chapter 11, and references therein).

For isothermal problems, a level set approach can also be applied. In the level set method, the position of the moving front is implicitly tracked and is represented by the zero level set of the so-called level set function. The level set method will be discussed in more detail in Section 5.4. Another alternative for the enthalpy method is the so-called temperature approach. In this approach, the enthalpy is written as the sum of sensible and latent heat. As a result, the enthalpy equation can be reformulated as a heat diffusion equation with an additional nonlinear term that accounts for the

latent heat. The temperature approach is addressed in Section 5.5.

Because it is important to be able to validate numerical results, we will first report on an analytical solution method for two-phase Stefan problems. The problem description and most of the notation used are adopted from Reference [33].

5.2   Analytic solution method

Analytic solutions exist for only a select number of phase-change problems. Stefan [63] was the first to solve the simplest phase-change problem possible: the one-dimensional one-phase problem in a semi-infinite region. By 'one-phase' we mean that, for a melting problem, only the liquid phase is 'active' while the other phase stays at the melting temperature, and is 'in-active'. Thus, to put it in other words, only for the 'active' phase the heat diffusion equation has to be solved.

In the context of Stefan problems, a dimensionless number St given by

$$St = \frac{\rho c_l \left(T_l - T_m\right)}{L},\tag{5.1}$$

often appears in the literature. This number, generally known as the Stefan number, governs the rate of melting or solidification in a semi-infinite region. In (5.1), ρc_l is the heat capacity of the liquid, L is the latent heat of fusion and T_l and T_m are the temperatures of the surroundings and the melting point, respectively. Interesting is that the commonly used definition (5.1), which is the sensible heat divided by the latent heat, was introduced by G.S.H. Lock in 1969 [39], not by Josef Stefan.

5.2.1   Neumann's method

In two-phase Stefan problems, both the liquid phase as well as the solid phase are 'active'. If melting of a semi-infinite slab ($0 < x < \infty$) is considered, initially solid at a uniform temperature $T_s < T_m$, and a constant temperature is imposed on the face $x = 0$, with assumptions of constant thermo-physical properties, the problem can be mathematically expressed as follows:

Heat conduction in the liquid region:

$$\frac{\partial T_l}{\partial t} = \alpha_l \frac{\partial^2 T_l}{\partial x^2}, \qquad \text{for } 0 < x < \Gamma(t), t > 0.\tag{5.2}$$

Heat conduction in the solid region:

$$\frac{\partial T_s}{\partial t} = \alpha_s \frac{\partial^2 T_s}{\partial x^2}, \qquad \text{for } \Gamma(t) < x, t > 0.\tag{5.3}$$

Interface temperature:

$$T(\Gamma(t), t) = T_m \quad , \text{for } t > 0. \tag{5.4}$$

Stefan condition:

$$\kappa_s \frac{\partial T_s}{\partial x} - \kappa_l \frac{\partial T_l}{\partial x} = L\rho \frac{d\Gamma}{dt}, \qquad \text{for } x = \Gamma(t), t > 0. \tag{5.5}$$

Initial conditions:

$$T(x, 0) = T_s < T_m, \qquad \text{for } x > 0, \Gamma(0) = 0. \tag{5.6}$$

Boundary conditions:

$$T(0, t) = T_l > T_m, \qquad \text{for } t > 0, \tag{5.7}$$

$$T(x, t) = T_s, \qquad \text{for } x \to \infty, t > 0. \tag{5.8}$$

Here $\alpha_l = \kappa_l / (\rho c_l)$ and $\alpha_s = \kappa_s / (\rho c_s)$ denote the diffusivity of the liquid and the solid phase, respectively.

The exact solution to such a problem was obtained by Neumann in terms of a similarity variable

$$\eta_p = \frac{x}{2\sqrt{\alpha_p t}}, \tag{5.9}$$

where the subscript p can be either l for the liquid phase or s to indicate the solid phase. The final Neumann's solution can be written as:

Interface position:

$$\Gamma(t) = \frac{x\lambda}{\eta_l}. \tag{5.10}$$

Temperature in the liquid phase:

$$T(x, t) = T_l - (T_l - T_m) \frac{\text{erf}(\eta_l)}{\text{erf}(\lambda)}. \tag{5.11}$$

Temperature in the solid phase:

$$T(x, t) = T_s - (T_m - T_s) \frac{\text{erfc}(\eta_s)}{\text{erfc}(\lambda \sqrt{\alpha_l/\alpha_s})}. \tag{5.12}$$

The λ in Equations (5.10) - (5.12) is the solution of the transcendental equation

$$\frac{St_l}{\exp(\lambda^2)\,\text{erf}(\lambda)} - \frac{St_s\,\sqrt{\alpha_s}}{\sqrt{\alpha_l}\exp(\alpha_l\lambda^2/\alpha_s)\,\text{erfc}(\lambda\sqrt{\alpha_l/\alpha_s})} = \lambda\sqrt{\pi}, \tag{5.13}$$

where

$$St_l = \frac{\rho c_l(T_l - T_m)}{L}, \qquad St_s = \frac{\rho c_s(T_m - T_s)}{L}. \tag{5.14}$$

Neumann's solution as presented above exists only for moving boundary problems in the rectangular coordinate system. An exact solution for phase-change problems in cylindrical coordinates as well as several approximative methods can be found in the literature, but we will not discuss them here.

5.3 Enthalpy approach

The most convenient starting point for deriving a numerical scheme for solving the Stefan problem above, is to consider the law of energy conservation in the form of a primitive integral heat balance over arbitrary volumes and time-intervals, as given by

$$\int_t^{t+\Delta t} \frac{\partial}{\partial t}\left(\int_V H dV\right) dt = \int_t^{t+\Delta t} \int_{\delta V} -\mathbf{q} \cdot \mathbf{n} dS dt + \int_t^{t+\Delta t} \int_V Q dV dt. \tag{5.15}$$

Here, H is the energy density (per unit volume), or enthalpy, and $-\mathbf{q} \cdot \mathbf{n}$ is the heat flux *into* the volume V across its boundary δV, $\mathbf{n}$ is the outgoing normal to δV and Q is an internal heat source. The heat conduction equation (3.2a) can be easily derived from (5.15), see for instance Reference [2], Chapter 4.1.

The energy balance (5.15) is valid irrespectively of phase over the whole domain considered, and even for jumps in H or $\mathbf{q}$. Thus, it is more general than the localized differential form

$$H_t + \text{div} \, \mathbf{q} = Q. \tag{5.16}$$

According to the Gauss' divergence theorem, the integral notation (5.15) and the differential form (5.16) are equivalent for smooth H, $\mathbf{q}$ and Q. In case of a phase-change problem, (5.16) can only be interpreted classically (point-wise) in each phase separately, but then in addition a Stefan interface condition (3.2b) is required, making front-tracking necessary.

Alternatively, (5.16) may be interpreted in a weak sense globally. The numerical solution to the discretized form of equation (5.16) via the enthalpy method, is found to approximate the weak solution (see for instance Reference [2], Chapter 4.4). It is for this reason that from this point onwards, as is common in the literature, we consider (5.16).

In general, the enthalpy function H is defined as the integral of the heat capacity with respect to temperature. For problems in which no phase-change occurs, the enthalpy H is equal to the sensible heat, defined by

$$H(T) = \int_{T_{\text{ref}}}^T \rho c(T) dT, \tag{5.17}$$

where ρc is the volumetric heat capacity which depends on temperature, and where T_{ref} is a reference temperature. For problems involving a phase-change the enthalpy is defined as the sum of the sensible and the latent heat. Since the type of material considered influences the form of the function $H(T)$, it is convenient to distinguish between two cases: the non-isothermal (or mushy) phase-change, and the isothermal phase-change.
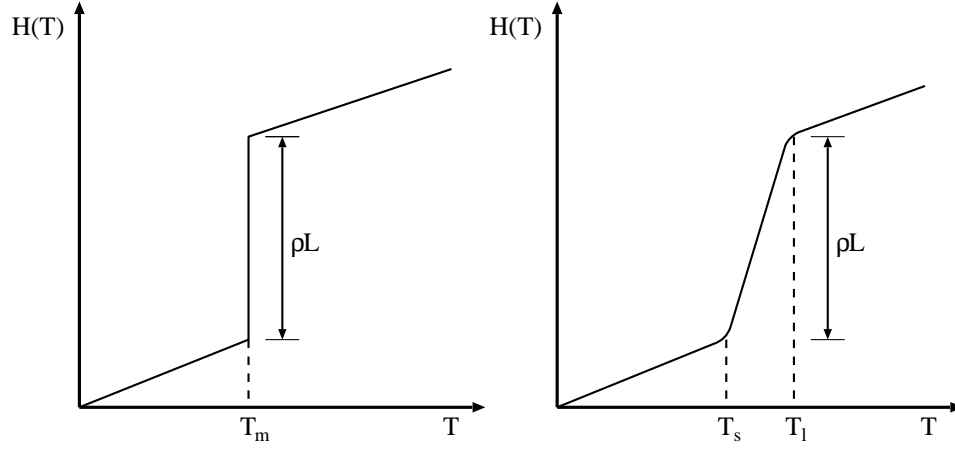
Figure 5.1: *Sketches of the enthalpy versus temperature relations for isothermal phase-change (left) and mushy phase-change.*

In case of isothermal phase-change, the enthalpy function has a jump-discontinuity at the melting temperature T_m and its temperature dependence may be written as

$$H(T) = \begin{cases} \int_{T_{\text{ref}}}^{T} \rho c_s(T) dT, & \text{for } T \leq T_m, \\ \int_{T_{\text{ref}}}^{T_m} \rho c_s(T) dT + \rho L + \int_{T_m}^{T} \rho c_l(T) dT, & \text{for } T > T_m. \end{cases} \tag{5.18}$$

The quantity ρL, where L is the latent heat, is the energy that is required for a phase transition from the solid to the liquid state. If for example we consider the case in which c_s, c_l are constants and $T_{\text{ref}} = T_m$ then (5.18) becomes:

$$H = \begin{cases} \rho c_s(T - T_m), & T \leq T_m, \\ \rho c_l(T - T_m) + \rho L, & T > T_m. \end{cases} \tag{5.19}$$

That is, solving for T, it follows that

$$T = \begin{cases} T_m + \frac{H}{\rho c_s}, & \text{for } H \leq 0, \quad \text{(solid)} \\ T_m, & \text{for } 0 < H \leq \rho L, \quad \text{(phase change)} \\ T_m + \frac{H - \rho L}{\rho c_l}, & \text{for } H > \rho L. \quad \text{(liquid)} \end{cases} \tag{5.20}$$

A more general form of phase-change, often appearing in industrial applications involving alloys, is that of mushy phase-change. In these problems melting takes place over a finite interval $[T_s, T_l]$. For non-isothermal

cases the enthalpy function (5.17) takes the form:

$$
H(T) = \begin{cases}
\int_{T_{\mathrm{ref}}}^{T} \rho c_s(T)dT, & \text{for } T \leq T_s, \\[2ex]
\int_{T_{\mathrm{ref}}}^{T_s} \rho c_s(T)dT + \int_{T_s}^{T} \rho \frac{\partial L}{\partial T} dT, & \text{for } T_s < T \leq T_l, \\[2ex]
\int_{T_{\mathrm{ref}}}^{T_s} \rho c_s(T)dT + \rho L + \int_{T_l}^{T} \rho c_l(T)dT, & \text{for } T > T_l.
\end{cases} \tag{5.21}
$$

In Figure 5.1 the enthalpy versus temperature relations in case of isothermal and mushy phase-change have been sketched.

The enthalpy formulation removes the necessity of carefully tracking the moving interface and consequently standard numerical techniques can be employed. Since in the enthalpy method the moving interface is not explicitly tracked, but the front position may be recovered from the values of the enthalpy a posteriori, the method may be characterized as a front-capturing scheme.

5.3.1 Enthalpy methods

It should be noted that the abrupt change in H as described by (5.18) gives rise to numerical difficulties. For instance, a naive discretization of the enthalpy equation on a uniform grid is well known to predict non-physical features such as step-like movement of the phase boundary and spurious temperature plateaux [17]. However, temperature plateaux can be physical in problems that are governed by an external source, see Figure 5.2.

The step-like behavior that appears in the time history of the temperature in a typical point is a consequence of the temperature being 'enforced' to be equal to the melting temperature during the phase transition. This 'stair-casing' can be smoothed by reducing the spatial step size, by introducing a special algorithm in the neighborhood of the phase-change to effectively 'track' the moving interface, by spreading the phase-change over a temperature range, by employing approximation techniques, or by combinations of these methods, see Dalhuijsen and Segal [19] and References therein.

The solution to the nonlinear system of equations, obtained by discretization of the enthalpy problem, can be found using Picard iterations, Newton-Raphson or the nonlinear successive over-relaxation method of Elliott and Ockendon [23], which uses relaxation only when there is no phase-change. In particular in case of the Newton-Raphson method, the determination of the derivative of $u = T(H)$ in the Jacobian of the system gives rise to conceptual problems as to the meaning and existence of this derivative, since the derivative experiences jumps at $H = 0$ and $H = \rho L$ [2], Chapter 4.3.

To avoid numerical difficulties associated with the instantaneous jump in the enthalpy, Bhattacharya et al. [5] propose the use of an artificial phase-

(a) stair-casing   (b) plateaux
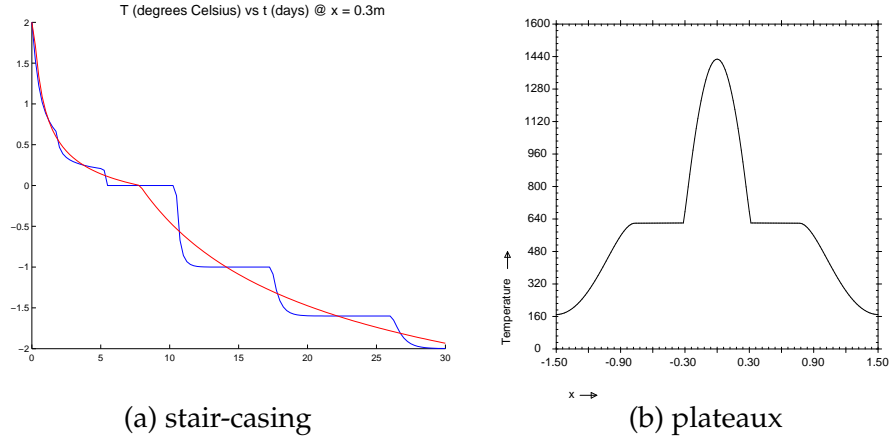
Figure 5.2: *Inherent to enthalpy methods are (a) the step-like behavior ('stair-casing') in the temperature as function of time and (b) the appearance of plateaux (regions where the temperature is (almost) constant in several adjacent nodes).*

change region around the discontinuity at the melting point. The governing equation that they consider is a source free energy balance equation:

$$\frac{\partial H}{\partial t} = \frac{\partial}{\partial x}\left(\kappa_{\text{eff}}\frac{\partial T}{\partial x}\right), \tag{5.22}$$

where $\kappa_{\text{eff}} = \phi_l \kappa_l + (1 - \phi_l)\kappa_s$ is the effective thermal conductivity and ϕ_l is the liquid volume fraction, which depends on the equilibrium phase diagram of the specific material involved, and is a function of temperature at a given position in the sample. Since ϕ_l is a step function in case of isothermal phase-change, an artificial phase-change range of ΔT around T_m is assumed, within which ϕ_l is assumed to vary linearly from 0 to 1. The following functional form for ϕ_l is used:

$$\phi_l = \begin{cases} 0, & T \leq T_I, \\[2mm] \frac{T-T_I}{T_F-T_I}, & T_I \leq T \leq T_F, \\[2mm] 1, & T \geq T_F. \end{cases} \tag{5.23}$$

Here $T_I = T_m - \Delta T/2$ is the initial melting point and $T_F = T_m + \Delta T/2$ is the final melting point. The enthalpy function of the system is written as

$$H(T) = \rho(1 - \phi_l)\int_{T_{\text{ref}}}^{T} c_s d\tau + \rho\phi_l\left(\int_{T_{\text{ref}}}^{T_I} c_s d\tau + L + \int_{T_I}^{T} c_l d\tau\right). \tag{5.24}$$

Although this regularization causes the convergence behavior of the iterative solver to improve, the stair-casing effect is not reduced. It merely
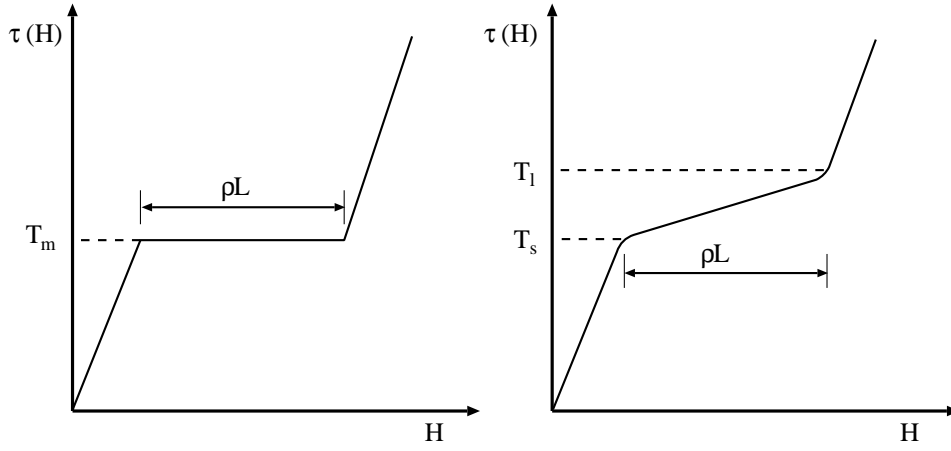
Figure 5.3: *Sketches of the temperature versus enthalpy relations for isothermal phase-change (left) and mushy phase-change.*

introduces sloped steps, with the angle of the slopes related to the value of ΔT.

Of course, as already stated by Shamsundar [62], smoothing of the enthalpy function on a stationary grid has to be done carefully, since the numerical results tend to become inaccurate when the amount of smoothing is too large. The accuracy can be improved by reducing the amount of smoothing, but this will eventually cause the step-like movement of the moving interface to reappear.

Nedjar [49] remarks that when regularization is used, a possible deviation from the original problem may occur. Instead, Nedjar proposes an incrementation of the enthalpy field as follows:

$$\Delta H^i = \frac{1}{\tau'(H^i)} \left[\Delta T^i + \left(T^i - \tau(H^i) \right) \right], \tag{5.25}$$

where $\Delta H^i := H^{i+1} - H^i$, $\Delta T^i := T^{i+1} - T^i$, and τ' is the derivative of the reciprocal function $\tau : \mathbb{R} \to \mathbb{R}$, given by $T = \tau(H)$. Expression (5.25) directly follows from the linearization of the function $\tau(H)$, given by

$$T^{i+1} := T^i + \Delta T^i = \tau(H^i) + \tau'(H^i)\Delta H^i. \tag{5.26}$$

Due to the non-convexity of the function $\tau(H)$, see Figure 5.3, the incrementation (5.25) is relaxed by replacing the fraction $1/\tau'(H^i)$ by a constant quantity μ in all of the domain and during the whole iterative process as

$$\Delta H^i = \mu \left[\Delta T^i + \left(T^i - \tau(H^i) \right) \right]. \tag{5.27}$$

The relaxation parameter μ must satisfy the condition

$$\mu \leq \frac{1}{\max \tau'(H^i)}. \tag{5.28}$$

In general, $\mu = 1/\max \tau'(H^i)$ proves to be a convenient choice. A major benefit of this approach is that it is very robust. In particular, the method requires no modifications in order to deal with plateaux that appear as a result of the addition of a source. However, convergence of the iterative solver can be very slow, owing to the relaxation factor as chosen in (5.28), especially for larger values of the latent heat, and wiggles are observed in the isotherms near the moving front.

A different approach, which yields no oscillations of the temperature and phase front, is proposed by Chun and Park [16]. They present an enthalpy related fixed-grid method which is implicit in time. To deal with the nodal points across the solid-liquid interface a fictitious temperature concept is introduced. Assuming that the density across the phases is constant, the governing equations considered are:

$$\frac{\partial h}{\partial t} = \kappa \nabla^2 h, \tag{5.29}$$

$$L v_n = \kappa_s \left. \frac{\partial h}{\partial n} \right|_s - \kappa_l \left. \frac{\partial h}{\partial n} \right|_l. \tag{5.30}$$

Here, h is the sensible enthalpy, i.e., latent heat is not included in the enthalpy, n is the surface normal and v_n is the velocity of the phase front. Without loss of generality, the enthalpy at the melting temperature, h_m, is set to zero. Using fictitious enthalpies positioned at a grid distance Δx of the location of the phase front X, the following numerical discretization is derived:

$$\frac{h_i^{n+1} - h_i^n}{\Delta t} = \frac{\phi_{i+1}^{n+1} - 2\phi_i^{n+1} + \phi_{i-1}^{n+1}}{(\Delta x)^2} + S_i, \tag{5.31}$$

where

$$S_i = \frac{\xi L}{\Delta x} \frac{X^{n+1} - X^n}{\Delta t}, \quad \text{for } |X^{n+1} - x_i| < \Delta x, \tag{5.32}$$

$$S_i = 0, \quad \text{for } |X^{n+1} - x_i| \geq \Delta x, \tag{5.33}$$

$$\xi = 1 - \frac{|X^{n+1} - x_i|}{\Delta x}, \tag{5.34}$$

$$\phi_i = \begin{cases} \kappa_l h_i, & \text{for } h_i \geq h_m, \\[2mm] \kappa_s h_i, & \text{for } h_i < h_m, \end{cases} \tag{5.35}$$

and x_i are the nodal points. The new position of the phase boundary is

obtained from

$$L\frac{X^{n+1} - X^n}{\Delta t} = \kappa_s \frac{h_m - \left[(1-\delta)h_{i-1}^{n+1} + L_i^{n+1}\right]}{\Delta x} - \kappa_l \frac{\left[(1-\delta)h_{i+1}^{n+1} + L_{i+2}^{n+1}\right] - h_m}{\Delta x},$$
(5.36)

where $0 \le \delta = |X^{n+1} - x_i| \le 1$. Per time step, an iterative process is performed in which first the position of the boundary is updated using (5.36) and then Equation (5.31) is solved until the phase boundary coordinate and enthalpy values are converged (for some convergence criteria). The solution is free of oscillations, i.e., shows no staircasing, since the phase boundary is treated as a line rather than a control volume. Although, according to Chun and Park, the method can be extended to two dimensional problems without much difficulty, it appears that an extension to 3D is rather non-trivial. Unfortunately, it seems that this technique cannot be easily applied to unstructured grids and finite elements.

Several methods have been developed for (adaptive) moving meshes. In order to incorporate the movement of the grid, a semi-Lagrangian formulation is considered of the form:

$$\frac{\partial H}{\partial t} - \frac{dx}{dt}\frac{\partial H}{\partial x} = \frac{\partial^2 u}{\partial x^2} + Q,$$
(5.37)

where the Kirchhoff transformed temperature defined as

$$u = \int_{T_{\text{ref}}}^{T} \kappa(\zeta)d\zeta,$$
(5.38)

is used in order to allow for a temperature dependency of the thermal conductivity κ. For instance, Mackenzie and Robertson [40] employ a technique based on integrable monitor functions to generate appropriate grid point distributions as well as smoothing of the enthalpy function in order to obtain accurate results for the one-dimensional problems that they considered.

Besides that the moving grid methods in general are rather elaborate, further disadvantages are the mesh generation for complex geometries, difficulties when there are nonlinearities and postprocessing. Moreover, these difficulties increase with the dimension of the problem [14].

5.4 Level set approach

In the enthalpy methods discussed in the previous section, the introduction of an enthalpy function that accounts for the latent heat absorption makes that the Stefan condition (3.2b):

$$v_n = \frac{1}{\rho L}\left[\kappa\frac{\partial T}{\partial \mathbf{n}}\right],$$
(5.39)

on the moving interface does not have to be enforced explicitly and therefore the front is only tracked implicitly. As we have seen, the enthalpy approach can be applied to both phase-change problems involving sharp fronts as well as problems with melting trajectories or mushy zones. For Stefan problems involving sharp moving interfaces, level set methods can be employed. Level set theory has been extensively developed, especially for finite difference methods, see References [51, 61, 64], although some finite element based studies have been published by for instance Barth and Sethian [3].

5.4.1 General principle

In the level set approach, the interface is represented by a signed distance function. This function $\Phi(\mathbf{x}, t)$, appropriately called the level set function, is defined as

$$\Phi(\mathbf{x}, t) = \begin{cases} + \min_{\bar{\mathbf{x}} \in \Gamma(t)} \|\mathbf{x} - \bar{\mathbf{x}}\|, & \mathbf{x} \in \Omega_l, \\ 0, & \mathbf{x} \in \Gamma, \\ - \min_{\bar{\mathbf{x}} \in \Gamma(t)} \|\mathbf{x} - \bar{\mathbf{x}}\|, & \mathbf{x} \in \Omega_s. \end{cases} \tag{5.40}$$

The location of the moving boundary Γ is then equal to the zero level set of Φ, i.e.:

$$\Gamma(t) = \{\mathbf{x} \in \Omega : \Phi(\mathbf{x}, t) = 0\}. \tag{5.41}$$

The main idea of the level set method is to move Φ with the correct speed v_n, prescribed by the Stefan condition (5.39), at the front and then to update the temperature, $T(\mathbf{x}, t)$, with the new position of the front stored implicitly in Φ. When the new position of the front is known, updating the temperature comes down to solving the heat equation over the whole domain Ω, where special care has to be taken near the interface between the phases. We will return to this matter later.

The interface motion is governed by the conservation equation

$$\Phi_t + F|\nabla\Phi| = 0, \tag{5.42}$$

where F is a speed function that is a continuous extension of v_n off Γ onto all of Ω. The construction of F seems to be one of the most difficult aspects of the level set method, mostly since F highly depends on the phase-change problem considered, in particular the front velocity v_n and the number of spatial dimensions. A commonly used technique to obtain the extended velocity field, is the fast marching method, which has been introduced by Sethian [59] in the context of the level set method in 1996, and later improved in References [15, 60].

The level set function Φ can also be used to define the outward pointing normal $\mathbf{n}$ by

$$\mathbf{n} = \nabla\Phi/|\nabla\Phi|, \tag{5.43}$$

and the interface curvature K by

$$K = \nabla \cdot \mathbf{n} = \nabla \cdot \left(\frac{\nabla\Phi}{|\nabla\Phi|}\right). \tag{5.44}$$

An illustrative article on the application of a level set technique using finite differences for solving Stefan problems, is that of Chen et al. [13]. In order to capture the moving front on a fixed grid the method as described by the authors can be outlined as follows:

1. Initialize T and Φ, so that Φ is the signed distance from the interface.

2. Compute the extended velocity field F.

3. Update Φ using equation (5.42) for one time step. The new position of the interface is then equal to the zero level set of Φ. Since the level set function will cease to be an exact distance function, even after this one time step, a re-initialization of Φ is used to retain a distance function.

4. Away from the interface Γ, solve the heat diffusion equation for T. For grid points less than or equal to a step size away from the front, appropriate numerical techniques are employed to approximate T.

5. Repeat steps 2 to 4 to get the next updated values of Φ and T.

The numerical solving of the heat equation as mentioned in step 4 is not restricted to a centered finite difference scheme, as proposed in the article, but can be any suitable discretization scheme. For details on the discretization of the velocity extension, discretization of the updating of the level set function, etc. the reader is referred to Reference [13].

If a variational approach is considered, the standard fixed grid based Galerkin approximations often exhibit poor representations of arbitrary discontinuities, such as cracks or phase fronts. Therefore, most standard finite element approaches require the employment of (adaptive) moving meshes and significant mesh refinements in order to resolve difficulties concerning these discontinuities and to properly deal with for instance moving heat sources.

The extended finite-element method (X-FEM) takes an alternative approach by extending the classical finite-element method (see for example Chessa et al. [14], Merle and Dolbow [47], Ji et al. [36]). To accurately capture arbitrary jumps in the gradient of the temperature, the key element of the

X-FEM is the addition of the so-called enrichment function, say, $g(\mathbf{x})$, to the Galerkin approximation of the temperature:

$$T(\mathbf{x}, t) = \sum_{i \in I} \phi_i(\mathbf{x}) T_i(t) + \sum_{j \in J} b_j \phi_j(\mathbf{x}) g(\mathbf{x}). \tag{5.45}$$

Here, the ϕ_k are the standard basis functions, I is the set of all nodes in the mesh, J is a subset of I that consists of all the nodes that are the vertices of the elements that are intersected by the moving front, and b_j are additional unknowns. In practice, this means that for instance for triangular elements with three nodes, the enriched elements have six degrees of freedom, while the others have only three. But, although the location of the discontinuity can be updated without a significant computational expense, the XFEM does not remove the complications associated with the extension of the velocity field.

5.5   Temperature approach

In Section 5.3 the *enthalpy* formulation has been discussed. Under the assumption of constant physical parameters, the enthalpy $H(T)$ for an isothermal problem has been defined as (5.19):

$$H(T) = \begin{cases} \rho c_s (T - T_m), & T \leq T_m, \\[2mm] \rho c_l (T - T_m) + \rho L, & T > T_m. \end{cases} \tag{5.46}$$

In the enthalpy formulation the enthalpy H is treated as a second dependent variable besides the temperature T. Using relation (5.46), the heat diffusion equation (3.2a) and the Stefan condition (3.2b) are replaced by the well-known enthalpy equation:

$$\frac{\partial H(T)}{\partial t} - \kappa_{s,l} \Delta T = q. \tag{5.47}$$

In the temperature formulation, instead of separating the domain in a liquid and solid part, as via definition (5.46), the enthalpy is written according to its formal definition: as the sum of sensible and latent heat:

$$H(T) = H^{\text{sensible}} + H^{\text{latent}} = \rho c_{s,l}(T - T_m) + \rho L f_l(T), \tag{5.48}$$

where $f_l(T)$ denotes the liquid volume fraction, which in case of isothermal phase-change is equal to the Heavyside step function $\mathcal{H}(T - T_m)$. Definition (5.48) leads to the classical Fourier heat diffusion equation, but with an additional term for the latent heat contribution:

$$\rho c_{s,l} \frac{\partial T}{\partial t} + \rho L \frac{\partial f_l}{\partial t} - \kappa_{s,l} \Delta T = q. \tag{5.49}$$

Here, the time derivative of the liquid volume fraction is to be interpreted in the weak sense. A benefit of this formulation is that the temperature becomes the primal (and only) dependent variable.

The addition of the term related to the latent heat makes that the temperature formulation (5.49) is highly nonlinear. Fachinotti et al. [24] consider a finite element discretization of Equation (5.49) for which they propose an analytical discontinuous integration technique. That is, for those elements that are intersected by the moving phase front, the integrals over the elements are obtained by adding up the analytically evaluated contributions over each of the two (liquid or solid) subdomains. Because the integrals are concisely expressed in their exact analytical form and no explicit regularization of the enthalpy function is carried out, the energy balance in weak form is exactly satisfied in discrete sense.

The nonlinear system of equations is solved using a Newton-Raphson iterative procedure. To improve global convergence, in particular in case of larger values of the latent heat, a line search algorithm is implemented. The (eventual) quadratic convergence rate makes that the temperature approach can be very cost efficient.

5.6 Evaluation of the methods

In Chapter 3, a mathematical model for the melting component of the formation of a mark was proposed. In the preceding sections many numerical techniques for solving general two-phase Stefan problems have been discussed. Unfortunately, most of these techniques cannot be employed to fulfill our goal of solving the moving boundary problem (3.2a) - (3.2c) inside the domain Ω. As a guideline, a selection of minimal requirements is considered. First and foremost, the method should be able to handle 'realistic' three-dimensional complex composite geometries, and should therefore also be robust. Furthermore, the method should be capable of dealing with multiple separate fronts. Besides, the method has to allow for the merging and breaking of these fronts. And although in the current melting model the assumption is made that only isothermal phase-change materials are considered, see Chapter 3, it can be beneficial for future work, if the method can be adapted to mushy problems. Last, but not least, the method is preferably simple (implementation/comprehension) and efficient (memory/computational time).

In the enthalpy approach the position of the moving boundary is implicitly incorporated in the enthalpy equation, and therefore no active tracking of the location of the front is required. Because the discretized system is highly nonlinear, linearizations or advanced solvers for nonlinear systems have to be employed. The location of the boundary is determined as part of a postprocessing step for which various techniques have been proposed with which fairly accurate results can be obtained. In general, the enthalpy

methods perform best in case of non-isothermal problems. In case of isothermal problems a smoothing of the enthalpy equation is advisable in order to minimize oscillations. Due to the implicit description of the moving front, multiple fronts, kinks and the merging/separation of fronts can probably be dealt with without much difficulty. Of particular interest are the nonlinear SOR algorithm of Elliott-Ockendon, because of its simplicity and relatively fast convergence, and the concept of a relaxed linearization by Nedjar, because the principle is independent of the spatial dimension and is applicable to both isothermal and mushy phase-change problems.

The explicit tracking of the moving front, such as with the level set method, is in particular interesting for problems in which the interface between phases is sharp. The location of the interface is accurately described by the zero level set of the level set function. Although the method essentially seems to be fairly simple and robust, there is one major disadvantage with respect to the level set function. In particular for phase-change problems, the construction of an (arbitrary) extension of the velocity field to the whole domain can be complicated, since only the velocity on the boundary itself is known. The inclusion of the level set function as part of enhancement functions in XFEM, or hybrid techniques in which advection of the level set function is performed using finite differences, do not tackle this inherent difficulty.

Since the temperature formulation (5.49) can be interpreted as a classical heat diffusion equation, but with an additional nonlinear source term, one of the major benefits of this approach is that it allows for the inclusion of melting into an existing (finite element) code. The method can be applied to virtually any form of phase transition, as described by the liquid volume fraction function $f_l(T)$, and in combination with a line search procedure, very fast convergence can be obtained. This makes that the method is both robust and efficient. However, the implementation of the discontinuous integration concept can be rather challenging in 3D.

5.7   Conclusions

A wide selection of numerical methods for solving two-phase Stefan problems is given in the literature. However, only a few methods can potentially be adopted to numerically determine a solution to the Stefan problem, as formulated in Chapter 3. Out of all methods discussed, the nonlinear SOR scheme of Elliott-Ockendon, the relaxed linearized enthalpy approach by Nedjar and the temperature approach using discontinuous integration by Fachinotti et al. are considered to be the most suitable methods. These methods are therefore discussed in more detail in Chapters 6 and 7. Of particular interest will be whether the basic ideas behind each method can be extended to be applicable to complex three-dimensional composite domains.

CHAPTER 6

The enthalpy approach

Enthalpy methods are commonly used to solve a wide selection of moving boundary problems. The focus of this chapter will be on two numerical methods that use the enthalpy approach, described in Section 5.3. An SOR scheme, modified for nonlinear systems, is discussed in Section 6.2 and a pseudo-Newton scheme is derived in Section 6.3. The main interest, of course, will be whether either method can be adopted to solve our Stefan problem (3.2a - 3.2c).

6.1 The Kirchhoff transformation

A well known transformation in the literature on enthalpy problems is the Kirchhoff transformation. The main reason for applying this transformation is that it eliminates the nonlinearity in the diffusion term. As such, in particular when an implicit scheme is used, a gain in efficiency can be obtained, due to faster convergence of the employed iterative scheme. Alexiades and Solomon [2], Chapter 4.3, even emphasize that, specifically when the thermal conductivities κ of the phases are unequal, and when they are functions of the temperature only and not of position, the Kirchhoff method should be used.

The normalized Kirchhoff transformed temperature is defined as

$$\tilde{T} := \int_{T_m}^{T} \kappa(\tau)d\tau = \begin{cases} \int_{T_m}^{T} \kappa_s(\tau)d\tau, & T < T_m, \\ \int_{T_m}^{T} \kappa_l(\tau)d\tau, & T \geq T_m. \end{cases} \tag{6.1}$$

For constant κ_s, κ_l, we have:

$$\tilde{T} = \begin{cases} \kappa_s(T - T_m), & T < T_m \\ 0, & T = T_m \\ \kappa_l(T - T_m), & T > T_m \end{cases} \tag{6.2}$$

The corresponding enthalpy is:

$$\tilde{H} = \begin{cases} \frac{\rho c_s \tilde{T}}{\kappa_s}, & \tilde{T} \le 0, \\ \frac{\rho c_l \tilde{T}}{\kappa_l} + \rho L, & \tilde{T} > 0. \end{cases} \tag{6.3}$$

6.2 Nonlinear SOR

Application of the standard Galerkin FEM to the enthalpy equation (5.47), in combination with one or more of the boundary conditions (3.4)-(3.6), leads to an equivalent system of (nonlinear) equations. In matrix-vector notation this system is given by:

$$M\frac{\partial \tilde{\mathbf{H}}}{\partial t} + S\tilde{\mathbf{T}} = \mathbf{q}, \tag{6.4}$$

where M is the mass matrix and S is the stiffness matrix.

In case Euler backward is applied for the time integration, with a time step size Δt, the fully discretized system at time level $m + 1$ is given by

$$M\frac{\tilde{\mathbf{H}}^{m+1} - \tilde{\mathbf{H}}^m}{\Delta t} + S\tilde{\mathbf{T}}^{m+1} = \mathbf{q}^{m+1}. \tag{6.5}$$

Remark that, for simplicity, the time-dependence of the stiffness matrix, which is not constant because the position of the moving interface determines the value of the thermal conductivity κ for each node at each time level, has been omitted. The mass matrix is always constant, since the specific heat c is contained in the enthalpy.

If we let $\bar{M}$ be the lumped version of the mass matrix M, D the diagonal of the stiffness matrix S, and $\bar{S}$ a matrix containing the off-diagonals of S, (6.5) can be rewritten as

$$\tilde{\mathbf{H}}^{m+1} + \Delta t \bar{M}^{-1} D\tilde{\mathbf{T}}^{m+1} = \Delta t \bar{M}^{-1}\mathbf{q}^{m+1} - \Delta t \bar{M}^{-1}\bar{S}\tilde{\mathbf{T}}^{m+1} + \tilde{\mathbf{H}}^m, \tag{6.6}$$

or

$$\tilde{\mathbf{H}}^{m+1} + Z\tilde{\mathbf{T}}^{m+1} = \mathbf{z}, \tag{6.7}$$

where

$$Z = \Delta t \bar{M}^{-1} D, \tag{6.8}$$

$$\mathbf{z} = \Delta t \bar{M}^{-1}\mathbf{q}^{m+1} - \Delta t \bar{M}^{-1}\bar{S}\tilde{\mathbf{T}}^{m+1} + \tilde{\mathbf{H}}^m. \tag{6.9}$$

By denoting the iteration number with the superscript (p) this system of equations can be reduced to (Gauss-Seidel):

$$\tilde{H}_j^{(p+1)} + Z_j \tilde{T}_j^{(p+1)} = z_j^{(p)}, \quad j = 1, \ldots, n \tag{6.10}$$

The Elliott-Ockendon SOR iteration process is then given by, see Reference [11]:

1. Compute Z_j and $z_j^{(p)}$.

2. Compute $\tilde{T}_j^{(p+1)}$ from (6.10), using definition (6.3) for the enthalpy:

$$\tilde{T}_j^{(p+1)} = \begin{cases} \frac{z_j^{(p)}}{\rho c_s + Z_j}, & z_j^{(p)} \leq 0, \\ 0, & 0 < z_j^{(p)} < \rho L, \\ \frac{z_j^{(p)} - \rho L}{\rho c_l + Z_j}, & z_j^{(p)} \geq \rho L. \end{cases} \tag{6.11}$$

3. Set $\hat{T}_j^{(p+1)} = \tilde{T}_j^{(p)} + \omega \left[\tilde{T}_j^{(p+1)} - \tilde{T}_j^{(p)} \right]$ (Over-relaxation).

4. Set

$$\tilde{T}_j^{(p+1)} = \begin{cases} \hat{T}_j^{(p+1)}, & \text{if } \hat{T}_j^{(p+1)} \cdot \tilde{T}_j^{(p)} > 0, \\ \tilde{T}_j^{(p+1)}, & \text{if } \tilde{T}_j^{(p+1)} \cdot \tilde{T}_j^{(p)} \leq 0, \end{cases} \tag{6.12}$$

   that is, only over-relax the nodes that have not just changed phase.

5. If a convergence criterion, say $\left\| \tilde{T}_j^{(p+1)} - \tilde{T}_j^{(p)} \right\| <$ *tolerance*, is satisfied, then set $\tilde{T}_j^{m+1} = \tilde{T}_j^{(p+1)}$ and $\tilde{H}_j^{m+1} = z_j^{(p)} - Z_j \cdot \tilde{T}_j^{m+1}$.

6.2.1 Evaluation of the method

With respect to applying the above technique to obtain the temperature distribution in a multilayered geometry, the following theoretical and practical difficulties arise:

1. In Alexiades and Solomon [2], Chapter 4.3, it is illustrated how in case of a 1D slab consisting of 2 layers, the enthalpy method can be applied. The key idea is to consider the interface between the two layers as an 'interface' that moves at zero speed. The enthalpy function is now not only dependent on the temperature, but also on position. For the given 1D example, the Ockendon-Elliott SOR method can quite easily be implemented. However, in case of 2D or 3D, it becomes increasingly more difficult (non-smooth edges, corners etc..).

2. The Ockendon-Elliott algorithm is nodal-point based. Especially in case of finite elements, when in particular the enthalpy might be multi-valued in nodal points along the (free) boundaries, it is not clear whether the method might break down or not.

3. The physical parameters and the source term are required in the solver. In a general finite element package implementation, such as for instance SEPRAN [58], this is quite impractical.

4. There is no solid theoretical basis on how to choose the relaxation parameter ω.

6.3   Pseudo-Newton method

In Reference [49] it is described how the fully discretized system (6.5) can be solved using a pseudo-Newton iterative procedure in terms of a temperature increment $\Delta\tilde{\mathbf{T}}_i$. Before we explain how this technique can be adapted to solve for the temperature distribution in a multilayered domain, we will first briefly repeat the three steps that form the key idea behind the proposed integration algorithm by Nedjar [49]. We conclude this section with an evaluation of the presented method with respect to the melting model.

6.3.1   Method description

First, introduce the reciprocal function $\tau : \mathbb{R} \longrightarrow \mathbb{R}$ of (5.46), given by $\tilde{\mathbf{T}} = \tau(\tilde{\mathbf{H}})$ and define

$$\tilde{\mathbf{H}}_{i+1} = \tilde{\mathbf{H}}_i + \Delta\tilde{\mathbf{H}}_i, \tag{6.13}$$

$$\tilde{\mathbf{T}}_{i+1} = \tilde{\mathbf{T}}_i + \Delta\tilde{\mathbf{T}}_i. \tag{6.14}$$

Next, consider a linearization of the function $\tau(\tilde{\mathbf{H}})$:

$$\tilde{\mathbf{T}}_{i+1} = \tilde{\mathbf{T}}_i + \Delta\tilde{\mathbf{T}}_i = \tau(\tilde{\mathbf{H}}_i) + \tau'(\tilde{\mathbf{H}}_i)\Delta\tilde{\mathbf{H}}_i, \tag{6.15}$$

or, rewritten in terms of the enthalpy update $\Delta\tilde{\mathbf{H}}_i$:

$$\Delta\tilde{\mathbf{H}}_i = \frac{1}{\tau'(\tilde{\mathbf{H}}_i)} \left[\Delta\tilde{\mathbf{T}}_i + \left(\tilde{\mathbf{T}}_i - \tau(\tilde{\mathbf{H}}_i) \right) \right]. \tag{6.16}$$

Here, τ' denotes the derivative of τ with respect to its argument. Unfortunately, this derivative can be zero. This is resolved by approximating the fraction in equation (6.16) by a constant μ defined as

$$\mu = \frac{1}{\max(\tau'(\tilde{\mathbf{H}}_i))}, \tag{6.17}$$

such that the relaxed enthalpy update becomes

$$\Delta\tilde{\mathbf{H}}_i = \mu\left[\Delta\tilde{\mathbf{T}}_i + \left(\tilde{\mathbf{T}}_i - \tau(\tilde{\mathbf{H}}_i)\right)\right]. \tag{6.18}$$

If we now define

$$\hat{\mathbf{q}} = \mathbf{q}^{m+1} + \hat{M}\tilde{\mathbf{H}}^m, \qquad \hat{M} = \frac{1}{\Delta t}M, \tag{6.19}$$

then substitution of (6.13)-(6.15) and (6.18) into the discretized system (6.5) gives

$$\hat{M}\left\{\tilde{\mathbf{H}}_i + \mu\left[\Delta\tilde{\mathbf{T}}_i + \left(\tilde{\mathbf{T}}_i - \tau(\tilde{\mathbf{H}}_i)\right)\right]\right\} + S(\tilde{\mathbf{T}}_i + \Delta\tilde{\mathbf{T}}_i) = \hat{\mathbf{q}}. \tag{6.20}$$

A rearrangement of terms finally leads to

$$\left(\mu\hat{M} + S\right)\Delta\tilde{\mathbf{T}}_i = \hat{\mathbf{q}} - \left(\mu\hat{M} + S\right)\tilde{\mathbf{T}}_i - \hat{M}\left(\tilde{\mathbf{H}}_i - \mu\tau(\tilde{\mathbf{H}}_i)\right). \tag{6.21}$$

By rewriting the discretized heat diffusion equation in terms of the temperature increment $\Delta\tilde{\mathbf{T}}_i$ for those layers of a recording stack that do not contain a phase change material, it is possible to build a system of equations for the multilayer as a whole. This means, that any existing finite element code for heat diffusion problems in composite domains, can easily be extended to include melting.

6.3.2   Evaluation of the method

At first glance, the Nedjar method appears to be an elegant solution method for our two-phase Stefan problem. The implicit treatment of the moving interface, which is inherent to the enthalpy approach, makes that the method can handle multiple separate fronts, and the merging and breaking up of these interfaces. The change of phase can be isothermal or mushy. And of course, we have a way of extending the method to problems on 3D multilayered domains.

However, some critical remarks can be made:

- A difficulty arises in case two adjacent layers of a multilayered configuration are active layers (i.e., the materials might melt): the enthalpy is then likely to be double-valued on the separating interface. Preferably, this is avoided. Therefore, in case of a multilayer, the assumption is made that the active layers are separated by at least one non-active layer (i.e., no melting occurs). This works, because in the non-active layers it suffices to solve the heat diffusion equation, since the temperature is the only dependent variable for these layers. Although this assumption seems very limiting when general stack configurations are considered, in practice it is not, since in existing recording stacks, two melting/recording layers are always separated by at least one non-melting layer.

- The evolution of the temperature in time, for a fixed point, shows 'stair-casing'. This undesirable effect has been addressed in an earlier report by Brusche [11]. The staircasing can be slightly reduced by increasing the number of elements. Of course, this might become very impractical, in particular for 3D problems.

- Strong wiggles in the position of the moving interface are observed, even on fine meshes and for small ϵ.

- The choice of the relaxation parameter μ as in (6.17) seems to be the most optimal choice, see Nedjar [49] and references therein. However, as a result of the relaxation, the observed convergence behavior is only linear, and often many iterations are required to reach convergence (with respect to the desired level of accuracy on the residual).

CHAPTER 7

The temperature approach

In the previous chapter we have looked at two enthalpy methods: an SOR scheme and a pseudo-Newton approach. Unfortunately, each method turns out to have its own major disadvantages with respect to our goal of finding a suitable method for solving the two-phase Stefan problem (3.2a - 3.2c) in 3D multi-layered domains. For the SOR scheme, an extension to composite domains seems to be nontrivial, or might not even be possible. The obstacles to application to coupled domains can be overcome by use of the pseudo-Newton approach, as proposed by Nedjar, but the number of iterations per time step turned out to become impractically large.

First, we will give a brief description of the temperature based method of Fachinotti et al. [24]. In particular we will focus on the concept of discontinuous integration, which is the key idea behind this temperature approach. The numerical evaluation of the integrals that arise from the FEM discretization of the temperature Equation (5.49) is discussed in Section 7.2.

As a result of the inclusion of latent heat, via the liquid volume fraction $f_l(T)$, Equation (5.49) is (highly) nonlinear. The corresponding discretized system is therefore solved using an iterative method. In order to improve the convergence behavior of the iterative solver, a line search or backtracking method is often needed. We will come back to this issue in Section 7.3.

In the concluding section a brief evaluation of the temperature method is presented.

7.1 Method description

In the temperature formulation, the diffusion of heat is described by equation (5.49):

$$\rho c_{s,l} \frac{\partial T}{\partial t} + \rho L \frac{\partial f_l}{\partial t} - \kappa_{s,l} \Delta T = q. \tag{7.1}$$
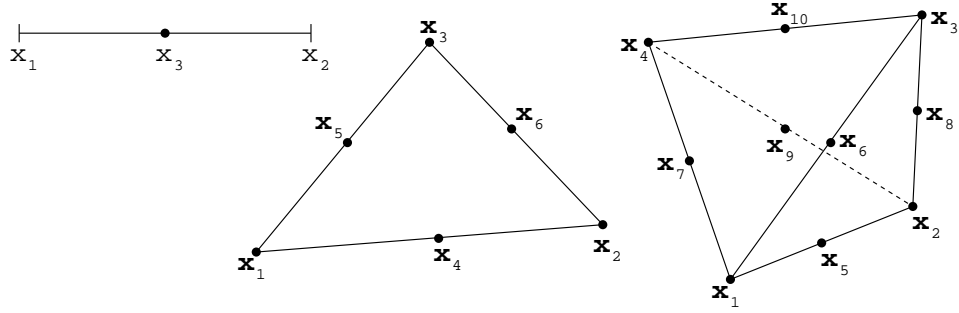
Figure 7.1: *First order C^0 elements in $\mathbb{R}^1$, $\mathbb{R}^2$ and $\mathbb{R}^3$.*

Application of the general Galerkin procedure, in which the temperature field is approximated by

$$T(\mathbf{x}, t) \approx \sum_{i=1}^{n} \phi_i(\mathbf{x}) T_i(t), \tag{7.2}$$

where ϕ_i is a (linear) basis shape function and T_i is the nodal temperature, in combination with an Euler backward time discretization, yields the following discretized system of (nonlinear) equations (at time level $m + 1$):

$$M^{m+1} \frac{T^{m+1} - T^m}{\Delta t} + \frac{L^{m+1} - L^m}{\Delta t} + S^{m+1} T^{m+1} = q^{m+1}. \tag{7.3}$$

Note that, when compared to the enthalpy approach, both the mass matrix as well as the stiffness matrix are now time-dependent (specific heat c is now included in the mass matrix; thermal conductivity κ is included in the stiffness matrix).

The matrix and vector entries for the above system are given by (boundary conditions have been omitted):

$$M_{ij} = \int_{\Omega} \rho c \phi_i \phi_j d\Omega, \tag{7.4}$$

$$S_{ij} = \int_{\Omega} \nabla \phi_i \cdot (\kappa \nabla \phi_j) d\Omega, \tag{7.5}$$

$$L_i = \rho L \int_{\Omega} \phi_i f_l d\Omega, \tag{7.6}$$

$$q_i = \int_{\Omega} \phi_i q d\Omega. \tag{7.7}$$

The distinct feature of the temperature based approach is the use of discontinuous integration in space. The key idea behind discontinuous integration, as for instance described by Fachinotti et al. [24], is that for elements intersected by the moving interface, the integrals (7.4 - 7.7) are not computed over an element as a whole at once, using for instance an averaged value for the physical parameters, but are instead computed over the liquid and solid subdomains separately. See Figure 7.2 for an illustration.

For problems without an external source term, an accurate evaluation of the discrete balance equation (7.3) is assured, because no regularization of the integrand is required [49]. However, depending on the shape and magnitude of the external source, difficulties with respect to the convergence of the iterative method will arise, if the considered problem is taken to be isothermal. In particular, in case the latent heat is relatively large, some elements will take on values that are (nearly) equal to the melting temperature, for several consecutive time steps. Often, the appearance of these so-called *plateaux* leads to a breakdown of the employed numerical method. A practical solution to this problem is the introduction of an artificial mushy region. In Section 9.3.2 the problem of dealing with a plateau will be discussed in more detail.

7.2   Numerical integration

Fachinotti et al. were not the first to apply discontinuous integration. But, as opposed to for instance Crivelli et al. [18], who applied a Gauss quadrature rule, Fachinotti et al. present an analytical integration technique. Fachinotti and coauthors prefer this analytical approach over the use of Gauss quadrature numerical integration, because "neither extra mapping is required nor summation over sample points."

However, despite of what is stated by Fachinotti et al., we believe that the use of Newton-Cotes numerical integration rules is a more practical choice, simply because only a (weighted) summation over sample points is required. Besides, the proposed analytical method by Fachinotti et al. requires several matrix-vector/matrix-matrix products and matrix inversions, which can be computationally costly.

The general form of an integration rule for the integration of an integrand $\text{Ind}(x)$ over an element e is given by:

$$\int_e \text{Ind}(x)dx = \sum_{k=1}^{r} w_k \text{Ind}(x_k), \tag{7.8}$$

in which r is the number of support points of the integration rule, the w_k are the weights (preferably $w_k > 0$), and x_k the support points.

For simplices, i.e., line segments in $\mathbb{R}^1$, triangles in $\mathbb{R}^2$ and tetrahedra in $\mathbb{R}^3$, see Figure 7.1, the Newton-Cotes formulas for the exact integration of a constant or linear function f over a simplex e, are as follows:

$$\int_e f \, dx =$$

$$\bullet \, \frac{|\Delta_1|}{2!} [\sum_{k=1}^{2} f(x_k)] \qquad\qquad (1D)$$

$$\bullet \, \frac{|\Delta_2|}{3!} [\sum_{k=1}^{3} f(\mathbf{x}_k)] \qquad\qquad (2D)$$

$$\bullet \, \frac{|\Delta_3|}{4!} [\sum_{k=1}^{4} f(\mathbf{x}_k)] \qquad\qquad (3D)$$

$$(7.9)$$

where $\Delta_1 = \det\begin{pmatrix} 1 & x_1 \\ 1 & x_2 \end{pmatrix}$,

$$\Delta_2 = \det\begin{pmatrix} 1 & x_1 & y_1 \\ 1 & x_2 & y_2 \\ 1 & x_3 & y_3 \end{pmatrix}, \text{and } \Delta_3 = \det\begin{pmatrix} 1 & x_1 & y_1 & z_1 \\ 1 & x_2 & y_2 & z_2 \\ 1 & x_3 & y_3 & z_3 \\ 1 & x_4 & y_4 & z_4 \end{pmatrix}. \qquad (7.10)$$

In case f is quadratic, e.g., the entries of the mass matrix, the Newton-Cotes formulas for exact integration are:

$$\int_e f \, dx =$$

$$\bullet \, \frac{|\Delta_1|}{3!} [f(x_1) + f(x_2) + 4f(x_3)] \qquad\qquad (1D)$$

$$\bullet \, \frac{|\Delta_2|}{3!} [\sum_{k=4}^{6} f(\mathbf{x}_k)] = \frac{|\Delta_2|}{3!} \sum f(\text{midpoints}) \qquad (2D)$$

$$\bullet \, \frac{|\Delta_3|}{5!} [-\sum_{k=1}^{4} f(\mathbf{x}_k) + 4\sum_{k=5}^{10} f(\mathbf{x}_k)] =$$

$$\frac{|\Delta_3|}{5!} \left[-\sum f(\text{vertices}) + 4\sum f(\text{midpoints}) \right] \qquad (3D)$$

$$(7.11)$$
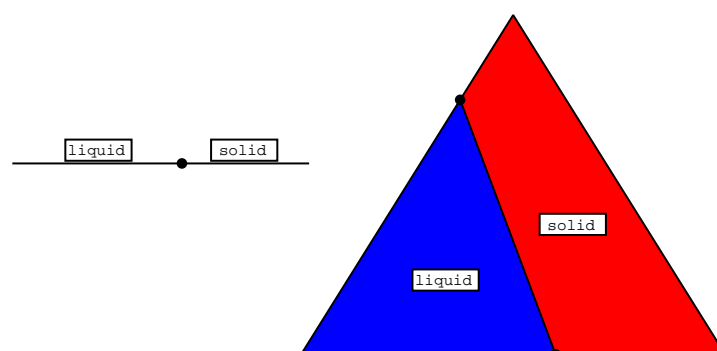
Figure 7.2: *For isothermal phase-change the intersection of simplices in 1D and 2D is almost trivial.*

In case of 1D isothermal phase-change, an element intersected by the moving interface is always subdivided into two line segments. Each segment is occupied by one of two phases of the material, see Figure 7.2. For each of these segments, the computation of the integrals (7.4)-(7.7) by means of a Newton-Cotes rule, is almost trivial. One should only take care to insert the correct values for the physical parameters.

As for 2D isothermal phase-change, a triangle can be intersected in three ways, all of which are topologically equivalent. For an intersection as depicted in Figure 7.2, the discontinuous integration of an integrand over the whole element is performed in two steps. First, the integral over the liquid subtriangle is computed, using the appropriate physical parameters for the liquid phase. Then, in order to evaluate the integral over the trapezium shaped solid region, we first compute the integral over the whole triangle, as if the element were not intersected, and thereafter subtract the integral part over the subtriangle. Alternatively, the trapezium shaped region can be further subdivided into subtriangles, and the integrals evaluated on each separate subtriangle.

In 3D we are faced with a bit more of a challenge. First of all, the area of the intersection of a tetrahedron can be either a triangle or a quadrilateral, see Figure 7.3. Furthermore, note that both of these intersections can occur in such a way that different 'corners' of the tetrahedron are 'cut off', each of which is topologically equivalent.

In order to compute the integrals over the liquid and the solid subdomains, it is of course convenient to do so in the most efficient way. In case the intersection area is a triangle, the tetrahedral domain is subdivided into a tetrahedron and a trapezoid. While an integral over the tetrahedral subdomain is easily computed using the Newton-Cotes integration rule, the evaluation of the integral over the remainder is somewhat more complicated. One choice would be to subdivide the remainder into three tetrahedra, compute the integral values over these tetrahedra and finally
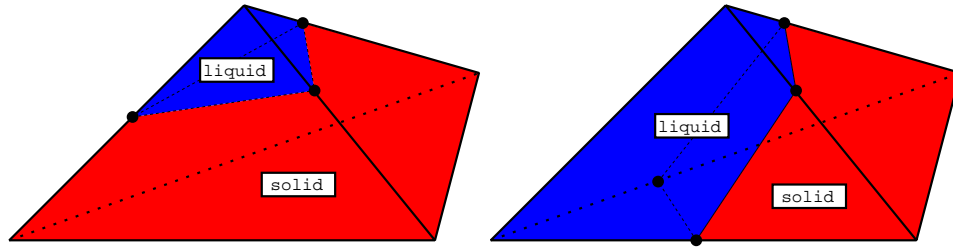
Figure 7.3: *In 3D, the intersection of a linear tetrahedron is either a triangle or a quadrilateral.*

add the contributions.

A more elegant approach is of course to first compute the integral over the whole tetrahedron, using the correct physical parameters corresponding to the phase of the remainder, and then to evaluate and subtract the integral part over the tetrahedral subdomain.

When the area of the intersection is a quadrilateral, one has no other choice than to subdivide each of the two trapezoidal subdomains into three tetrahedrals each and coherently adding the subsequent integral terms.

In general, the use of integration rules with negative weights should be avoided, because as a results of these weights, negative entries can appear in the element mass matrix. In addition, it should be noted that some caution is required in case the total integral over an element is computed by means of subtraction of the contributions over the subelements. For example, consider an intersected element in 2D and assume that all integrals are evaluated using first order Newton-Cotes (cf. (7.9), 2D). First, the element mass matrix for one phase, say, the solid phase, is computed for the whole element, which results in a diagonal matrix. Next, the element mass matrices are computed for the triangular subelement for both the solid and liquid parameters. The resulting element mass matrices are full matrices, although the off-diagonal elements will be relatively small with respect to the diagonal elements. Now, depending on the parameter values corresponding to both phases, the subtraction of the element mass matrix for the solid phase from the element mass matrix corresponding to the whole element, and the addition of the element mass matrix for the liquid phase, can result in negative entries on the diagonal and off-diagonals of the final element mass matrix. As a consequence, when the total mass matrix is no longer positive definite, the discrete system (7.3) will become unstable.

7.3 Solving the nonlinear system

In the temperature formulation, the heat diffusion equation (7.1) is highly nonlinear, due to the addition of the latent heat term $\frac{\partial f_l}{\partial t}$. In practice, the

solution to the corresponding discretized system of equations (7.3) can be found by either using fixed point iteration or by use of Newton-Raphson. We will discuss both approaches.

Let us consider the residual form of the system of equations (7.3):

$$\Psi(T^{m+1}) = M^{m+1}\frac{T^{m+1} - T^m}{\Delta t} + \frac{L^{m+1} - L^m}{\Delta t} + S^{m+1}T^{m+1} - q^{m+1} = 0. \quad (7.12)$$

Starting with an initial guess $T_0^{m+1} = T^m$, the subsequent approximations of the solution $T_k^{m+1}, k = 1, 2, \ldots$ to (7.12), by means of fixed point iteration, are computed via:

$$T_k^{m+1} = \Psi(T_{k-1}^{m+1}). \quad (7.13)$$

Unfortunately, for our application, this basic iterative scheme hardly ever leads to convergence: in most cases 'flip-flop', in which the solution jumps between two different states, is observed. A means of improving the convergence behavior is the use of weighted under-relaxation:

$$T_k^{m+1} = T_{k-1}^{m+1} + \omega\left[\Psi(T_{k-1}^{m+1}) - T_{k-1}^{m+1}\right]. \quad (7.14)$$

The problem here is that we do not know how to select an optimal value for ω, other than by trial-and-error. Furthermore, if a certain value of ω improves convergence for one time step, this does not automatically guarantee it will also improve the convergence for subsequent time steps.

The nonlinear system (7.12) can also be solved by means of the well-known Newton-Raphson iterative scheme. The main advantage of this approach is that locally quadratic convergence is assured, as soon as the norm of the difference between the numerical solution and the exact solution is less than the radius of convergence.

For the kth iterate of the Newton-Raphson scheme we have:

$$T_k^{m+1} = T_{k-1}^{m+1} + \Delta T_{k-1}^{m+1}, \quad (7.15)$$

where ΔT_{k-1}^{m+1} is the solution of the linear system

$$J(T_{k-1}^{m+1})\Delta T_{k-1}^{m+1} = -\Psi(T_{k-1}^{m+1}). \quad (7.16)$$

The Jacobian J is given by

$$J(T_{k-1}^{m+1}) = \frac{\partial \Psi}{\partial T} = \frac{1}{\Delta t}\left(M_{k-1}^{m+1} + \frac{\partial L_{k-1}^{m+1}}{\partial T}\right) + S_{k-1}^{m+1}. \quad (7.17)$$

The partial derivative of L with respect to the temperature T needs special attention. Let $L_i^{e_i}$ be the element matrix corresponding to element e_i of the vector L_i defined by (7.6), Ω^{e_i} the volume of e_i, and Γ^{e_i} the segment

of the moving boundary contained in e_i. For each entry (i, j) of the element derivative matrix $\frac{\partial L_i^{e_i}}{\partial T_j}$ it holds that

$$\frac{\partial L_i^{e_i}}{\partial T_j} = \rho L \int\limits_{\Omega^{e_i}} \frac{\partial H(T - T_m)}{\partial T_j} \phi_j d\Omega^{e_i}, \tag{7.18}$$

$$= \rho L \int\limits_{\Omega^{e_i}} \delta(T - T_m) \phi_i \phi_j d\Omega^{e_i}. \tag{7.19}$$

It is shown by Fachinotti et al. [24] that the integral (7.19) over Ω^{e_i}, at the finite element level, can be rewritten as an integral over Γ^{e_i}:

$$\rho L \int\limits_{\Omega^{e_i}} \delta(T - T_m) \phi_i \phi_j d\Omega^{e_i} = \rho L \int\limits_{\Gamma^{e_i}} \frac{\phi_i \phi_j}{\|\nabla T\|} d\Gamma^{e_i}. \tag{7.20}$$

As with the fixed point iteration, in practice, divergence of the Newton-Raphson scheme is often observed when highly nonlinear problems are considered. In particular, this concerns problems for which the latent heat is relatively large in comparison to the other physical parameters. The reason for the non-convergence of the Newton-Raphson scheme, is that the computed Newton step ΔT_{k-1}^{m+1}, is too large.

A reasonable strategy to overcome this problem is to minimize the 2-norm of the residual

$$\psi = \|\Psi\|_2^2 = \Psi^T \Psi, \tag{7.21}$$

since every solution to (7.12) minimizes (7.21). Note that the Newton step $p = \Delta T_{k-1}^{m+1}$ is a descent direction for ψ:

$$p^T \nabla \psi = (-J^{-1}\Psi)^T (\Psi^T J) = -\Psi^T \Psi < 0. \tag{7.22}$$

However, there may exist local minima of (7.21) that are no solutions to (7.12). The only remedy then is to start with a different initial guess.

Because p is a descent direction, there exists an α such that $\psi(T_{k-1}^{m+1} + \alpha p)$ is reduced sufficiently. When a satisfactory α is found, the temperature is updated as:

$$T_k^{m+1} = T_{k-1}^{m+1} + \alpha \Delta T_{k-1}^{m+1}. \tag{7.23}$$

Two questions now remain to be answered. What should be the criterion for accepting a step? And how to determine α? It is certainly not sufficient to simply require that $\psi(T_k^{m+1}) < \psi(T_{k-1}^{m+1})$. First of all, ψ could be decreasing too slowly relative to the step lengths. Secondly, one can have a sequence where the step lengths are too small relative to the initial rate of decrease of ψ.

The first problem is fixed by requiring that for $0 < \lambda < 1$:

$$\psi(T_k^{m+1}) \le \psi(T_{k-1}^{m+1}) + \lambda \nabla \psi \left(T_k^{m+1} - T_{k-1}^{m+1}\right), \tag{7.24}$$

$$= \psi(T_{k-1}^{m+1}) + \alpha \lambda \nabla \psi \Delta T_{k-1}^{m+1}. \tag{7.25}$$

According to Reference [54], $\lambda = 10^{-4}$ is a good choice. The second problem can be fixed by requiring that the rate of decrease of $\psi(T_k^{m+1})$ to be greater than some fraction β of the rate of decrease of $\psi(T_{k-1}^{m+1})$.

If the above two conditions are not satisfied for the current Newton update ΔT_{k-1}^{m+1}, a very practical procedure to determine α, taken from Reference [54], is the following line search procedure.

Define

$$g(\alpha) \equiv \psi \left(T_{k-1}^{m+1} + \alpha p\right), \tag{7.26}$$

so that

$$g'(\alpha) = p^{\mathrm{T}} \nabla \psi. \tag{7.27}$$

We start with $g(0)$ and $g'(0)$ available (the initial guess). Recall that we only need to backtrack when the full Newton step (i.e., $\alpha = 1$), is not acceptable. We therefore also have $g(1)$ at our disposal. The idea now is to model g as a polynomial $\tilde{g}$ in α and choose α such that it minimizes the model. This α is found by setting $\tilde{g}'(\alpha) = 0$ and then to solve for α.

In Reference [54] $g(\alpha)$ is modeled as a quadratic polynomial $\tilde{g}(\alpha) = a\alpha^2 + b\alpha + c$ for the first step of the line search:

$$\tilde{g}(\alpha) = [g(1) - g(0) - g'(0)]\alpha^2 + g'(0)\alpha + g(0), \tag{7.28}$$

where a, b and c are easily determined using the known values of $g(1)$, $g(0)$ and $g'(0)$. A minimum is found when

$$\alpha = -\frac{g'(0)}{2[g(1) - g(0) - g'(0)]}. \tag{7.29}$$

On second and subsequent backtracks, $g(\alpha)$ is modeled as a cubic polynomial in α. Here, the previous value $g(\alpha_1)$ and the second most recent value $g(\alpha_2)$ are used:

$$\tilde{g}(\alpha) = a\alpha^3 + b\alpha^2 + g'(0)\alpha + g(0). \tag{7.30}$$

Requiring this expression to give the correct values of g at α_1 and α_2 leads to two equations that can be solved for the coefficients a and b:

$$\begin{bmatrix} a \\ b \end{bmatrix} = \frac{1}{\alpha_1 - \alpha_2} \begin{bmatrix} 1/\alpha_1^2 & -1/\alpha_2^2 \\ -\alpha_2/\alpha_1^2 & \alpha_1/\alpha_2^2 \end{bmatrix} \cdot \begin{bmatrix} g(\alpha_1) - g'(0)\alpha_1 - g(0) \\ g(\alpha_2) - g'(0)\alpha_2 - g(0) \end{bmatrix}. \tag{7.31}$$

For the cubic model (7.30) the minimum is at:

$$\alpha = \frac{-b + \sqrt{b^2 - 3ag'(0)}}{3a}. \tag{7.32}$$

It can be shown that, since the Newton step failed, $\alpha \lesssim \frac{1}{2}\alpha_1$ for small λ. Besides, we need to guard against too small a value of α. It is thus advisable to require that at most $\alpha_{\min} = 0.1\alpha_1$.

One could ask oneself whether the use of a cubic polynomial approximation is really necessary. We therefore propose the use of a quadratic model for all backtracking steps:

$$\tilde{g}(\alpha) = a\alpha^2 + b\alpha + c, \tag{7.33}$$

where a, b and c are found using the known values of $g(\alpha_1)$, $g(\alpha_2)$ and $g'(\alpha_2)$ and are given by:

$$a = \left[g(\alpha_1) - g(\alpha_2) + g'(\alpha_2)(\alpha_2 - \alpha_1)\right]/(\alpha_2 - \alpha_1)^2, \tag{7.34}$$
$$b = g'(\alpha_2) - 2a\alpha_2, \tag{7.35}$$
$$c = g(\alpha_2) - g'(\alpha_2)\alpha_2 + a\alpha_2^2. \tag{7.36}$$

The minimum for this quadratic form is found at

$$\alpha = \alpha_2 - g'(\alpha_2)/2a. \tag{7.37}$$

For many problems it often even suffices to simply model $g(\alpha)$ as a linear function. Using only $g(\alpha_1)$ and $g'(\alpha_1)$, $\tilde{g}(\alpha)$ can be defined as:

$$\tilde{g}(\alpha) = g(\alpha_1) - g'(\alpha_1)\alpha_1. \tag{7.38}$$

Instead of computing α from $\tilde{g}'(\alpha_1) = 0$, which would make no sense, we solve for α from $\tilde{g}(\alpha) = 0$ to find:

$$\alpha = \alpha_1 - g(\alpha_1)/g'(\alpha_1). \tag{7.39}$$

Fachinotti et al. seem to take a slightly different approach to minimize the residual norm. They determine the parameter α by requiring orthogonality between the residual vector $\Psi(T_k^{m+1})$ and the search direction ΔT_{k-1}^{m+1}, i.e.,

$$G^k = \left[\Delta T_{k-1}^{m+1}\right]^{\mathrm{T}} \Psi(T_k^{m+1}) = 0. \tag{7.40}$$

For the first linesearch step, G^k is approximated by a linear polynomial, while quadratic regression is applied for the successive backtracking steps.

Nonetheless, (7.40) does not make much sense: if we require $\Psi(T_k^{m+1}) = 0$, then why would it be any better to take the inner product with the search direction? Note that if we multiply the residual by the Jacobian matrix, the following holds

$$(\Delta T_{k-1}^{m+1})^{\mathrm{T}} \left[\Psi(T_{k-1}^{m+1})^{\mathrm{T}} J(T_{k-1}^{m+1})\right] = (\Delta T_{k-1}^{m+1})^{\mathrm{T}}\nabla\psi = g'(\alpha), \tag{7.41}$$

which is exactly (7.27)!
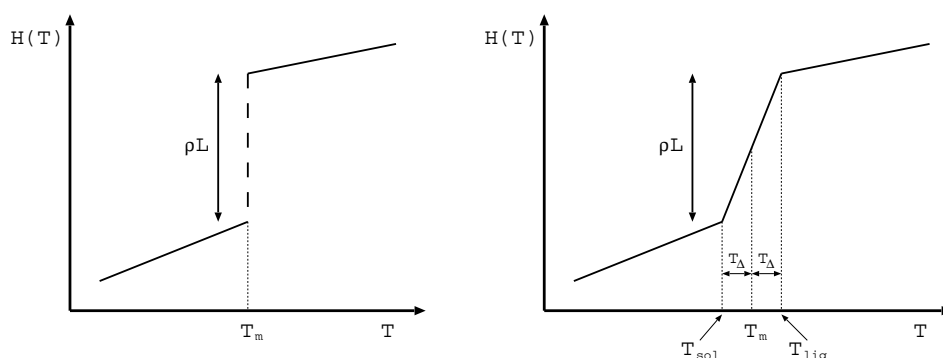
Figure 7.4: *Enthalpy H as function of temperature T. Isothermal (left) and mushy (right).*

7.4   The addition of a source term to an isothermal problem

Most test cases found in the literature on Stefan problems consider moving fronts induced by boundary conditions on the fixed boundaries of the computational domain. This restriction also holds for the paper by Fachinotti et al. However, in optical rewritable recording, marks are formed as a result of the absorption of the energy contained in the incident laser light. In other words, our isothermal model for the melting component of the mark formation process, introduced in Chapter 3, is governed by a source term, not by boundary conditions on the fixed boundaries.

Besides, without loss of generality, it may be assumed that the amorphous mark is to be created in a fully crystalline background. For our isothermal model, this implies that initially there exists no moving boundary. Unfortunately, in practice the eventual creation of a new moving front can lead to poor convergence of the Newton Raphson scheme. At first, a reduction of the time step can prove beneficial, but for increasingly larger values of the latent heat, a breakdown of the iterative procedure is imminent.

To illustrate this problematic behavior of the numerical solution, let us consider a temperature distribution at time level $t = t_n$, as sketched in Figure 7.5. The time step is $\Delta t = 1$. Now assume that at the next time instance, part of the numerical solution reaches the melting temperature T_m, at which point the latent heat come into effect. At this stage, typically an overshoot of one of the nodes is observed. Moreover, the number of Newton iterations increases considerably and backtracking is used heavily.

Next, assume that we successfully acquired a solution at $t = t_{n+1}$ (which in general is not even guaranteed), but failed to obtained a solution at time level t_{n+2} (within the specified maximum number of Newton iterations). Further assume that a second attempt, this time using a time step that is
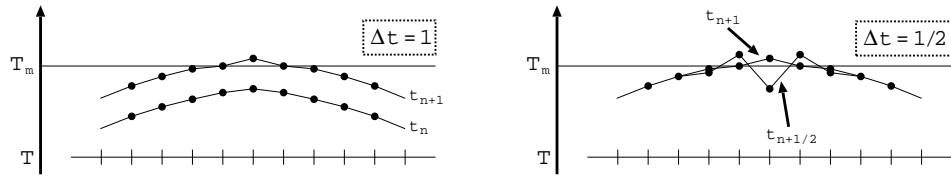
Figure 7.5: *The appearance of a new (source term induced) moving interface: evolution of the numerical solution in time. Isothermal case. The numerical solution mainly oscillates between two states; amplitudes decrease with the reduction of the time step.*
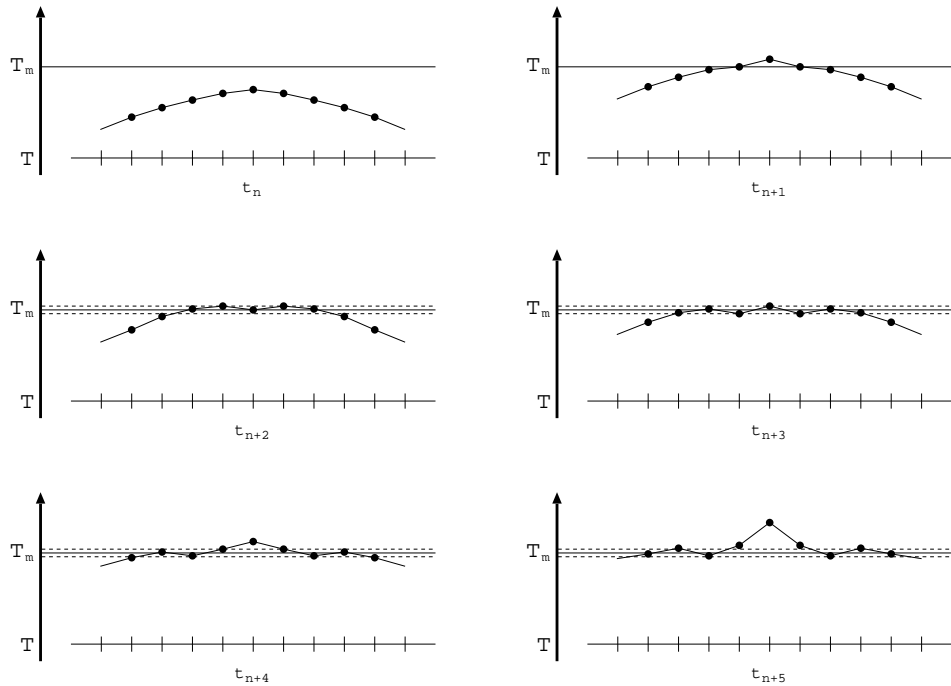
Figure 7.6: *The appearance of a new (source term induced) moving interface: evolution of the numerical solution in time. Mushy case. Only minor oscillations within the mushy band; no time step reduction.*

half the size of the original one, is successful. Most likely, the newly obtained solution shows several overshoots and undershoots. With each successive attempt, as the time step is consecutively reduced, the acquired solutions will oscillate between the two states shown in Figure 7.5. Not surprisingly, the amplitudes of the oscillations decrease with the reduction of the time step.

To counteract this impracticality, we propose the introduction of an artificial mushy region. This regularization of the enthalpy allows the approximating solution to lie within a small band (the mushy region) around the melting temperature T_m. The bounds of the artificial mushy region are determined by two values of the temperature, which we denote by T_{sol} and

T_{liq}, see Figure 7.4. These bounds are determined via a parameter T_Δ as:

$$T_{\text{sol}} = T_m - T_\Delta, \qquad T_{\text{liq}} = T_m + T_\Delta. \tag{7.42}$$

In general, a value of, say, 0.1% of the melting temperature, is sufficient to obtain good convergence behavior of the Newton scheme, while at the same time the time step can be kept constant. Smaller values of T_Δ may require a few reductions of the time step, although with respect to the accuracy, the gain is minimal.

The effect of the artificial mushy region on the evolution in time of the temperature distribution, taken from the previous example, is sketched in Figure 7.6. Note that, since the enthalpy is regularized, it is also continuous. Therefore, the enthalpy can take on any value in the range of the jump from 0 to ρL. And thus, as can be seen from the figure, the artificial region allows for minor oscillations of the numerical solution around the melting temperature.

The application and performance of the artificial mushy region will be further discussed in Section 9.3.2. In particular, we will focus on the choice of the regularization parameter T_Δ.

7.5 Evaluation of the method

For a large variety of test problems, the above discussed temperature approach outperforms the enthalpy methods. Computational costs seem to be less and, probably most importantly, the moving interface is found to show hardly any wiggles and stair-casing is considerably reduced.

Nonetheless, a few issues should be addressed:

- Although the temperature method performs extremely well for relatively small values of the latent heat L, the performance deteriorates when L becomes relatively large. This problem can be (partly) remedied with the addition of a line search procedure to the Newton Raphson solver. A good estimate of the parameter α, used to scale the Newton step, can be determined using either linear, quadratic or cubic regression.

- The addition of an external source to the temperature formulation, in combination with larger values for the latent heat, gives rise to plateaux: temperature values of all the nodes of one or more elements take on values that are (up to a very small tolerance, say $O(10^{-6})$) equal to the melting temperature T_m during several consecutive time steps. As a result, the convergence of the Newton scheme is heavily affected, and the method often breaks down completely. This complication can be resolved by introducing an artificial mushy region.

CHAPTER 8

Adaptive local mesh refinement

A refinement of the computational mesh often proves to be invaluable, in particular in case of extremely large industrial applications. Therefore, in this chapter, several strategies considering adaptive local mesh refinement are discussed, and a refinement strategy is selected. In Section 8.4 the implementation of the preferred strategy is described in detail.

8.1 Introduction

The accuracy of a finite element solution is affected by the total number and size of the elements that are used. On fine grids, a higher level of accuracy can be expected than on coarse grids. Globally refining an existing mesh, however, is very impractical. Computational time and storage space can soon become huge, especially in 3D.

An obvious means of resolving this major drawback of global refinement is to limit the refinement to selected regions of the computational domain. Typically, these regions are assigned for refinement based on a priori knowledge about particular characteristics of the solution or the geometry of the domain. In case of Stefan problems, the estimated position of the moving boundary presents a good indication of where to refine the mesh. Of course, as a result of the movement of the interface, the regions that are to be refined can constantly change during a computation.

Ideally, a typical local refinement code has the following properties:

- Adaptive: an advancing interface or changes in geometry can be resolved.

- Preserving: the quality of the mesh does not degrade during successive refinements.

- Efficient: the amount of refinement and the corresponding gain in accuracy are balanced.

- Practical: the construction of the refinement and the data structure used, are uncomplicated.

The refinement strategy and data structure discussed in this chapter have been developed as an integral part of the Sepran finite element package [58]. Since the larger part of the information on the structure of the mesh is available within the Sepran code, the data structure presented here is specifically designed to facilitate the addition of the local adaptive mesh refinement to the Sepran package. An important feature of our design is that the implementation of the data structure is such that it is independent of the spatial dimension.

Although most of the principles of the local mesh refinement as described in this chapter are generally applicable, some aspects specifically relate to Stefan problems, and solid-liquid transitions in particular.

8.2   Basic terminology

Before discussing the local mesh refinement, it is convenient to first introduce some basic terminology, which is used throughout the text.

By *refinement* we mean the subdivision of an element into sub-elements. Our subdivision is always the result of the division of at least one edge of the element into two new edges. A new node is added at the intersection point of the divided edge. This node is always connected to either an 'opposite' vertex of the original element, or another added node. *Hanging nodes*, i.e., nodes that are not a vertex of all sub-elements containing this node, are thus avoided. As such, a 1D line element is always divided into two line elements, a 2D triangular element is at most subdivided into 4 subtriangles, and a 3D tetrahedral element is at most divided into 9 subtretrahedra. Throughout this chapter it is assumed that an edge is always split up into two equally sized subedges.

If all of the subelements of an already refined element are refined as well, we say that the initial element is refined twice, or put differently, that the *level of refinement (LOR)* of the initial element is *of the order two*.

Two elements are called *direct neighbors*, in case they share at least one vertex. These elements are said to be *at 'distance' 1*. The 'distance' between an element and a direct neighbor of a direct neighbor of this element is equal to 2, etc.

The initial mesh, i.e., the mesh at the beginning of a computation at $t = t_0$, is called the *basis mesh*. Elements of the basis mesh are referred to as *basis elements*.

In case of isothermal moving boundary problems, an element is called an *intersected element*, when at least one of the vertices has a temperature value larger than the melting temperature T_m, and at least one node for which $T < T_m$. If a mushy region is considered, the element is an intersected element when at least one of the nodes has a temperature smaller than the solidification temperature T_{sol} or the liquification temperature T_{liq}, and at least one node for which the temperature is larger. When the whole element is mushy ($T_{sol} < T < T_{liq}$), it is also considered to be intersected.

When an element of the basis mesh is assigned to be refined, the element is said to be marked for refinement, or simply *marked*.

8.3 Local refinement strategies

Whenever a local refinement of a mesh is required, the first decision to be made is which elements are to be refined. A generally accepted and commonly used criterion for element refinement is based on a computed element wise error of the approximated solution with respect to some reference solution. Those elements for which the error is larger than a given tolerance, are marked to be refined.

However, in general this approach requires some error estimate based on theory or knowledge on the exact (analytic) solution. For practical applications, such reference solutions generally do not exist. An obvious alternative is to refine in a neighborhood where difficulties or inaccuracies can be expected. A priori knowledge of these locations often exists, based on for instance properties of the computational domain. One could think of composite geometries with discontinuous material properties, or kinks. In particular, the position of the moving boundary, as for example in our melting model, gives a very good indication of where mesh refinement can be beneficial.

A problem that arises when moving boundary problems are considered, is that the interface displacement can be rather unpredictable. Although the interface velocity can be estimated, given the governing equation and the values for the physical parameters, the merging and breaking up of multiple fronts most likely gives rise to irregularities. An obvious cause of these difficulties lies of course in the discontinuity of the derivative of the temperature across the moving interface.

In general, it is to be ensured that after one time step of the numerical scheme, the moving interface always ends up in the same, or at most adjacent basis elements. This strict requirement guarantees that the latent heat contribution is dealt with appropriately (in discrete sense). One might consider this as a kind of Courant-Friedrich-Lewy criterion. Since the moving interface is restricted to advance at most to adjacent elements, it follows that the minimal region to be marked for refinement consists of the intersected
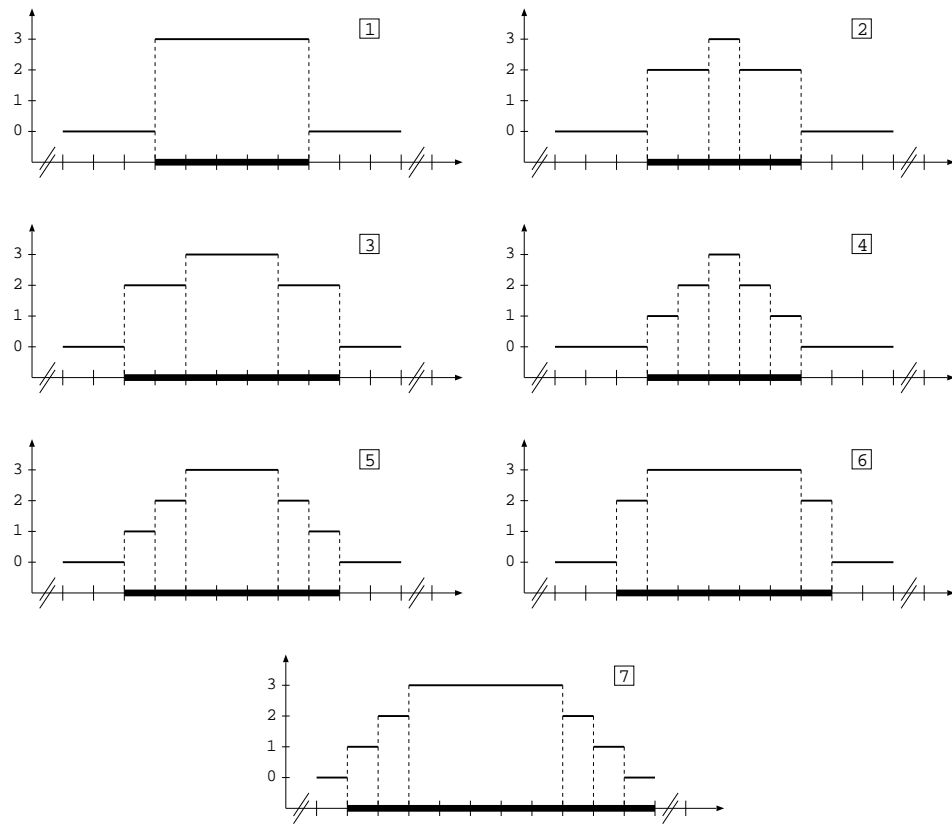
Figure 8.1: *Graphical representation of seven means of assigning an LOR to marked elements (bold elements). The central element is assumed to be intersected. The height of the bar on top of each element indicates the assigned LOR (vertical axis).*

elements, and their direct neighbors. The collection of marked elements forms a so-called *band of refinement*. The width of this band of refinement, an integer value referred to as the *width of the refinement*, is defined as the maximum minimal 'distance' between a marked (non-intersected) element and the intersected elements. For example, in case only the direct neighbors of the intersected elements are marked for refinement, it has a value of 1. If, in addition, the direct neighbors of these direct neighbors are also marked, then the width of the refinement is equal to 2, etc.

Because of our CFL-like criterion, it can thus be concluded that the minimal width of the refinement is equal to 1. The final width of the refinement depends on two choices. Firstly, the maximum 'distance' from the intersected elements at which elements are assigned the highest LOR, must be selected. Secondly, in case more elements are to be refined, it should be decided whether these basis elements are all refined at a lower, but constant, LOR, or that the assigned LOR is gradually reduced depending on the 'distance' from the intersected elements.

Figure 8.1 shows a 1D graphical representation of a variety of ways in which basis elements can be assigned an LOR. If all elements are refined the same number of times as in option 1, say, with a LOR of the order two or more, the transition from the refined grid to the coarse grid can be quite abrupt. In particular when the band of refinement consists only of the intersected elements and their direct neighbors, this choice could have a negative impact on the effectiveness of the refinement. The same argument holds for options 2, 3 and 6.

It is also best avoided to assign the highest LOR to just the intersected elements, as in options 2 and 4. When the moving interface advances to adjacent elements, a loss of accuracy would be the result of the adjacent elements being coarser. This loss of accuracy can be easily avoided by at least giving the directly neighboring elements the same LOR as the intersected elements.

In short, the fifth and seventh option are the most favorable. Of these two alternatives, option 5 seems to be the best choice, because it will lead to the least total number of elements in the refined mesh.

Next, it has to be decided how to realize the actual refinement of the marked elements. Three different refinement strategies can be employed:

- Refine each basis element the assigned number of times at once. Consider the basis elements one at a time, sequentially.

- Perform a single refinement of all basis elements that need to be refined at least once. Next, refine the subelements of the basis elements that are marked to be refined twice or more. Repeat this procedure until all basis elements are refined the assigned number of times.

- Perform a single refinement of all basis elements that have the highest assigned LOR. Then refine each element that has an LOR that is one smaller. Continue this process until all marked basis elements are refined as intended.

To make these refinement strategies more illustrative, let us look at a 2D example. Consider a segment of a basis mesh consisting of four elements, as shown in Figure 8.2. For simplicity, let us assume that element 3 has been marked to be refined twice and the adjacent elements 2 and 4 are marked to be refined once.

Remark that as a result of the refinement of some of the basis elements, neighboring elements need to be subdivided, even when they are not marked for refinement, in order to avoid hanging nodes. The way in which these hanging nodes are avoided can have a major effect on the final mesh. Let us consider the first refinement strategy. In case the hanging nodes are corrected for in adjacent elements each time a basis element is refined to the assigned LOR, the quality of the resulting mesh deteriorates considerably, as is shown in Figure 8.2.
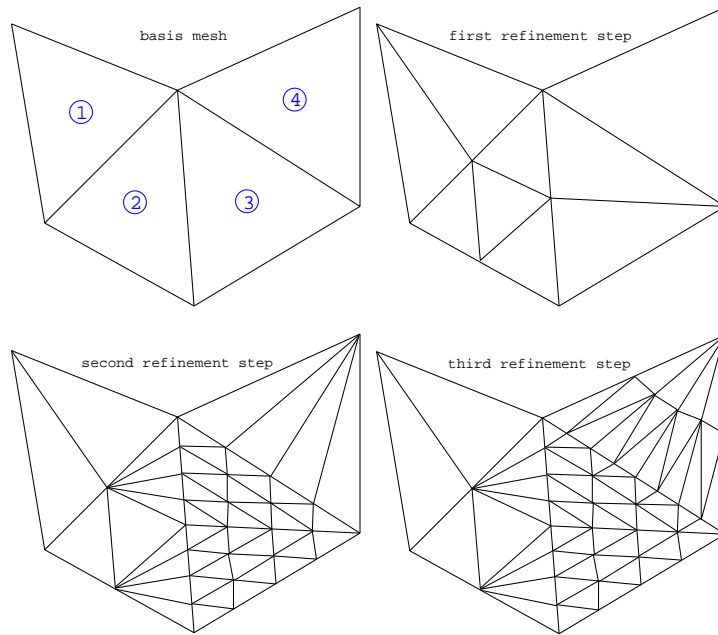
Figure 8.2: *Refinement strategy S1. Elements are refined successively. Subdivided elements that are created to avoid hanging nodes inherit the LOR of the original basis element.*
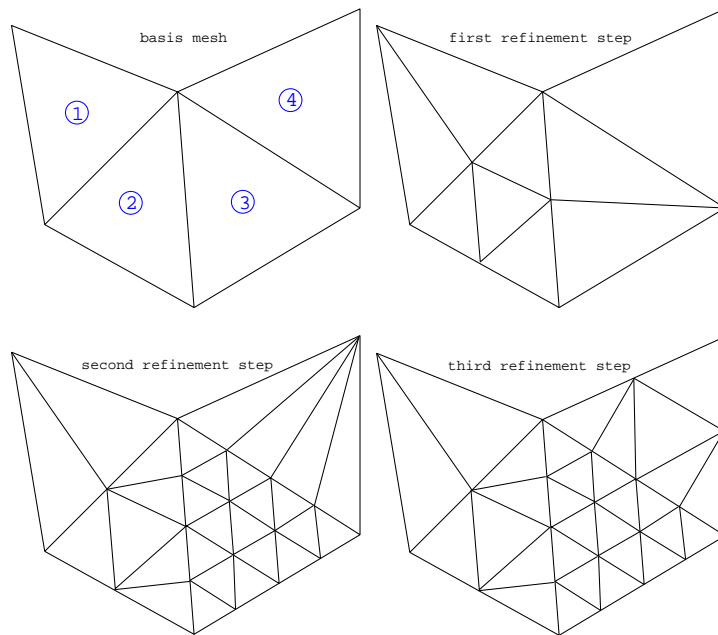
Figure 8.3: *Refinement strategy S1. Elements are refined successively. Subdivided elements that are created to avoid hanging nodes are removed. Refinement proceeds from the associated basis element onward.*
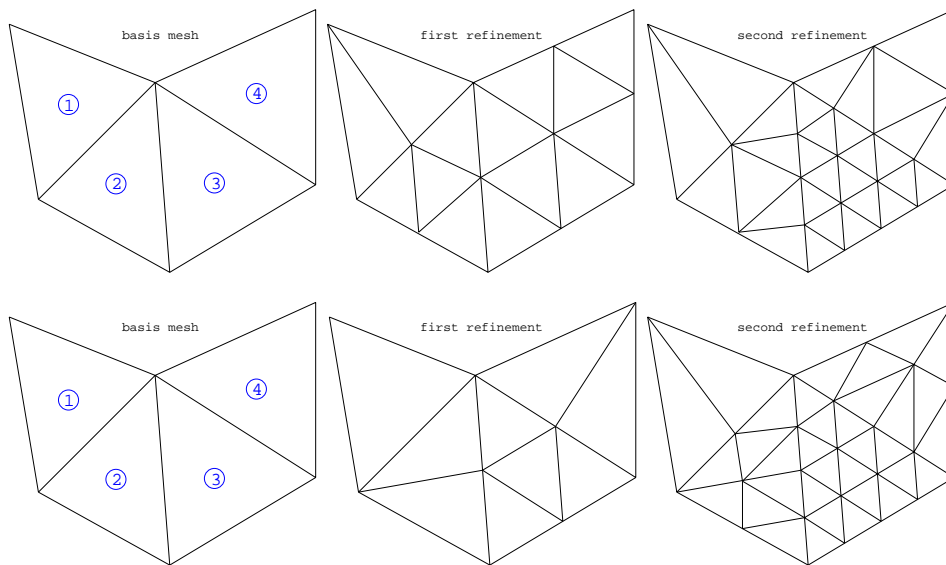
Figure 8.4: *Refinement strategies S2 (top) and S3 (bottom). Refinement proceeds per LOR. Subdivided elements that are created to avoid hanging nodes are removed. Refinement proceeds from the associated basis element onward.*

A better approach is to remove the subelements that are the result of previous corrections of hanging nodes, then to refine the original basis element the required number of times, and finally to deal with newly created hanging nodes, see Figure 8.3. Of course, this is very impractical with respect to the implementation, because a lot of precise bookkeeping is required.

Therefore, it is advisable to choose either the second or third mesh refinement strategy, as shown in Figure 8.4. Of these two options, strategy S2 is the best alternative. Firstly, the refinement of the mesh changes the most gradually. Secondly, the total number of elements (and unknowns) of the final mesh is the smallest. Furthermore, unnecessary interpolations during transitions from one mesh to another are avoided, since all the nodes of refined basis elements with a low LOR are always also nodes of subdivided basis elements with a higher LOR.

Finally, a decision has to be made on how to implement the transition from an existing locally refined mesh to the next. Two basic approaches can be distinguished:

- First refine the elements that need further refining. Then coarsen those elements that are assigned a lower LOR than before.

- Start from the basis mesh and refine the mesh employing refinement strategy S2 or S3.

Each of these approaches has been illustrated in Figure 8.5. As a starting mesh, a refined mesh obtained using strategy S3 is considered (cf. Fig-

ure 8.4). It is assumed that for the mesh to be created, element 2 has been marked to be refined twice and the adjacent elements 1 and 3 are marked to be refined once. This could for instance occur when a moving interface advances from element 3 to element 2.

From Figure 8.5 it immediately becomes clear that building a new locally refined mesh is best done starting from the basis mesh. The number of elements, and thus the number of unknowns, is less. Besides, no irregularly shaped elements appear, as a result of compensating for what otherwise would have been hanging nodes. Furthermore, the mapping of data between meshes becomes almost trivial.

Finally, it is important to stress that the coarseness of the basis mesh is restricted to be such that the accuracy of the solution to a problem without latent heat is guaranteed on this mesh. If not, there is no use in refining the mesh locally.

In conclusion, a practical strategy for locally refining a mesh has the following characteristics:

- Always construct the refined mesh from the basis mesh.

- Always refine the intersected basis elements and the direct neighbors (CFL-like condition).

- Mark the intersected basis elements and the direct neighbors to get the highest LOR. The remaining marked elements get a lower LOR, which gradually reduces with the 'distance' of the elements from the intersected elements.

- Perform a single refinement of all basis elements that need to be refined at least once. Next, refine the subelements of the basis elements that are marked to be refined twice or more. Repeat this procedure until all basis elements are refined the assigned number of times.

8.4   Implementation of the local mesh refinement

In the previous section we have derived an optimal strategy for locally refining a mesh. In this section, the implementation of this refinement strategy is discussed. The backbone of the local refinement code is the so-called *outer loop*. The structure of the outer loop can be split up into five parts:

1. initialization of the data structure

2. solution of the governing equation for a single time step on the current (refined) mesh

3. if needed, construction of new refined mesh

Algorithm 1: Outer refinement loop.

---

1 extract parameters from input
2 **if** *first time this routine is called* **then**
3 | create and initialize auxiliary arrays

4 **while** *no convergence and not iterations ¿ maxiter* **do**
5 | solve governing equation
6 | **if** *no convergence* **then**
7 | | reset time and data to previous time level
8 | | modify time step

9 determine necessity of refinement (**new solution**), and mark elements
10 **if** *refinement necessary* **then**
11 | fill auxiliary arrays
12 | construct new refined mesh

13 **if** *interface outside refinement* **then**
14 | reset time and data to previous time level
15 | possibly modify time step
16 **else**
17 | map data to new mesh
18 | update auxiliary arrays

---

4. if the mesh has been adapted, mapping of the data to the new mesh

5. if needed, adaptation of the time step

Each step of the outer loop, except of course the initialization of the data structure, which is only needed at the very beginning of a computation, is processed during each time level of the numerical time integration process. Next, we will address steps 3 to 5 of the outer loop in more detail, see Algorithm 1.

8.4.1   Marking elements for refinement

When the numerical solution to the governing equation has been computed at the new time level on a previously refined mesh, this solution is used to determine whether the *old mesh* should be adapted, and if so, how. To this end, first an array *update* is created of which the length is equal to the number of elements of the old mesh. If an element of the old mesh is intersected, the corresponding entry in array *update* is set equal to '1', if it is not intersected, the entry is set equal to '0', see Figure 8.6.

Next, an array *refinenew* is filled, of which the length is equal to the number of elements of the basis mesh. At this stage, array *refinenew* has
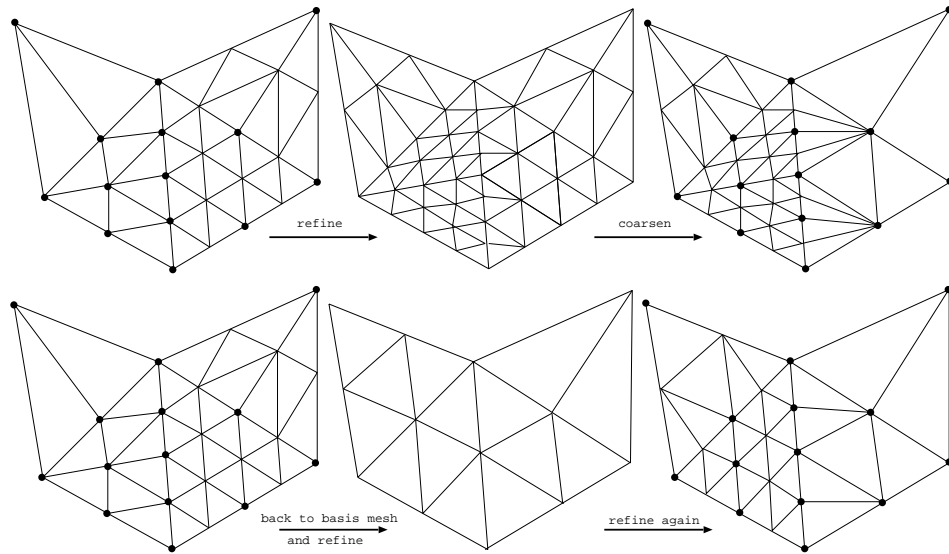
Figure 8.5: *Two ways of implementing the transition from one mesh to another. Top: first refine and then coarsen. Bottom: rebuild mesh from basis mesh. The nodes indicated with a '•' are common to all final meshes.*

essentially the same functionality as array *update*, but now for the basis mesh. If the old mesh is equal to the basis mesh then filling array *refinenew* is trivial: *refinew* becomes an exact copy of array *update*. In case the old mesh differs from the basis mesh, a auxiliary array called *refmapold* is used, which contains mapping information on how the elements of the refined old mesh relate to those of the basis mesh. The addition 'old' in the name 'refmapold' indicates that the array contains information concerning the old mesh. In the same way, the addition 'new' in the name refinenew indicates that the array contains information with respect to the new mesh. For a detailed explanation of array *refmap* we refer to Section 8.4.3. If one or more elements of the old mesh, that are subelements of the same basis element, are marked for refinement, the corresponding entry of array *refinenew* is also marked.

Now that all basis elements that are intersected by the moving interface have been marked, the band of refinement surrounding the intersected elements is created. First the entries of array refinenew that contain a '1' are replaced by a number equal to the desired LOR plus one. In this way, the intersected elements can later be distinguished from the adjacent elements. The entries of array refinenew that correspond to the direct neighbors are assigned a value equal to the LOR. Next, the elements adjacent to these elements are given a lower LOR, which gradually reduces with the 'distance' of these elements from the intersected elements. In pseudo-code, the marking of the elements proceeds as shown by Algorithm 2.
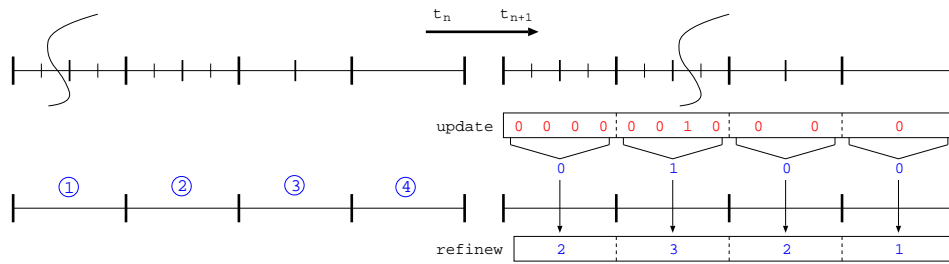
Figure 8.6: *Filling of the refinement vector. Entries of array update that correspond to an intersected element of the old mesh are assigned a value of '1'. Basis elements are marked for refinement if at least one of its subelements is marked. The corresponding positions in array refinenew are assigned a value LOR_{max}. Finally, neighboring elements are assigned LOR values in accordance with the employed refinement strategy.*

Algorithm 2: Marking of elements.

---

1 fill array update
2 fill array refinenew
3 **foreach** *LOR* **do**
4 | mark neighboring elements

Algorithm 3: Mesh construction outer loop.

---

1 start with basis mesh
2 create and initialize auxiliary arrays
3 **foreach** *LOR* **do**
4 | construct intermediate mesh
5 finalize new mesh

8.4.2 Construction of the refined mesh

Obviously, by far the most important part of the mesh refinement code considers the actual construction of the refined mesh. This process consists of an outer loop over all LOR, and an inner loop over all elements of the basis mesh. The outer loop is straightforward, as shown by Algorithm 3.

At this point it is important to explain up to some degree of detail the way in which a mesh is generated and stored in the Sepran finite element package [58]. To illustrate the construction process of a mesh in Sepran, let us consider a 2D triangulation. Initially, one starts with a single triangular element. This element is labeled to be element number '1', and the vertices and edges are each assigned labels '1' to '3'. Information on the numbering of the vertices, edges and elements is stored in separate arrays. In addition, information is stored on the connections between vertices and edges, vertices and elements, and edges and elements.

Algorithm 4: Mesh construction inner loop.

---

1 **foreach** *edge* **do**
2   **if** *edge is intersected* **then**
3   mark edges to be subdivided

4 **foreach** *element* **do**
5   **if** *at least one edge is marked* **then**
6   assign required subdivision of element

7 **foreach** *marked element* **do**
8   remove old element
9   create new nodes
10   create new edges
11   add new elements
12   fill auxiliary arrays

When a second element is added, first a new node is added to the list of vertices. This node is assigned the label '4'. Then, two edges, numbered '5' and '6' are added to the list of edges. Next, element number '2' is added to the array of elements. Finally, the information on the connections between the vertices, edges and elements is updated in accordance with new mesh. Each successive element is added accordingly.

Let us return to the refinement of an existing mesh. As explained in Section 8.3, a refined mesh is built up starting from the basis mesh. Then, for each LOR, Algorithm 4 is applied.

In short, the general idea behind the inner loop is to sequentially expand the basis mesh by taking out basis elements that are to be refined, and adding the appropriate subelements to the new mesh. The described procedure is best illustrated by means of an example. Consider a basis mesh consisting of three elements as shown in Figure 8.7, and assume that element '2' is marked to be refined once.

In this situation, the contents of the array in which the numbering of the elements is stored is: '1', '2' and '3'. The vertices are numbered '1' to '5', and the edges are labeled '1' to '7'. Since element '2' is assumed to be refined, the edges '3', '4' and '5' are marked to be subdivided. Because edge '3' is shared by elements '1' and '2', element '1' is marked to be subdivided into two subelements. Element '2' is labeled to be divided into 4 subelements, since all its edges are marked to be subdivided. For element '3' the same argument for subdivision holds as for element '1', because of edge number '4'.

During the refinement process, as illustrated in Figure 8.7, several auxiliary arrays are filled. A new version of each of these arrays is created for each newly adapted mesh. A version of each of these arrays associated with
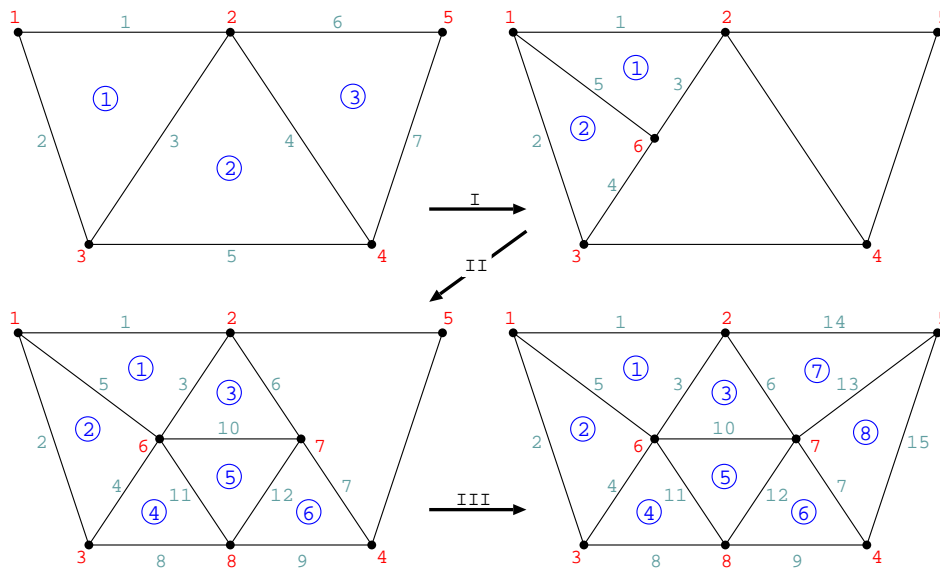
Figure 8.7: *Sketch of the refinement procedure. Basis element '2' is to be refined once.*

a previously refined mesh is always stored, since they are useful for the mapping of the data or when the time level is reset to the previous time level.

Arrays *intnodes* and *parentnodes* are later used for the mapping of the data from the previous mesh to the newly created mesh. Array *refmap* is used to fill array *update*, see Section 8.4.1, and to fill array *intnodes*. The auxiliary arrays that are discussed here are:

- *refmap*: contains mapping information on how the elements of the new mesh relate to those of the basis mesh.

- *intnodes*: contains for each basis element the node numbers of all the vertices that are added during the subdivision, for all LOR. These added nodes are called *internal nodes*.

- *parentnodes*: contains for each added node, the node numbers of the end points of the edge that this node was added on during the subdivision. These two end nodes are referred to as *parent nodes* of the added node.

For each element of the refined mesh, array *refmap* contains two integer values. The first integer is the number of the basis element, the *parent element*, of which this element of the refined mesh is a subelement. The second number is the assigned LOR of the parent element. The total length of array *refmap* is equal to two times the number of elements of the refined mesh.
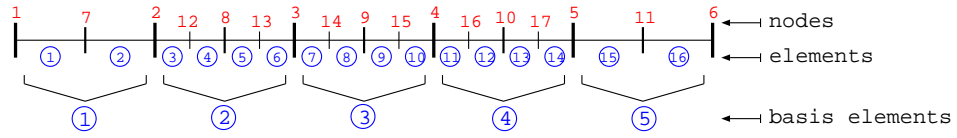
Figure 8.8: *Example of a 1D refined mesh consisting of 5 basis elements.*

If, for instance, a 1D refined mesh as sketched in Figure 8.8 is considered, then array *refmap* has the following contents: 1, 1 | 1, 1 | 2, 2 | 2, 2 | 2, 2 | 2, 2 | 3, 2 | 3, 2 etc.

By far the most difficult array to construct, is auxiliary array *intnodes*. The contents of array *intnodes* consists of two parts. Let N_{basis} be the number of elements of the basis mesh. The first N_{basis} entries of array *intnodes* contain pointers to positions larger than N_{basis} of the array, where the numbers of the internal nodes for each basis element are stored. These node numbers per basis element form the second part of array *intnodes*. Because the required LOR for each basis element has been determined beforehand, the number of internal nodes per basis element to be refined can easily be calculated. The number of internal nodes for each dimension and required LOR is computed as follows:

- $2^{\text{LOR}} - 1$ (1*D*)
- $(2^{\text{LOR}} + 1) * (2^{\text{LOR}-1} + 1) - 3$ (2*D*)
- $(2^{\text{LOR}} + 1) * (2^{\text{LOR}} + 2) * (2^{\text{LOR}} + 3)/6 - 4$ (3*D*)

The number of internal nodes for the most relevant situations are shown in Table 8.1. The length of array *intnodes* is thus equal to N_{basis} plus the total number of internal nodes. In the second part of array *intnodes*, the node numbers of the internal nodes are stored in the order in which the nodes are added to the new mesh. This ordering of the nodes numbers is particularly important for the mapping of data from one mesh to another. Information concerning the parent element, such as the assigned LOR, is obtained from array *refmap*.

For the 1D refined mesh as shown in Figure 8.8, array *intnodes* has the following contents: 6, 7, 10, 13, 16 || 7 | 8, 12, 13 | 9, 14, 15 | 10, 16, 17 | 11. This array was constructed and filled as follows. Assume that each basis element has been assigned a LOR: basis elements '1' and '5' are refined once, the other basis elements twice. The length of array *intnodes* is thus equal to 5 + 2*1 + 3*3 = 16. The first five entries of array *intnodes*, the pointers to the starting positions of the information for each basis element, can now be filled. Then, a loop over all elements that need to be refined at least

once is performed. This fills the first position in each segment of the array corresponding to the various basis elements. After a second loop, this time over all elements that have an LOR equal to 2, the remaining entries are filled.

The structure of array *parentnodes* is simple. Let n_{basis} be the number of nodes of the basis mesh. Then the first two positions of array *parentnodes* contain the node numbers of the parent nodes of internal node number $n_{\text{basis}} + 1$, the third and fourth position of array *parentnodes* contain the node numbers of the parent nodes of internal node number $n_{\text{basis}} + 2$, etc. The length of array *parentnodes* is therefore equal to two times the number of internal nodes. For the 1D refined mesh as shown in Figure 8.8, array *parentnodes* has the following contents: 1, 2 | 2, 3 | 3, 4 | 4, 5 | 5, 6 | 2, 8 | 8, 3 | 3, 9 | 9, 4 | 4, 10 | 10, 5.

8.4.3 Mapping of the data vectors

The final step of the mesh refinement considers the mapping of the data vectors from the old to the newly refined mesh. In case the temperature method is considered, a typical data vector contains the temperature. The mapping takes advantage of the manner in which the refined mesh is constructed. The most important aspect of course is the fact that each consecutive LOR further refines the subelements that results from a previous refinement. In this way, a newly refined basis element with a certain LOR always shares all its nodes with the same basis element at a previous time level and with a higher LOR. If the newly refined element has a higher LOR than before, only a few (linear) interpolations are needed. The procedure describing the mapping of the data is shown in Algorithm 5.

To illustrate the mapping procedure, consider the transition from an old refined mesh to a newly refined mesh, as shown in Figure 8.9. In the first step of the mapping, data is copied for nodes '1' to '4'. These nodes are the vertices of the basis elements, and are therefore always part of each mesh. The numbering of these nodes is also always the same. Next is the mapping of basis element '1'. Because in the old mesh the LOR of this basis element is one order higher than that of the new mesh, it suffices to simply perform a one-on-one mapping of the data of nodes '5' to '7' of the old mesh to the nodes '6', '5' and '7' of the new mesh.

Table 8.1: *The number of internal nodes per dimension and LOR.*

	LOR = 1	LOR = 2	LOR = 3
1D	1	3	7
2D	3	12	42
3D	6	31	161

Algorithm 5: Mapping of data vectors.

---

1 foreach *node of the basis mesh* **do**
2 │ make a one-on-one copy of the data

3 foreach *basis element* **do**
4 │ **if** *LOR of old mesh >= LOR of new mesh* **then**
5 │ │ **foreach** *common node unequal to those of the basis mesh* **do**
6 │ │ │ make a one-on-one copy of the data
7 │ **else**
8 │ │ **foreach** *common node unequal to those of the basis mesh* **do**
9 │ │ │ make a one-on-one copy of the data
10 │ │ **foreach** *remaining node of the new mesh* **do**
11 │ │ │ **foreach** *LOR* **do**
12 │ │ │ │ interpolate data
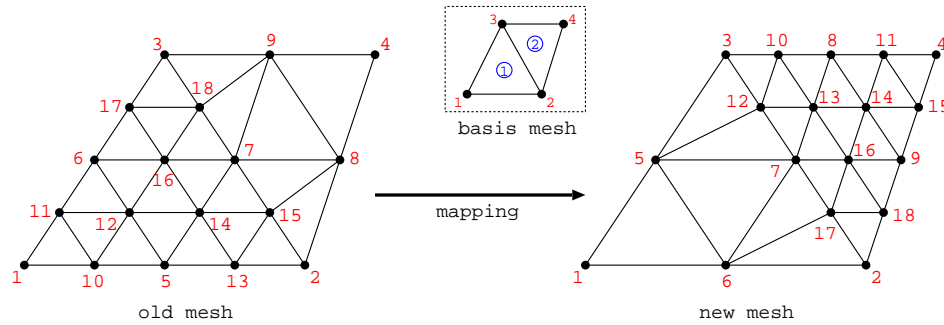
Figure 8.9: *Transition from one mesh to another. Due to the way the meshes are constructed, the number of nodes and the number of interpolations is minimal.*

At this stage, it is really important to note that the numbering of the internal nodes in the new mesh can be completely different from the numbering of the internal nodes of the old mesh, even though it geometrically concerns the same nodes. This of course is a direct consequence of the possible differences in the assigned LOR of each basis element for each mesh at each time level. It only requires one basis element with a different LOR than before to completely alter the order in which the added nodes are numbered. The essential link between the node numbers of the internal nodes of the old and new mesh is obtained via arrays *intnodesold* and *intnodesnew*.

The mapping of the data to the internal nodes of the second basis element is slightly more complicated. In the same way as for element '1', first the nodes are mapped that are contained in both the new as well as the old mesh. In case of our example, this concerns nodes '7' to '9'. Surely, the pos-

sible difference in numbering between the two meshes, which follows from comparing the corresponding entries in arrays *intnodesold* and *intnodesnew*, is taken into account.

Next, the remaining internal nodes of the newly refined second basis element are mapped by means of (linear) interpolation. In order to determine the correct node numbers of the parent nodes, array *parentnodes* is used. Some caution is advised, in particular when the difference in LOR between the old and the new mesh is larger than one, because the order in which the nodes are interpolated then becomes important. This is the reason why the node numbers of the internal nodes are stored in sequence of increasing LOR in auxiliary array *intnodes*.

8.4.4   Adaptation of the time step

The performance of both the numerical scheme and the local refinement code is affected by the size of the time step. Clearly, the time step should not be chosen too large, because this can lead to instability of the numerical scheme (for instance in case an explicit time integration method is used) or it could affect the resolution of physical phenomena. Setting the time step to too small a value is mostly impractical and often unnecessary. Therefore, even though the choice of the initial time step is reasonable, it is important to include some means of time step control into the code.

In case divergence of the iterative solver is detected, a sound approach is to attempt to solve the governing equation again after the time step has been halved and the time level has been reset to a previous time instance. Of course, one cannot halve the time step indefinitely. Therefore, the maximum number of refinements is set to be equal to 16. If the time step has become too small, the computation is terminated.

If the (initial) time step is too large, a situation can arise in which (part of) the moving interface has advanced to elements having a lower LOR than the elements that were previously intersected. Inevitably, this results in a loss of information and thus reduces the accuracy of the numerical solution. This so-called *interface outside refinement* problem is addressed next.

8.4.5   Interface outside refinement

At any given moment during a computation, a situation may arise in which the mesh, and possibly the time step, are to be adapted. If for instance the time step is relatively large, a moving interface might advance outside the band of refinement. Another possibility is that a new interface is created due to a source term or a change in boundary conditions. In any of these circumstances, proper actions need to be taken to limit any possible loss of accuracy.
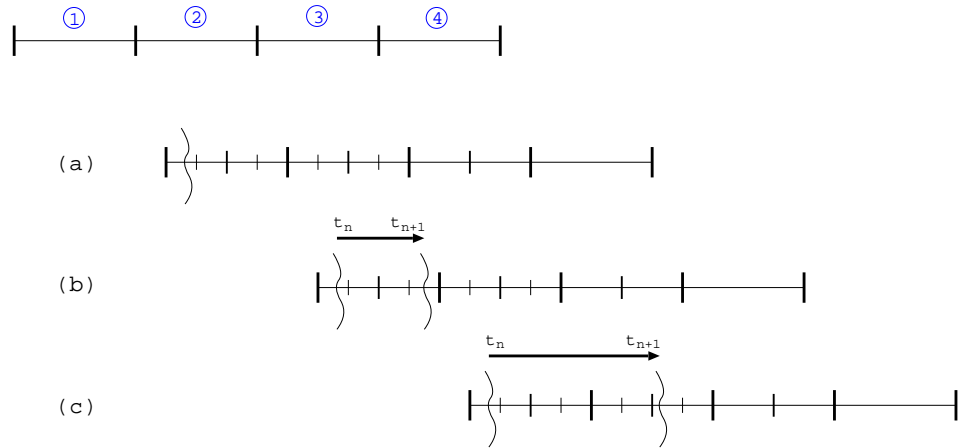
Figure 8.10: *Basic interface progression. (a) Initial interface position. (b) The moving interface remains within the same basis element. (c) The moving interface advances to a neighboring basis element with equal LOR.*

Consider the solution to a moving boundary problem at time level $t = t_n$, on a refined grid as shown in Figure 8.10a. Next, the numerical solution at time level $t_{n+1} = t + \Delta t$ is computed on the given grid. In case the obtained solution at $t = t_{n+1}$ is such that the moving interface remained within the same basis element as before (and no new interface has appeared), as shown in Figure 8.10b, neither the mesh nor the time step need to be modified. If the moving interface advances to a neighboring basis element which has an equal LOR as the previously intersected basis element, a local re-meshing is sufficient (Figure 8.10c).

However, in any of the following three instances, illustrated in Figure 8.11, a more strategic approach is required:

- the moving interface advances to a basis element which has a lower LOR than before (either still within the band of refinement, or worse, outside the band of refinement)

- the moving interface remains in a basis element which has the same LOR as before, but a new interface has appeared in a basis element with a lower LOR

- the moving interface advances to a basis element which has a lower LOR than before and a new interface has appeared in a basis element with a lower LOR

Each of the above 'interface outside refinement' situations can easily be detected. All that is required is a comparison of the (at most) N_{basis} entries of the arrays *refineold* and *refinenew*. As soon as an entry of array *refinenew* contains a value equal to $\text{LOR}_{max} + 1$ (which indicates that this particular

basis element is now intersected by a moving interface, see Section 8.4.1), while the corresponding entry in array *refineold* contains a lower value, the search is terminated, and an 'interface outside refinement' warning is given.

Although an 'interface outside refinement' situation is easily detected, it is far from trivial to determine whether its cause is an advancing or a newly created moving front. Indeed, a means of keeping track of existing front positions, in combination with estimates of the front velocity field, could probably be implemented. However, this will most likely be rather costly.

Another problem is that in either situation, preferably, different actions have to be taken. In case of an existing front, a good strategy is to halve the time step and then to retry to solve the governing equation on the existing mesh, in order to keep the number of elements (and thus the number of unknowns) limited. If a new front appears, there is no real need to modify the time step. But, in order to resolve the new interface position at the highest resolution possible, a local re-meshing is required. Of course, in either case, the time level is to be reset to the previous time instance.

At first glance, a reasonable strategy might seem to just perform both a re-meshing and a time step reduction, whenever an 'interface outside refinement' situation is detected. In this way, the level of accuracy is sustained, although at a fairly high price: an increase in both the number of unknowns as well as the number of time steps to be taken.

Unfortunately, besides the increase in costs, there is another drawback to this strategy. For instance, assume that due to a source term a new moving interface appears in a previously unrefined mesh, see Figure 8.12. If we now proceed according to the above strategy, we reduce the time step, reset the time level to the previous time instance, perform a re-meshing and solve the governing equation on the now locally refined mesh.

As a result of the higher resolution of the mesh, and the smaller time step, it is not unlikely that at this new time instance, we find a solution for which a front does not yet appear. Since there no longer exists a moving front, it is then determined that a local mesh refinement is not needed. The mesh is once more coarsened and the governing equation is again solved on the coarsest grid. And so, once again a new front is detected, etc. In the worst case, this process of repeatedly refining and coarsening might even cause the computation to be terminated because the time step is reduced too often.

Hypothetically, an appropriate remedy to this problem is to always maintain the local refinement for at least two or three consecutive time steps and not to reduce the time step. If during these successive time steps new modifications to the mesh are required, the desired refinement can be obtained by combining arrays *refinenew* and *refineold*. A modified array refinenew is then constructed by setting each entry of the new array refinenew equal to the maximum value of the old refinenew and the corresponding value of array refineold.
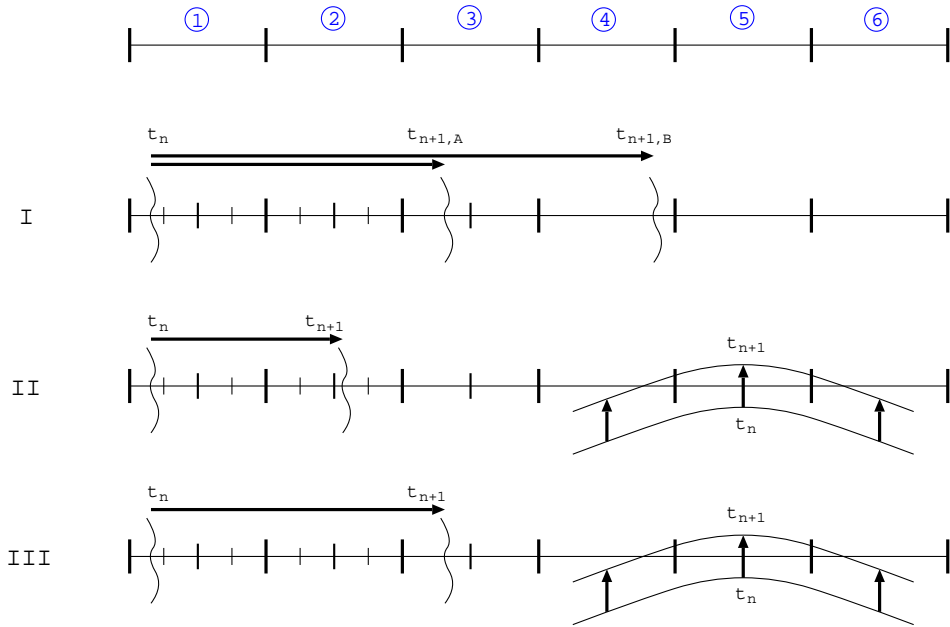
Figure 8.11: *More complicated interface progression. (I) The moving interface advances to an element A) within the band of refinement; B) outside the band of refinement. (II)/(III) Besides an advancing existing front, a new interface appears (for instance due to a source).*

However, although in this example it is clear that we are dealing with a new interface and not an advancing front, recall that in general this distinction is not easily made. The problem with this remedy lies in the time step, which is not reduced. If, for instance, we have a moving front as sketched in Figure 8.12, that has advanced considerably within one time step, say, outside the band of refinement, it definitely not suffices to simply perform a local refinement and not to reduce the time step. The reason is that in this way physical phenomena, such as the influence of latent heat, are not properly resolved.

At this point, it can be concluded that more information is needed in order to derive a generally applicable strategy. Luckily, for our melting problem, this additional piece of information follows from a basic observation: whenever a moving interface skips one or more elements during a single time step, this automatically means that these skipped elements have undergone a full phase transition. That is, they either went from being fully solid to fully liquid, or vice versa.

Thus, one final array is added to the set of auxiliary arrays. This array, called *phasenew* or *phaseold*, depending on which mesh it refers to, has a length equal to the number of elements of the current mesh, and each of its entries is assigned an integer value corresponding to the phase of the associated element. For instance, if an element is fully solid, the position in
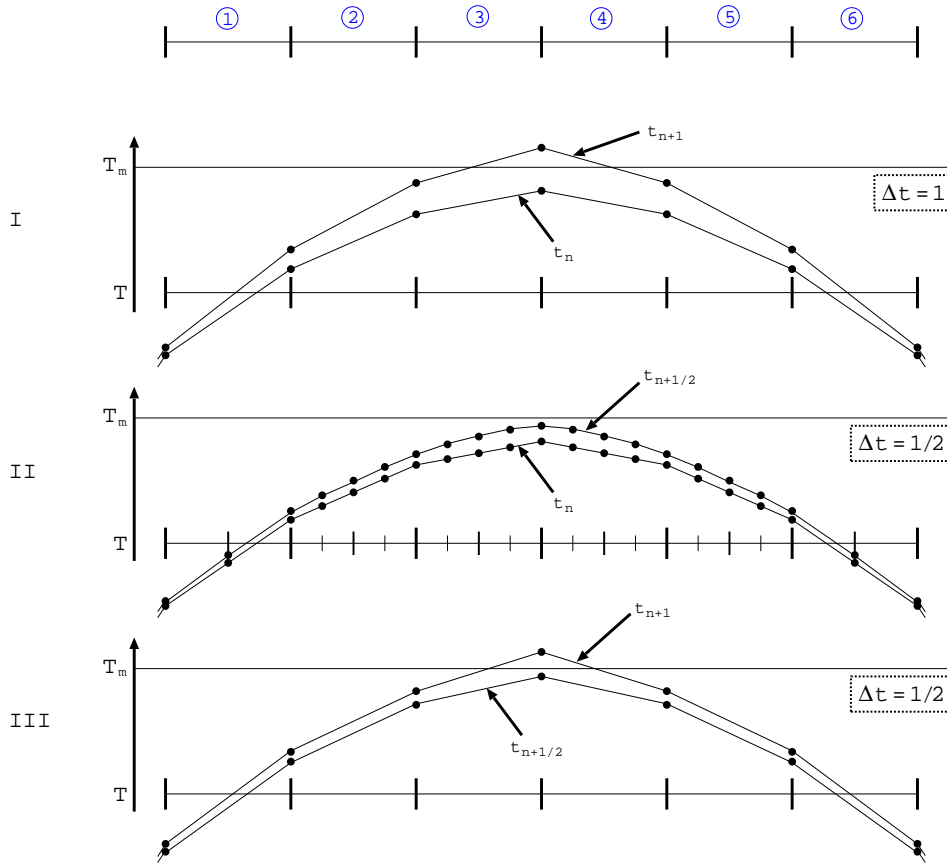
Figure 8.12: *Inefficient resolution of a source induced interface. (I) A moving interface is detected at $t = t_{n+1} = t_n + \Delta t$. (II) The time step Δt is halved and the time level is reset to the previous time instance t_n. The mesh is refined and the numerical solution is computed for $t = t_{n+1/2}$. (III) Because no moving interface is detected, the mesh is coarsened and the numerical solution is computed for $t = t_{n+1}$.*

the array is assigned a value of '0', if the element is fully liquid it contains the value '1'. Otherwise, its value is set to '2'. In order to detect whether at least one element skipped its phase transition, all that is needed is a one-on-one comparison of the entries of arrays *phasenew* and *phaseold*.

The general refinement strategy to deal with 'interface outside refinement' situations (which is also applicable to moving boundaries initiated by Dirichlet boundary conditions at $t = t_0$), is given by Algorithm 6.

8.5 Conclusions

In this chapter a local refinement code has been described which is capable of accurately resolving changes in the geometry or the displacements of a moving interface, while preserving the quality of the basis mesh. The data

---

Algorithm 6: Interface outside refinement procedure.

---

1 solve governing equation on current grid
2 **if** *element skipped phase transition* **then**
3 | reduce time step

4 **if** *interface outside refinement* **then**
5 | combine refineold and refinenew
6 | refine mesh

7 **if** *element skipped transition or interface outside refinement* **then**
8 | reset time and data to previous time level

---

structure developed, and the implementation of the local refinement in the Sepran package, are both efficient and easily understood.

A good strategy for refining the mesh is to always start constructing the new mesh from the basis mesh onward. The intersected elements, as well as the direct neighboring ones, are preferable assigned the highest LOR, while the remaining elements are assigned an LOR which gradually reduces with the distance from the intersected elements. The actual construction of the refined mesh proceeds by first performing a single refinement of all basis elements that are assigned to be refined at least once, then to refine all elements that are assigned an LOR of at least two, etc. In this way, the number of interpolations of the data field are kept at a minimum.

With respect to the basis mesh it is important that the coarseness is such that for a smooth solution an acceptable accuracy is guaranteed. If not, there is no use in refining the mesh locally.

In case solving the governing equation fails within a given maximum number of iterations, a new attempt can be made with a reduced time step. Of course, the number of reductions of the time step is to be limited to a reasonable number of times. If for several successive time steps the time step is not reduced, it can be attempted to increase the time step.

To ensure that physical phenomena are properly resolved, it is always first checked whether an element did not skip its phase transition. If an element indeed underwent a full change of phase, the time step is reduced. Whenever a moving interface advances to elements that are assigned a LOR that is lower than LOR_{max}, or when a new interface appears, an 'interface outside refinement' situation is created. The mesh is then locally refined. Finally, in case either an element skipped its phase transition and/or an 'interface outside refinement' situation has occurred, the time level is reset to the previous time instance, and the governing equation is solved anew under the modified conditions.

CHAPTER 9

Numerical results

The enthalpy and the temperature approach, discussed in Section 6.3 and Chapter 7, respectively, have both been proposed as numerical resolution methods to solve our two-phase Stefan problem, introduced in Chapter 3, that describes the melting component of the mark formation process. The focus of the first part of this chapter will be on the differences in performance of these approaches. In particular, it will be shown that for the current application, the temperature approach is preferred over the enthalpy approach.

The second part of this chapter concentrates on some characteristic properties of the temperature approach. Of special interest are the inclusion of an artificial mushy region, as introduced in Section 7.4, and the application of the local adaptive mesh refinement discussed in Chapter 8.

In the remainder of this chapter, results are presented for the application of the melting model to DVD and Blu-ray recording configurations.

9.1 Introduction

Throughout the first part of this chapter, the emphasis will be on the 'performance' of certain numerical methods. But before a judgment can be made on how well a method performs, it is worthwhile to define the criteria on which to base our assessment.

Since the temperature T is the quantity of interest for our melting model, it is important to know how accurate the approximated temperature actually is. To this end, the numerical solution is compared to a reference solution T_{ref}, which is either a known similarity solution or a numerically obtained solution on a very fine grid. The error in the approximated solution T is

measured as

$$\text{Err}_{i,j} = \frac{\|T_{\text{ref}} - T\|_i}{\|T_{\text{ref}}\|_i} \times 100\%. \tag{9.1}$$

The type of norm that is used to measure the error is indicated by the subscript i. Both the 2-norm ($i = 2$) and ∞-norm ($i = \infty$) will be considered. The second subscript j is used to distinguish between either the temperature as a function of position ($j = x$) and the temperature as function of time ($j = t$). Errors are always evaluated for $t = t_{\text{end}}$, and, when applicable, at a prescribed position.

Other interesting quantities include the total time taken to complete a computation, the total number of (pseudo) Newton iterations, and the average number of iterations per time step. In tables, the abbreviation '*#iters*' is used to indicate the average number of Newton iterations. In case the time step size is adapted at least once during a computation, the total number of time steps taken at the end of the computation is given within brackets.

Unless indicated otherwise, time is in seconds, and all temperatures are given in 10^3 °C, except for Section 9.2, where temperatures are given in °C.

9.2 Comparison: Fachinotti vs Nedjar

The performance of the Nedjar method and the Fachinotti scheme has been evaluated using three test cases. The first two test cases consider the melting of a 1D line segment, and are taken from Chun and Park [16]. The third test problem considers the melting of a 2D square region, which consists of a phase-change material, and is embedded on two sides by a second, non-melting material.

Since we are comparing two numerical methods that are essentially quite different, it is appropriate to first address the validity of the comparison.

9.2.1 Validity of the comparison

In the method of Nedjar we solve a linear system for the temperature update ΔT. In the Fachinotti method, we solve a nonlinear system for T^{m+1}. Both systems are solved iteratively, but the stopping criterion for each is different. The Fachinotti method is said to have converged when $\|\Psi(T_i^{m+1})\|_\infty < \epsilon \|\Psi(T^m)\|_\infty$, where ϵ is taken to be equal to 10^{-6}. The method of Nedjar is said to have converged when $\|\Delta T_i\|_\infty < \epsilon$, and corresponding results are presented in this section. The reason for this choice of stopping criterion for the Nedjar method is that results for using absolute criterion $\|\Delta T_i\|_\infty < \epsilon \|\Delta T_0\|_\infty$ are found to be equal up to the third or higher significant digits. However, slightly more iterations (and thus more time) are required.

Although the solution methods and their corresponding stopping criterion are essentially different, we believe that the comparison presented in

this section is valid. The reason is that for the given value of ϵ, the computed errors with respect to the similarity solution, in both the 2-norm and ∞-norm, are of the same order of magnitude. This argument holds for the temperature as function of time as well as position. In particular, it holds for the test case where the physical parameters in for both phases are equal, most likely because the temperatures are of the order of one. For the test case 'unequal' the errors of the Fachinotti method are even less, for the given tolerance ϵ, which supports why the Fachinotti method is to be preferred.

The reason for choosing the ∞-norm for the measures used in the stopping criteria is that for melting problems in composite domains, this choice of norm ensures that the solution method converges up to desired accuracy level, in those regions where the actual melting occurs. In particular when these regions are small with respect to the computational domain, the use of the 2-norm would negatively affect the accuracy of the solution, because of too much averaging of the error.

9.2.2 Test case 1: 'equal'

In this first 1D test problem, the thermal properties for the liquid and the solid phase are taken constant, and equal for both phases. The thermal conductivity $\kappa = 2$ W/m°C, $c = 2.5 \times 10^6$ J/kg°C and density $\rho = 1$ kg/m^3. The latent heat $L = 10^8$ J/kg. The initial temperature at $t = 0$ of the whole domain is 2 °C, the melting temperature $T_m = 0$ °C. On one end, a Dirichlet boundary condition is imposed, $T = -4$ °C, and on the other end we have the insulation condition $\partial T / \partial t = 0$. The time step size is kept fixed at $\Delta t = 21600$ s (6 hours) and the computation ends at $t = t_{\text{end}} = 2.592.000$ s (30 days).

The computations for the original test case are performed on a spatial grid consisting of 100 elements, with $\Delta x = 0.1$ m. The temperature as a function of time for both methods is plotted in Figure 9.1. Notice that the solution, as computed using the method by Nedjar, clearly shows 'staircasing', which is characteristic for enthalpy methods. The temperature method exhibits a similar type of behavior.

Results with respect to a global refinement of the spatial grid are listed in Table 9.1. A benefit of this test case, as well a test case 2, is the existence of a corresponding similarity solution [16], which is used to estimate the errors in the approximated solution. The table clearly shows that in general the error for the temperature as a function of time (Err$_{,t}$, evaluated at a fixed node located at $x = 0.3$ m) is about ten times larger (in both norms) than the error for the temperature as a function of position (Err$_{,x}$). In addition, the reduction of the errors is linear when the spatial grid size is doubled, as expected. Also, note that for the Nedjar method for $n = 400$ too low a value is found for the interface position x_m, as a result of wiggles.
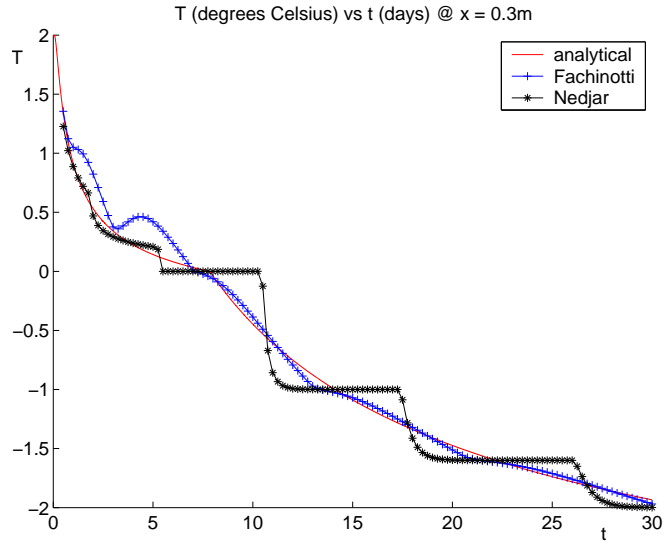
Figure 9.1: *Test case 1: 'equal'. Difference between Nedjar and Fachinotti for the temperature as function of time in a point $x = 0.3$ m. $n = 100$, $\epsilon = 10^{-6}$.*

Table 9.1: *Test case 1: 'equal'. The effect of a global refinement of the spatial grid. The 'exact' position of the moving interface at $t = t_{\mathrm{end}}$ is $x_m = 0.587$.*

	n	time	#iters	x_m	$\mathrm{Err}_{2,t}$	$\mathrm{Err}_{\infty,t}$	$\mathrm{Err}_{2,x}$	$\mathrm{Err}_{\infty,x}$
Fachinotti	100	10	3.2	0.601	8.1	17	1.3	1.7
	200	10	3.5	0.593	4.2	7.1	0.67	0.98
	400	13	4.0	0.589	2.2	3.6	0.38	0.76
	800	18	4.6	0.587	1.3	2.1	0.15	0.19
Nedjar	100	12	28	0.600	12	25	0.89	2.2
(NC)	200	18	55	0.600	5.5	13	0.60	2.0
	400	44	116	0.575	2.6	8.0	0.43	1.8
	800	91	137	0.594	1.9	3.1	0.22	0.70
Nedjar	100	17	79	0.621	11	18	1.5	1.9
(Gauss)	200	32	143	0.589	5.2	8.6	0.72	1.2
	400	54	144	0.607	2.8	6.5	0.36	0.69
	800	84	122	0.581	2.3	4.4	0.35	1.4

9.2.3 Test case 2: 'unequal'

For the second 1D test case, the values of κ and c are taken to be constant, but different for each phase. The thermal properties are: $\kappa_s = 2.22$ W/m°C, $\kappa_l = 0.556$ W/m°C, $c_s = 1.762 \times 10^6$ J/kg°C, $c_l = 4.226 \times 10^6$ J/kg°C, $L = 3.38 \times 10^8$ J/kg, and $\rho = \rho_s = \rho_l = 1$ kg/m^3. On the whole domain the initial

temperature is now 10 °C, while the melting temperature is once more set to be $T_m = 0$ °C. The temperature at the left boundary is kept at -20 °C, the right end is again insulated. Although t_{end} is also set to 30 days, a smaller time step size is taken: $\Delta t = 2000$ s.

The results obtained for this second test case are listed in Table 9.2. In comparison to the previous test problem, the overall performance of both methods is comparable. Remark that for both test cases, it holds that the computational load, expressed by the average number of (pseudo)-Newton iterations and the total computational time, for the Nedjar method scales with the increase of the number of elements. For the temperature based method, the computational load hardly increases when the mesh is globally refined.

An interesting observation can be made from Table 9.3, in which the performance of both methods is compared for varying Stefan numbers $St = \rho c_l (T_0 - T_m)/L$, where ρc_l is the heat capacity of the liquid phase and T_0 the ambient temperature. For problems for which the melting front moves very rapidly, i.e., the Stefan number $St \approx O(10^2)$, the enthalpy based method seems to be the method of choice. However, for the phase-change materials that are used in optical rewritable recording, a Stefan number of $O(1)$ is commonly found. These problems can best be resolved using the method of Fachinotti.

Table 9.2: *Test case 2: 'unequal'. The effect of a global refinement of the spatial grid. The 'exact' position of the moving interface at $t = t_{end}$ is $x_m = 0.742$.*

	n	time	#iters	x_m	$Err_{2,t}$	$Err_{\infty,t}$	$Err_{2,x}$	$Err_{\infty,x}$
Fachinotti	100	102	3.0	0.748	2.1	6.0	0.49	1.4
	200	110	3.1	0.744	0.88	3.2	0.15	0.39
	400	128	3.5	0.743	0.41	1.6	0.08	0.25
	800	171	4.0	0.743	0.20	0.75	0.04	0.19
Nedjar	100	107	11	0.700	11	30	0.98	2.1
(NC)	200	131	19	0.750	4.7	18	0.56	2.0
	400	223	36	0.725	2.0	9.4	0.31	1.4
	800	564	72	0.738	0.85	5.3	0.06	0.64
Nedjar	100	152	54	0.721	5.4	15	1.2	2.7
(Gauss)	200	244	80	0.682	2.4	9.0	0.22	0.68
	400	572	139	0.745	1.4	8.5	0.14	0.34
	800	1831	264	0.737	1.0	4.1	0.16	0.72
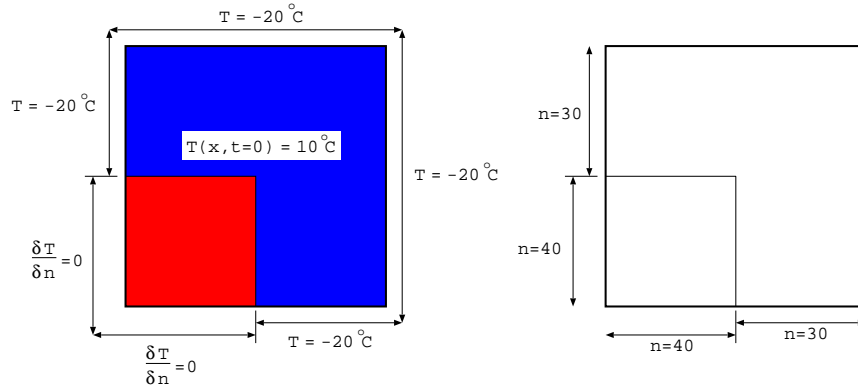
Figure 9.2: *Test case 3: '2D corner'. Initial and boundary conditions (left). Number of grid points used (right).*

9.2.4   Test case 3: '2D corner'

The third test problem considers the melting of a square region, occupied by the same material as that of test case 2: 'unequal', which is on two sides enclosed by a non-melting material, see Figure 9.2. For the embedding material, $\rho = 1$ kg/m^3, $c = 10^6$ J/kg°C, $\kappa = 0.5$ W/m°C, $L = 2 \times 10^4$ J/kg and $T_m = 20$ °C.

Table 9.4 shows that the computational demand of the Fachinotti method does not increase as rapidly for smaller values of the tolerance ϵ then that of the Nedjar method. This is caused by the damping factor μ in the pseudo Newton iteration process.

In Figure 9.3, contour levels are plotted of the temperature within the composite domain. The figure illustrates the difference in the captured interface position. Although the moving interface, represented by contour level 5, is very smooth when using the temperature approach, Nedjar clearly shows oscillations.

Table 9.3: *Test case 2: 'unequal'. Performance with respect to Stefan number St, $\epsilon = 10^{-3}$, $\Delta t = 2000$ s, $n = 800$, $t_{\text{end}} = 20$ days.*

		Stefan number St			
		$\approx 5 \times 10^{-4}$	$\approx 5 \times 10^{-2}$	$\approx 5 \times 10^{0}$	$\approx 5 \times 10^{2}$
total #iters	Fachinotti	2322	2829	4957	6603
	Nedjar	78947	43045	14396	6271
total time	Fachinotti	23	29	45	58
	Nedjar	355	195	132	32
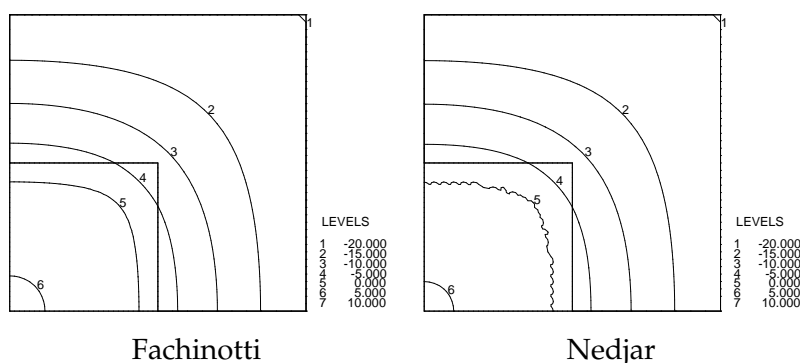
Fachinotti   Nedjar

Figure 9.3: *Test case 3: '2D corner'. Fachinotti: no wiggles; Nedjar: wiggles.* $\epsilon = 10^{-3}$, $\Delta t = 2000$ s, $t_{end} = 20$ days.

9.2.5   Nedjar: Newton-Cotes vs Gauss rule

The results shown for the above test cases have all been obtained using first order Newton-Cotes integration. As such, the plot of the solution for test case 'equal', i.e., Figure 9.1, for the original mesh size ($n = 100$), is found to be equal to results presented by, for instance, Chun and Park [16]. However, the solution obtained on the same grid using a 3-points Gauss rule, has quite a different shape, see Figure 9.4.

Because of the observed difference, the computations for the various grid spacings have been performed anew for test cases 1 and 2, using Gauss integration. The results obtained are also listed in Tables 9.1 and 9.2. When compared to the results that are found using Newton-Cotes integration, it can be concluded that in general, the use of a Gauss rule is much more costly: both the average number of iterations as well as the total time are (much) higher. With respect to the level of accuracy, not much difference between both integration rules can be discerned.

Table 9.4: *Test case 3: '2D corner'. Computational load for varying tolerance ϵ:* $\Delta t = 2000$ s, $t_{end} = 20$ days.

		$\epsilon = 10^{-6}$	$\epsilon = 10^{-4}$	$\epsilon = 10^{-2}$
total #iters	Fachinotti	3376	2599	1734
	Nedjar	88964	46020	10107
total time	Fachinotti	208	166	116
	Nedjar	2030	1093	266
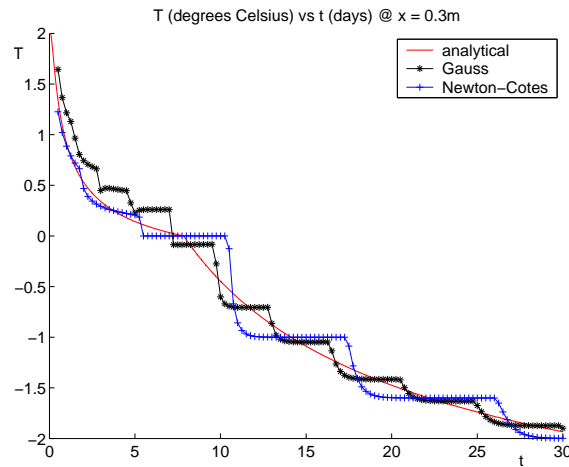
Figure 9.4: *Test case 1: 'equal'. Influence of the choice of integration rule for the Nedjar method on the temperature as function of time in a point $x = 0.3$ m. $n = 100$, $\epsilon = 10^{-6}$.*

9.2.6   Conclusions

Based on the results, the temperature based method seems to be the method of choice for small and medium range Stefan numbers. Not only can it easily be integrated into existing finite element codes for diffusion problems in composite domains, it also outperforms the enthalpy based method with respect to accuracy, stability and computational load. For melting problems with Stefan number of $O(10^2)$ or larger, the enthalpy method might be the better choice.

With respect to spatial integration, the use of first order Newton-Cotes is preferred over the use of a 3-point Gauss rule.

9.3   Temperature approach

In this section some characteristics of the Fachinotti method are studied in more detail. Numerical results will be discussed concerning the introduction of an artificial mushy region and the application of adaptive local refinement of the computational grid.

9.3.1   Line search

In Section 7.3 it is explained how convergence of the Newton-Raphson method can be improved, by means a line searching algorithm. Of particular interest is the order of the polynomial that approximates the function $g(\alpha)$ as defined in (7.26), and which is used to determine the linesearch parameter α. In practice, the use of a linear polynomial sometimes leads to

non-convergence of the Newton scheme. No noticeable difference in performance can be discerned when using either a cubic or quadratic polynomial. Since the cubic approximation is slightly more costly, the use of a quadratic approximation polynomial is preferred.

9.3.2 Artificial mushy region

In Section 7.4, it has been explained that the isothermal approach fails in case a source is added to the problem formulation. This drawback can be overcome by means of an artificial mushy region. A pivotal parameter in this is the width of the mushy zone T_Δ. In this section, we will limit our study to 1D problems. The source functions that are used in the experiments are listed in Table 9.5.

The physical parameters of the test problems considered are taken such that they resemble the values used in simulations of the recording of a DVD [52]. The values for these parameters are: $\kappa_s = \kappa_l = 0.006$, $c_s = c_l = 12.85$, $L = 6400$ and $T_m = 620$. (These values are scaled to be used in the computer code, and therefore can differ from those in Reference [52]). At $t = 0$, the whole domain [-1, 1] is at a temperature of $0\,°C$, thus solid, and the boundaries are taken to be adiabatic. For this configuration, the reference solutions, corresponding to the four source functions from Table 9.5, are plotted in Figure 9.5 at selected time instances between $t = 0$ and $t = t_{end} = 100$.

In case of isothermal problems that are driven by a non-zero source term, the mushy parameter T_Δ is preferably chosen such that the solution to the regularized problem resembles the isothermal solution as much as possible. In order to get a good impression on how to choose T_Δ, a parameter study has been performed, of which the results are listed in Table 9.6. In this table, as in future tables, x_m denotes the leftmost point at which the moving interface intersects the melting temperature. For the 'exact' values of x_m and the maximum temperature T_{max} at $t = t_{end}$ we refer to Table 9.5.

An interesting observation that can be made from Table 9.6 is that the approximated solutions are in general rather accurate (the errors are less

Table 9.5: *Definitions of the various source distributions and values for the position of the leftmost moving interface and the maximum temperature ($\sigma = 1/\sqrt{2\pi}$).*

	actual function ($A = 3.5 \cdot 10^2$)	x_m	T_{max}
exp2	$A \exp\left(-\frac{1}{2}x^2/\sigma^2\right)$	0.58890	1.96416
exp4	$A \exp\left(-\frac{1}{2}x^2/\sigma^4\right)$	0.25950	1.38633
2exp4	$A \left[\exp\left(-\frac{1}{2}(x - \frac{1}{4})^2/\sigma^4\right) + \exp\left(-\frac{1}{2}(x + \frac{1}{4})^2/\sigma^4\right)\right]$	0.51344	1.61716
const	A	X	2.22568
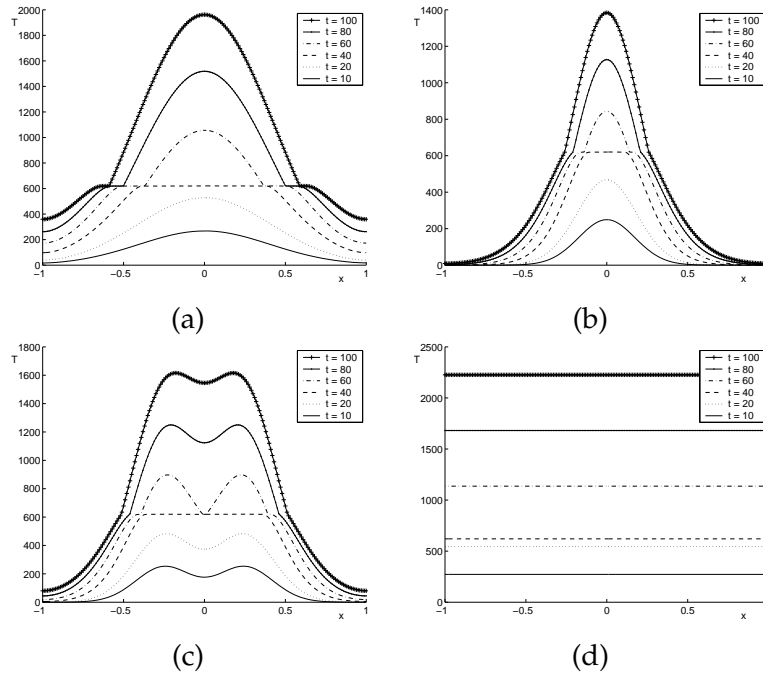
Figure 9.5: *Reference solutions T_{ref}. (a) exp2, (b) exp4, (c) 2exp4, (d) const. (For definitions, see Table 9.5). The melting temperature $T_m = 620\,^\circ$C.*

than 1% in both norms). Furthermore, the mushy parameter T_Δ can be taken surprisingly large, without much loss of accuracy. It seems that the shape of the source function plays an important role in the performance of the method: in case of multiple appearing fronts (2exp4) or functions with steep gradients near the front (exp2), the performance of the temperature method is affected more for smaller values of T_Δ, than in case the other source functions are applied. It can be concluded that $T_\Delta = 0.1\%$ of T_m is a save choice for most problems.

In the previous test, the threshold parameter ϵ, which is used in the stopping criterion for the Newton scheme, has been kept exceptionally small ($\epsilon = 10^{-6}$). In Table 9.7 results are listed on the performance for increasing values of ϵ. The mushy parameter T_Δ is taken to be equal to 0.1% of T_m. From the table it follows that for values of ϵ smaller than 10^{-2}, the gain in accuracy becomes negligible. Therefore, a value of 10^{-3} is a reasonable choice for parameter ϵ.

In case both ϵ and T_Δ are kept fixed, it is interesting to see how the performance is affected when the spatial and the time grid are globally refined simultaneously. From Table 9.8 it can be concluded that the reduction of the error of the approximated solution is linear with respect to halving both the time step and the grid spacing. As expected, the total amount of time required for the computation also scales accordingly. The average

number of Newton iterations is almost constant for each source function. The same effect on the performance is observed for the Nedjar method, see Table 9.9. Not surprisingly, after our comparison made in Section 9.2, the enthalpy approach shows to be computationally more demanding and less accurate.

Table 9.6: *The effect of varying the mushy parameter T_Δ (in % of the melting temperature T_m). $\Delta t = 1$ s, $n = 100$, $\epsilon = 10^{-6}$.*

	T_Δ	time	#iters	x_m	$\text{Err}_{2,x}$	$\text{Err}_{\infty,x}$	$T_{\max}$
exp2	10	7.8	2.4	0.602	1.1	1.9	1.96018
	0.1	8.3	4.7	0.595	0.12	0.32	1.96236
	0.001	11	9.9 (102)	0.621	0.12	0.34	1.96242
exp4	10	7.8	2.7	0.263	0.74	0.73	1.37975
	0.1	8.4	3.9	0.261	0.28	0.26	1.38267
	0.001	8.5	4.9	0.261	0.28	0.27	1.38265
2exp4	10	7.9	2.8	0.518	0.42	0.51	1.61298
	0.1	8.3	4.7	0.516	0.17	0.23	1.61520
	0.001	10	7.4	0.516	0.17	0.23	1.61522
const	10	7.5	1.0	X	0	0	2.22568
	0.1	7.5	1.2	X	0	0	2.22568
	0.001	7.6	1.2	X	0	0	2.22568

Table 9.7: *The effect of varying ϵ. $\Delta t = 1$ s, $n = 100$, $T_\Delta = 0.1\%$ of T_m.*

	ϵ	time	#iters	x_m	$\text{Err}_{2,x}$	$\text{Err}_{\infty,x}$	$T_{\max}$
exp2	10^{-4}	8.5	5.2	0.595	0.12	0.32	1.96236
	10^{-2}	8.2	4.2	0.595	0.12	0.32	1.96234
	10^{-1}	8.0	3.2	0.596	0.20	0.32	1.96106
exp4	10^{-4}	8.0	3.4	0.261	0.28	0.26	1.38267
	10^{-2}	7.8	2.7	0.261	0.29	0.28	1.38246
	10^{-1}	7.8	2.2	0.260	0.49	0.44	1.38031
2exp4	10^{-4}	8.3	4.1	0.516	0.17	0.23	1.61520
	10^{-2}	8.1	3.5	0.516	0.17	0.24	1.61521
	10^{-1}	7.9	2.9	0.515	0.29	0.33	1.61403
const	10^{-4}	7.5	1.2	X	0	0	2.22568
	10^{-2}	7.5	1.2	X	0	0	2.22568
	10^{-1}	7.5	1.2	X	0.05	0.05	2.22686

One might wonder to what extent the latent heat affects the maximum value of the temperature distribution when compared to the same problem, but with no latent heat. For the given parameters, this difference appears to be of the order of 20%, see Table 9.10.

Table 9.8: *Fachinotti: the effect of varying the time step size Δt and number of elements n.* $T_\Delta = 0.1\%$ *of* T_m, $\epsilon = 10^{-3}$.

	Δt	n	time	#iters	x_m	$\text{Err}_{2,x}$	$\text{Err}_{\infty,x}$	$T_{\max}$
exp2	1	100	8.4	4.7	0.595	0.12	0.32	1.96236
	0.5	200	18	4.0	0.590	0.05	0.14	1.96320
	0.25	400	42	3.6	0.590	0.03	0.10	1.96367
exp4	1	100	7.9	3.1	0.261	0.28	0.26	1.38266
	0.5	200	17	2.9	0.260	0.14	0.15	1.38450
	0.25	400	39	3.0	0.260	0.06	0.07	1.38549
2exp4	1	100	8.2	3.9	0.516	0.17	0.23	1.61519
	0.5	200	18	3.8	0.515	0.09	0.19	1.61613
	0.25	400	42	3.3	0.514	0.04	0.05	1.61664
const	1	100	7.6	1.2	X	0	0	2.22568
	0.5	200	16	1.0	X	0	0	2.22568
	0.25	400	34	1.1	X	0	0	2.22568

Table 9.9: *Nedjar (Gauss-rule): the effect of varying the time step size Δt and number of elements n.* $\epsilon = 10^{-3}$.

	Δt	n	time	#iters	x_m	$\text{Err}_{2,x}$	$\text{Err}_{\infty,x}$	$T_{\max}$
exp2	1	100	11	31	0.638	0.12	0.34	1.96239
	0.5	200	28	32	0.635	0.06	0.15	1.96323
	0.25	400	69	25	0.631	0.04	0.12	1.96370
exp4	1	100	9.4	23	0.264	0.38	0.84	1.38265
	0.5	200	23	24	0.262	0.16	0.41	1.38448
	0.25	400	54	17	0.259	0.09	0.26	1.38542
2exp4	1	100	9.9	25	0.516	0.16	0.28	1.61518
	0.5	200	25	29	0.513	0.12	0.42	1.61613
	0.25	400	58	22	0.515	0.06	0.26	1.61665
const	1	100	8.5	29	X	0	0	2.22568
	0.5	200	20	37	X	0	0	2.22568
	0.25	400	47	34	X	0	0	2.22568

9.4 Adaptive local mesh refinement

The performance of the adaptive local mesh refinement code, discussed in Chapter 8, has been evaluated using the test cases from Section 9.2. The results for test cases 1 and 2 can be found in Tables 9.11 and 9.12. The number of elements of the basis mesh is taken to be $n = 100$. In the tables, LOR denotes the maximum level of refinement assigned to the basis elements intersected by the moving interface. Since $n = 100$ for the basis mesh, an LOR = 2 means that locally, the grid spacing is the same as for a non-refined mesh for which $n = 400$. The maximum number of elements used during the computation is denoted by n_{max}.

Consider the errors as listed in Tables 9.11 and 9.12, and compare them with the values as listed for the Fachinotti method in Tables 9.1 and 9.2, respectively. The level of accuracy, obtained using an LOR = 3, is found to be almost equal to that acquired on a mesh consisting of 800 elements, as expected. The same holds for the other levels of refinement. The total number of time steps required increases slightly in some cases (as a result of time step size reductions), but there is a noticeable gain in computational time. The effect of the mesh refinement for a basis mesh of 100 elements and an LOR = 3 is illustrated in Figure 9.6.

In Figure 9.7 the adaptive space-time refinement procedure is illustrated, based on test case 3. In this example, the initial time step size of 40.000 seconds has been exaggerated with respect to that of the reference problem (2.000 seconds), in order to suit our purpose. The problem is driven by a Dirichlet boundary condition, imposed on the outer fixed boundary, such that at $t = 0$ a moving interface will appear, see Figure 9.7a. When the presence of the moving interface is detected, a local refinement of the mesh is performed, see Figure 9.7b. Next, one time step is performed using the initial time step $\Delta t = 40.000$ s. However, this initial time step size causes the interface to pass over multiple elements, such that for these elements a change of phase is not taken into account properly. The time step size is therefore halved, the time level is reset to $t = 0$ and the computation is repeated using the new time step, see Figure 9.7c. Now that a suitable time

Table 9.10: *Fachinotti: the difference in maximum temperature T_{max} for latent heat $L = 6400$ and $L = 0$. $\Delta t = 1$ s, $n = 100$, $T_\Delta = 0.1\%$ of T_m, $\epsilon = 10^{-3}$.*

	T_{max} ($L = 6400$)	T_{max} ($L = 0$)	difference
exp2	1.96236	2.40911	19%
exp4	1.38266	1.71917	20%
2exp4	1.61519	2.05155	21%
const	2.22568	2.72374	18%

step size has been determined, it is either reused for three successive time steps, after which it is checked whether the time step size can be doubled, or it halved again when needed (up to a given maximum number of times). In the current example, the time step size of 20.000 seconds is reused three times, and is then doubled, see Figures 9.7c-9.7f.

9.5 Applications

In Chapter 4, an optical model and a thermal threshold model have been combined to simulate the recording of data on DVD and Blu-ray disc configurations. In this section we present results that are obtained in case latent heat is taken into account. These results will be compared to those presented in Chapter 4. In addition, the position of the melting front at various time instances during a laser pulse are presented. Although the molten regions give an 'upper bound' of the final mark shape and size, because (re)crystallization is not yet included into the model, an assessment can still be made whether marks recorded in adjacent tracks might be affected in case a land-groove recording strategy is used. In all simulations, the spot is at rest and a single pulse is applied for the duration of 100 ns.

Table 9.11: *Test case 1: 'equal'. The effect of adaptive local mesh refinement. The 'exact' value of $x_m = 0.587$. The maximum number of elements used during the computation is denoted by $n_{\max}$. The bottom row shows the results in case it is not checked whether the moving interface skips one or more elements during a single time step.*

$n_{\max}$	LOR	time	#iters	x_m	$Err_{2,t}$	$Err_{\infty,t}$	$Err_{2,x}$	$Err_{\infty,x}$
100	0	9.6	3.2	0.601	8.1	17	1.3	1.7
103	1	9.8	3.6 (123)	0.593	4.2	7.5	0.74	0.98
111	2	10	4.1 (127)	0.589	2.2	3.9	0.54	0.78
129	3	11	4.5 (131)	0.587	1.4	2.8	0.20	0.20
129	3	10	4.5	0.587	1.6	2.6	0.22	0.19

Table 9.12: *Test case 2: 'unequal'. The effect of adaptively refining the mesh. The 'exact' value of $x_m = 0.742$. The maximum number of elements used during the computation is denoted by $n_{\max}$.*

$n_{\max}$	LOR	time	#iters	x_m	$Err_{2,t}$	$Err_{\infty,t}$	$Err_{2,x}$	$Err_{\infty,x}$
100	0	102	3.0	0.748	2.1	6.0	0.49	1.4
103	1	103	3.1	0.744	0.91	3.2	0.19	0.39
111	2	105	3.5	0.743	0.42	1.6	0.14	0.25
129	3	108	4.1	0.743	0.21	0.76	0.10	0.20

(a)

(b)
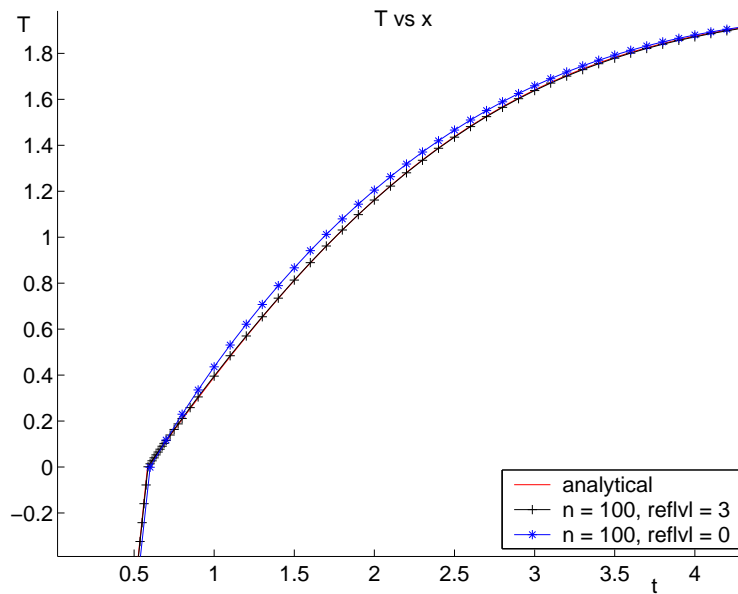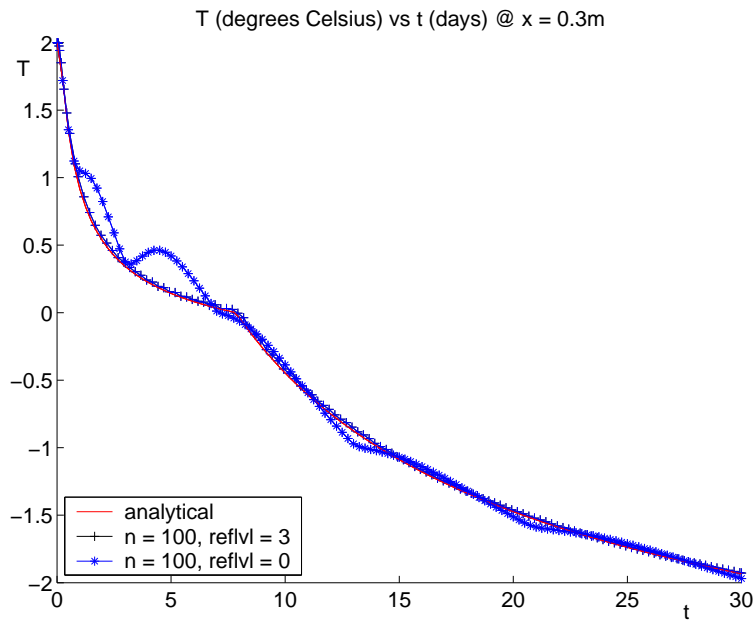
Figure 9.6: *Test case 1: 'equal'. The influence of the local adaptive mesh refinement for n = 100, using the Fachinotti method. (a) T as a function of time (in days) at the point x = 0.3 m, (b) T as a function of position x (zoomed in) at time t = t_end. In both figures, the numerical solution obtained using an LOR = 3 lies 'on top of' the analytic solution.*

(a) $t = 0$ s (basis mesh)

(b) $t = 0$ s (refined mesh)

(c) $t = 20.000$ s

(d) $t = 40.000$ s

(e) $t = 220.000$ s

(f) $t = 300.000$ s
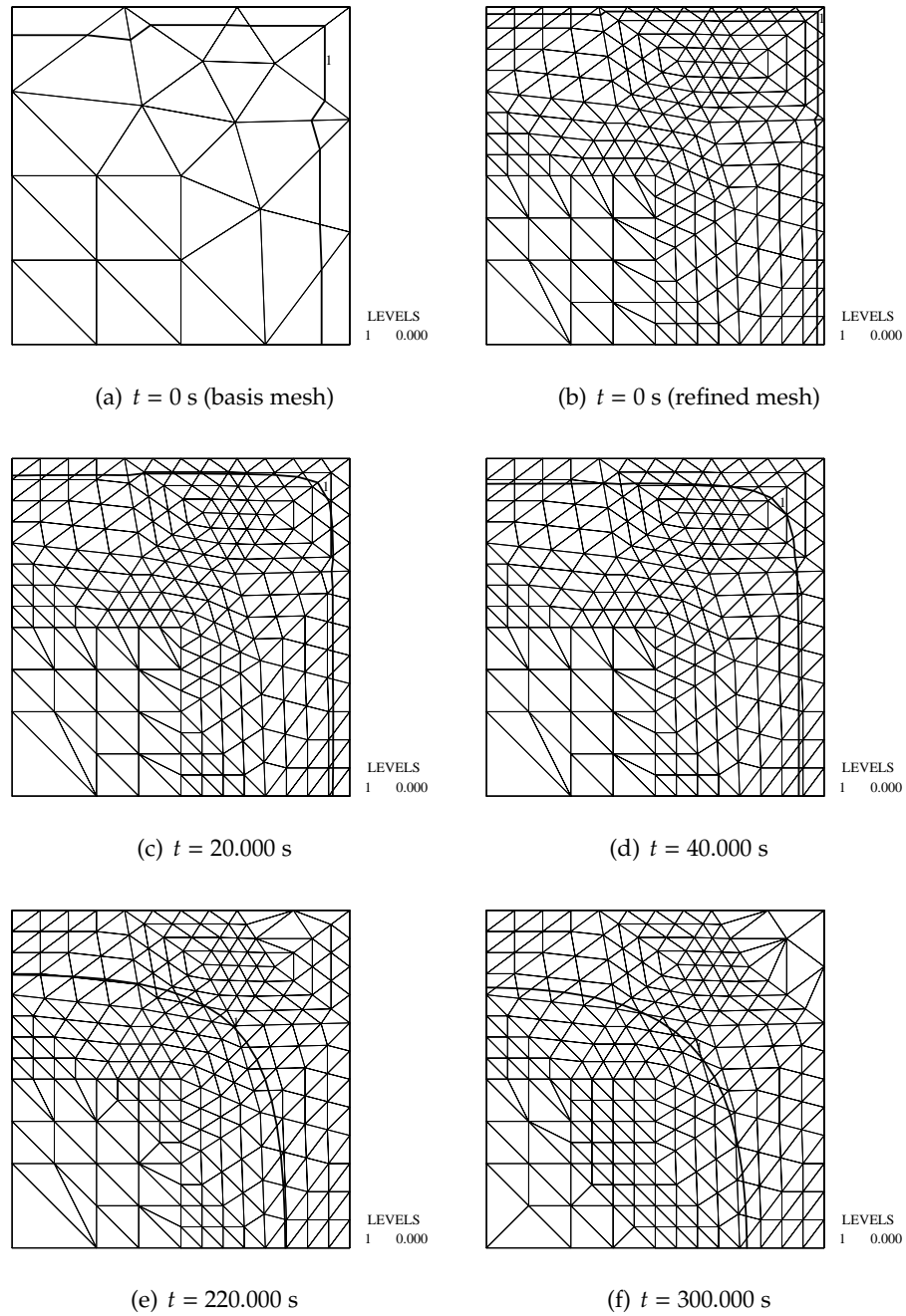
Figure 9.7: *Test case 3: '2D corner'. The position of the $T = T_m$ contour at selected time instances.*

9.5.1 DVD

The first test case is a multilayered DVD-like stack as shown in Figure 4.6. This configuration, for which the material properties are listed in Table 4.1 is taken to be equal to the recording stack called 'case C1' by Peng and Mansuripur [53]. An interesting feature of this configuration is that the groove depth of 50 nm has been exaggerated in order to study to what extent the polarization of the incident spot influences the absorbed energy and the temperature distribution. The Gaussian beam that is incident on the lens has its $1/e$ amplitude at the rim of the aperture of the lens, and the output power of the laser is taken to be 4 mW.

Let us assume that the lens pupil has radius R. The flux through the lens is then given by:

$$\int_0^{2\pi} \int_0^R \frac{1}{2} \sqrt{\frac{\epsilon_0}{\mu_0}} |E|^2 r \, dr \, d\phi = \pi \sqrt{\frac{\epsilon_0}{\mu_0}} \int_0^R \exp\left(-2\frac{r^2}{R^2}\right) r \, dr, \qquad (9.2)$$

$$= \frac{1}{4}\pi R^2 \sqrt{\frac{\epsilon_0}{\mu_0}} \left[1 - \exp(-2)\right]. \qquad (9.3)$$

Because the total flux is given by:

$$\int_0^{2\pi} \int_0^\infty \frac{1}{2} \sqrt{\frac{\epsilon_0}{\mu_0}} |E|^2 r \, dr \, d\phi = \frac{1}{2}\pi R^2 \sqrt{\frac{\epsilon_0}{\mu_0}} \int_0^\infty \exp(-2s) \, ds, \qquad (9.4)$$

$$= \frac{1}{4}\pi R^2 \sqrt{\frac{\epsilon_0}{\mu_0}}, \qquad (9.5)$$

it follows that approximately 86% of the laser light passes through the lens.

Four different recording strategies have been simulated. The incident spot is taken to be either TM polarized, i.e., the magnetic field is parallel to the grooves, or TE polarized, i.e., the electric field is parallel to the grooves, and land and groove recording are considered. In the TM case, 2.97 mW of energy is absorbed inside the phase-change layer, when a land recording strategy is chosen. This means that approximately 74% of the initial output of the laser (4 mW) is absorbed. When groove recording is considered, the amount of optical energy absorbed is equal to 3.01 mW ($\approx$ 75%). For a TE polarized spot, both land and groove recording show an absorption rate of approximately 73%. These values are in good agreement with the value of 74%, as reported in Reference [53].

In Figures 9.8 and 9.9 the temperature distributions are shown for a TE and a TM polarized spot, incident on the center of a land and that of groove, halfway in the phase-change layer. The corresponding absorbed energy distributions are as shown in Figure 4.10. In the computations of

these temperature distributions, a latent heat $L = 640$ J/cm^3 has been taken into account [52]. If we compare Figures 9.8 and 9.9 with Figures 4.11 and 4.12, respectively, it is observed that for this specific DVD stack, the obtained maximum temperature values are approximately 1% lower than when latent heat is not taken into account. However, we emphasize that these relatively small differences only account for this specific configuration and the physical parameters as taken from References [52, 53]. If, for instance, the latent heat is increased by various orders of magnitude, the effect on the temperature distribution becomes distinctive, see Figure 9.10. The figure shows that, if the latent heat increases, the region in which the temperature rises above the melting temperature decreases gradually. Figure 9.10c shows that for larger values of L the phase-change material does not even fully melt at all. Instead, a small region can be discerned in which the temperature resides in the lower band of the artificial mushy region ($T - T_\Delta \leq T < T_m$), as shown in Figure 9.11.

Figure 9.12 shows the evolution of the $T = T_m$ isotherm for a TE polarized spot that is incident on the center of a groove. Inside the phase-change layer, this isotherm determines the melting front. Note that the shape of the molten region, in a plane perpendicular to the intersections shown in the figure, is elliptic, see also Figure 9.8a. More precisely, the region that has molten is slightly wider in the direction along the groove than it is across the groove. Another notable feature is the change in shape of the boundary as the molten region grows. At around $t = 20$ ns, the boundary of the molten region reaches the bottom of the phase-change layer. From this moment onward, the growth is essentially two-dimensional. Although the slope of the boundary increases gradually, it is interesting to see that the slope remains much steeper in the direction along the groove.

When we compare the $T = T_m$ isotherms at $t = t_{\text{end}}$ for a TE and a TM polarized spot, either incident on a groove or on a land, see Figure 9.13, some distinct differences between the configurations become apparent. From the cross sections across the grooves it can be concluded that, for both groove and land recording, the molten region is slightly wider for the TM case. Moreover, in case of land recording, the region that have molten are found to be wider for land recording than for groove recording. Also note that small regions have molten on the adjacent lands in case of a TM polarized spot that is incident on the center of a groove. The cross sections along the grooves hardly show any differences. However, it is worth mentioning that in case of a TE polarized spot, the molten region is slightly longer than for the TM case. This holds for both groove and land recording.

With respect to thermal cross-track cross-talk, we can conclude from Figure 9.13 that in case of a land-groove recording strategy, i.e., when data is written on the lands and in the grooves, it is less likely that undesirable data erasure occurs in case of a TE polarized, than when a TM polarized spot is applied.

(a) TE groove (b) TM groove

(c) TE land (d) TM land
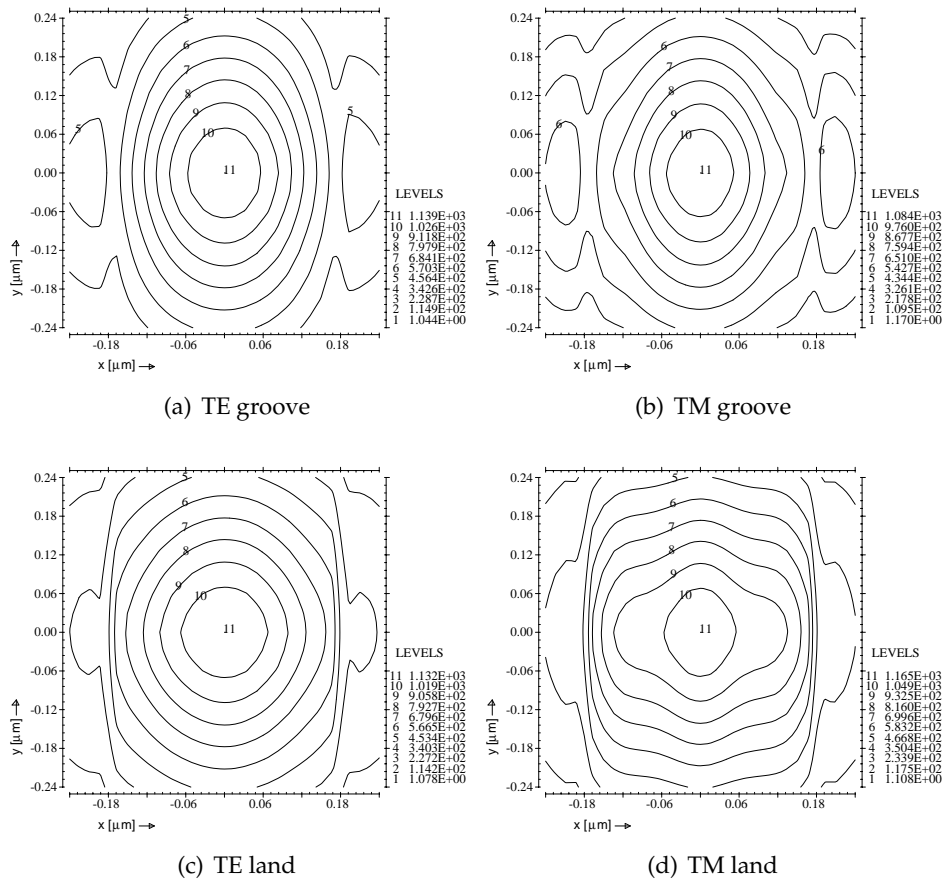
Figure 9.8: *Temperature distributions [°C] halfway in the phase-change layer for a TE and TM polarized spot that is incident on the grooved multilayer of Figure 4.6, for a latent heat L = 640 J/cm³.*

(a) groove (b) land
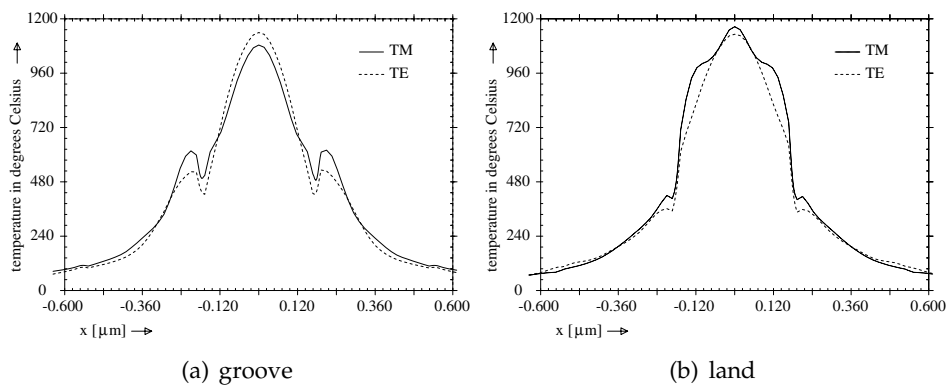
Figure 9.9: *Cross sections of the temperature distributions [°C] halfway in the phase-change layer as shown in Figure 9.8, for a latent heat L = 640 J/cm³.*

(a)

(b)

(c)
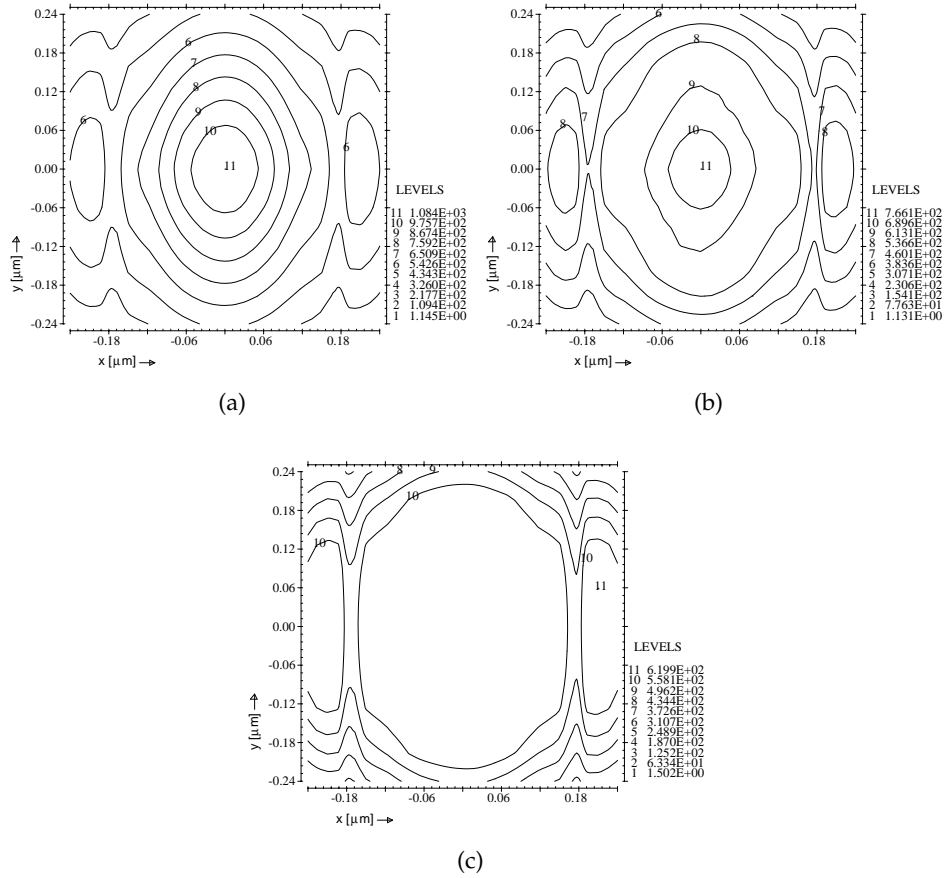
Figure 9.10: *Temperature distributions [°C] halfway in the phase-change layer for a TM polarized spot that is incident on the center of a groove, for a latent heat L = 640, L = 6400, and L = 64000 J/cm³.*

(a)

(b)
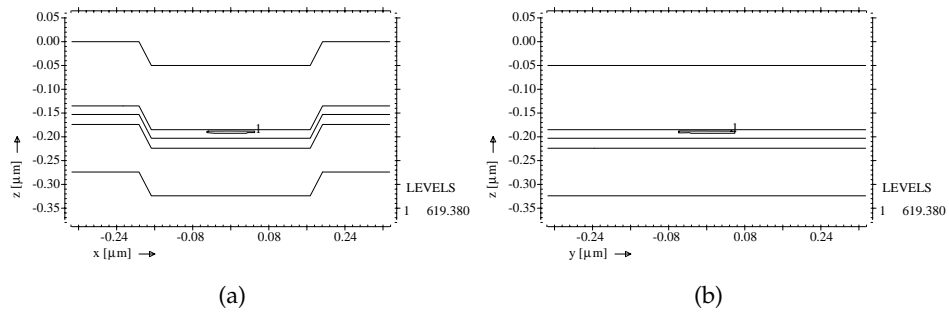
Figure 9.11: *The $T = T_m - T_\Delta$ isotherm for cross sections of Figure 9.10c.*

(a) $t = 12$ ns

(b) $t = 12$ ns

(c) $t = 24$ ns

(d) $t = 24$ ns

(e) $t = 60$ ns

(f) $t = 60$ ns

(g) $t = 100$ ns

(h) $t = 100$ ns
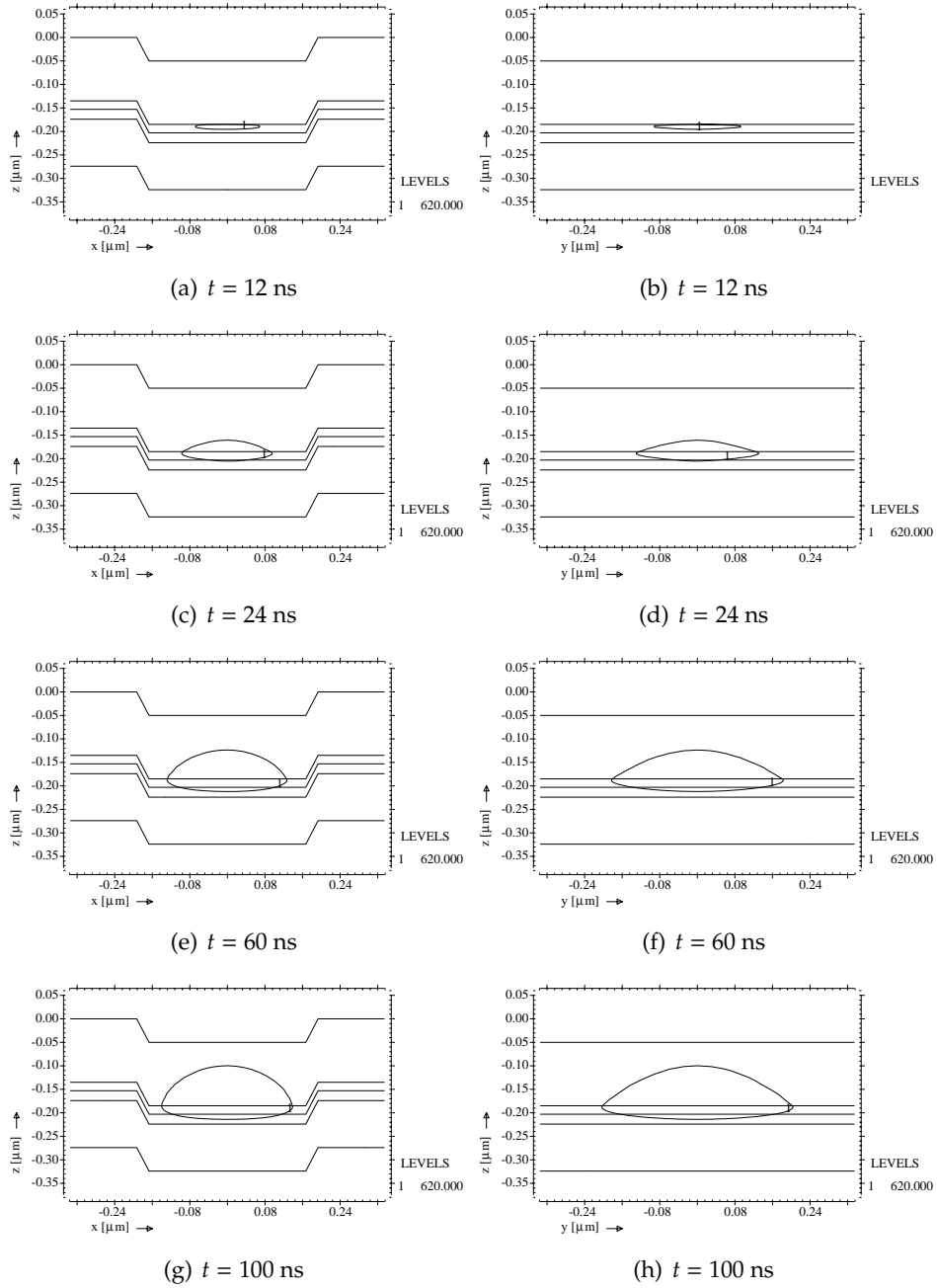
Figure 9.12: *Evolution in time of the melting front ($T_m = 620$ °C contour) for a TE polarized spot that is incident on the center of a groove, for a latent heat $L = 640$ J/cm^3. (left) Across the groove, (right) along the groove.*

(a) TE groove

(b) TE groove

(c) TM groove

(d) TM groove

(e) TE land

(f) TE land

(g) TM land

(h) TM land
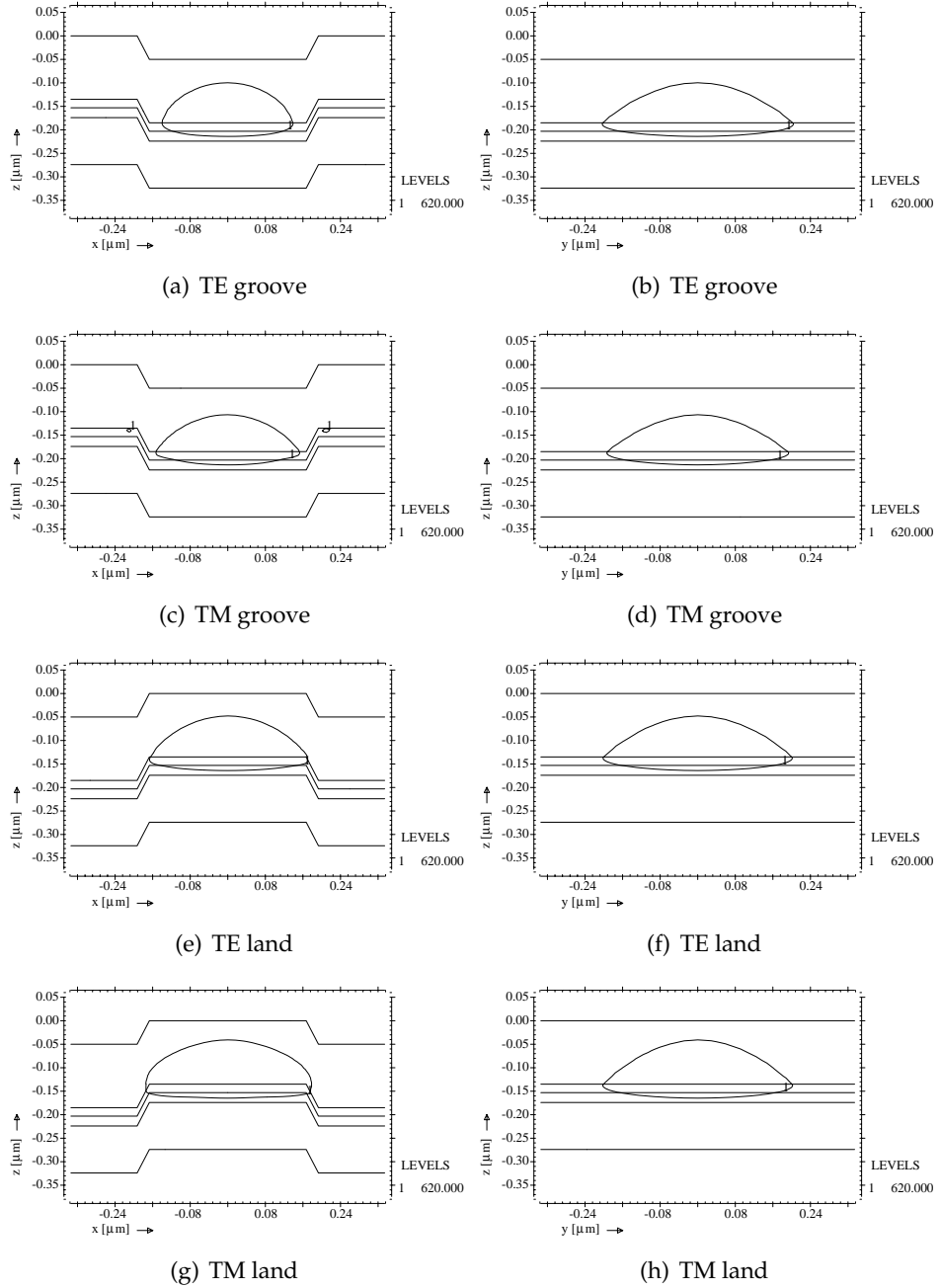
Figure 9.13: *Mark boundary ($T_m = 620$ °C contour) at $t = t_{\mathrm{end}} = 100$ ns for a TE and TM polarized spot that is incident on the center of a land and of a groove, for a latent heat $L = 640$ J/cm^3. (left) Across the groove, (right) along the groove.*

(a) groove   (b) land
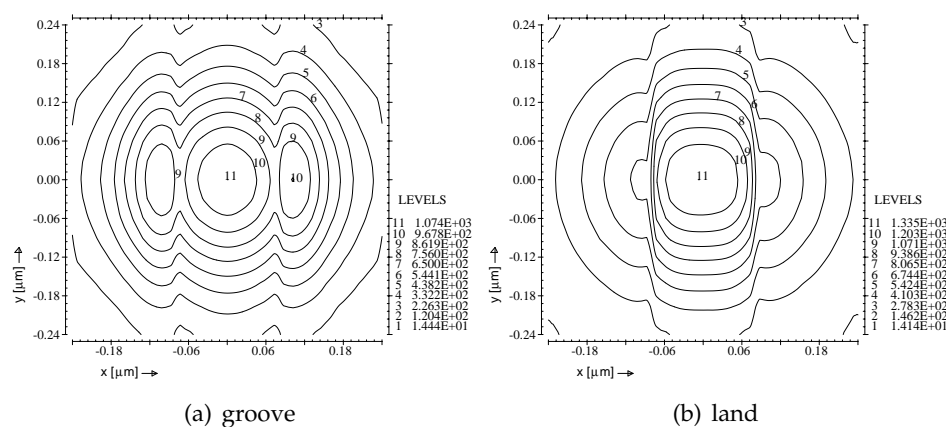
Figure 9.14: *Temperature distributions [°C] halfway in the phase-change layer for a TM polarized spot that is incident on the center of a land and that of a groove for the Blu-ray stack of Figure 4.15.*

9.5.2   Blu-ray

The second stack configuration that was studied in Chapter 4 is that of a Blu-ray disc. A typical Blu-ray recording stack is shown in Figure 4.15. The track pitch for a Blu-ray disc is less than half of that of the DVD disc (320 nm) and the focusing lens has a numerical aperture equal to 0.85. Of course, as the name of the disc format already implies, a blue laser (λ = 405 nm) is used. The groove depth of 50 nm has been exaggerated, similar to the DVD simulations. The power level of the laser is set to 15 mW, see for instance Meinders et al. [44].

Figure 9.14 shows the temperature distributions halfway in the phase-change layer for a TM polarized spot that is incident on the center of a land and that of a groove in case a latent heat of 640 J/cm^3 has been taken into account. The corresponding absorbed energy distributions are shown in Figures 4.16 and 4.17. Similar to the DVD simulation, the temperatures found when the latent heat is not incorporated, are approximately 1% higher.

In Figures 9.15 and 9.16, the evolution of the $T = T_m$ isotherm is shown for a TM polarized spot that is incident on the center of a groove, and the center of a land, respectively[1]. Inside the phase-change layer, this isotherm determines the melting front. In contrast to the DVD case, this example clearly illustrates the occurrence of cross-track cross-talk. However, for this specific stack configuration, references from literature or experimental data to validate these results, are currently not available.

---

[1]In Figures 9.15 and 9.16, an additional interface is shown halfway in the phase-change layer. This interface however is artificial, and was added for plotting purposes.

(a) $t = 3$ ns

(b) $t = 3$ ns

(c) $t = 9$ ns

(d) $t = 9$ ns

(e) $t = 36$ ns

(f) $t = 36$ ns

(g) $t = 100$ ns

(h) $t = 100$ ns
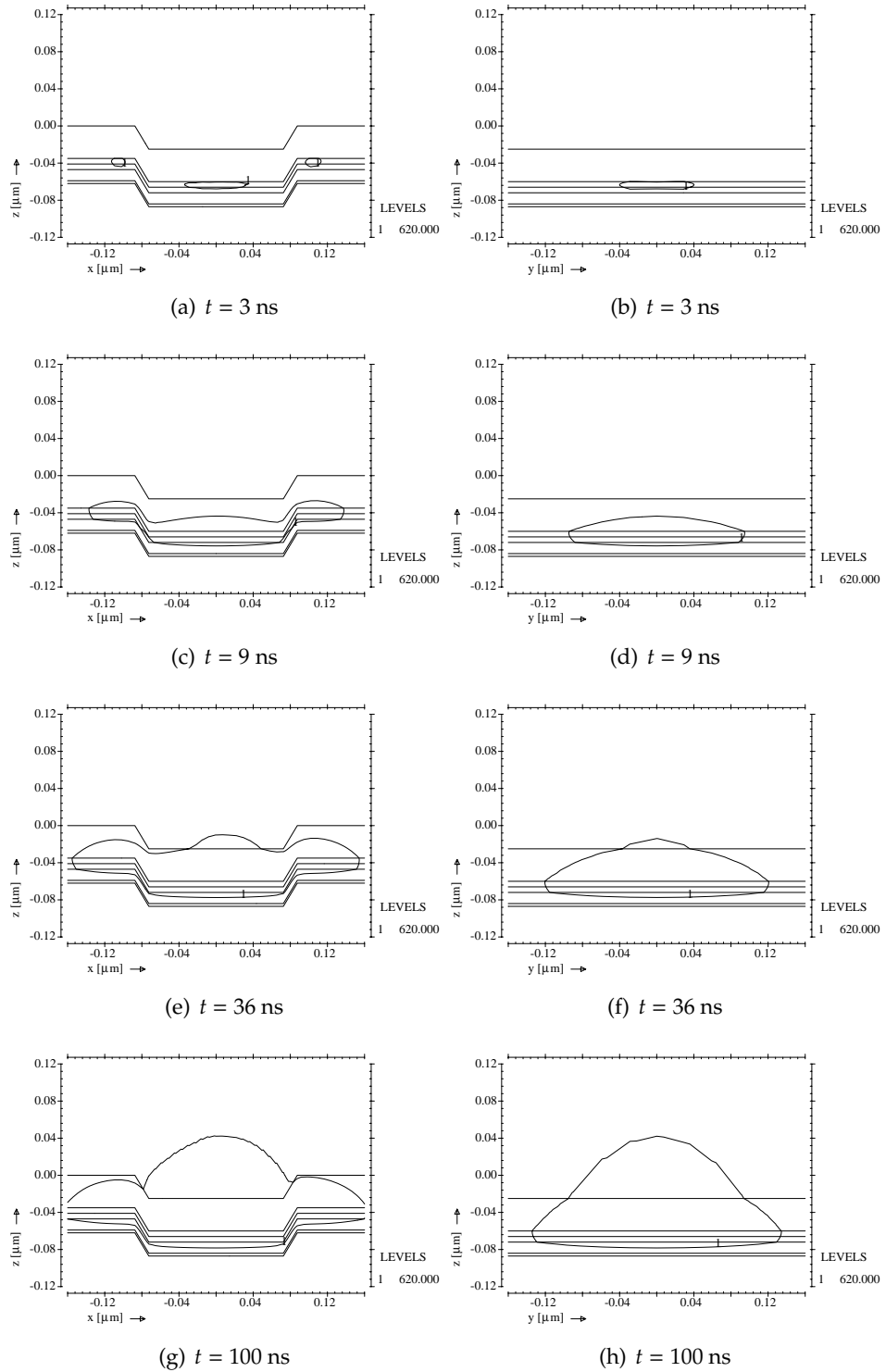
Figure 9.15: *Evolution in time of the melting front ($T_m = 620$ °C contour) for a TM polarized spot that is incident on the center of a groove for the Blu-ray stack of Figure 4.15. The latent heat $L = 640$ J/cm^3.*

(a) $t = 3$ ns

(b) $t = 3$ ns

(c) $t = 9$ ns

(d) $t = 9$ ns

(e) $t = 36$ ns

(f) $t = 36$ ns

(g) $t = 100$ ns

(h) $t = 100$ ns
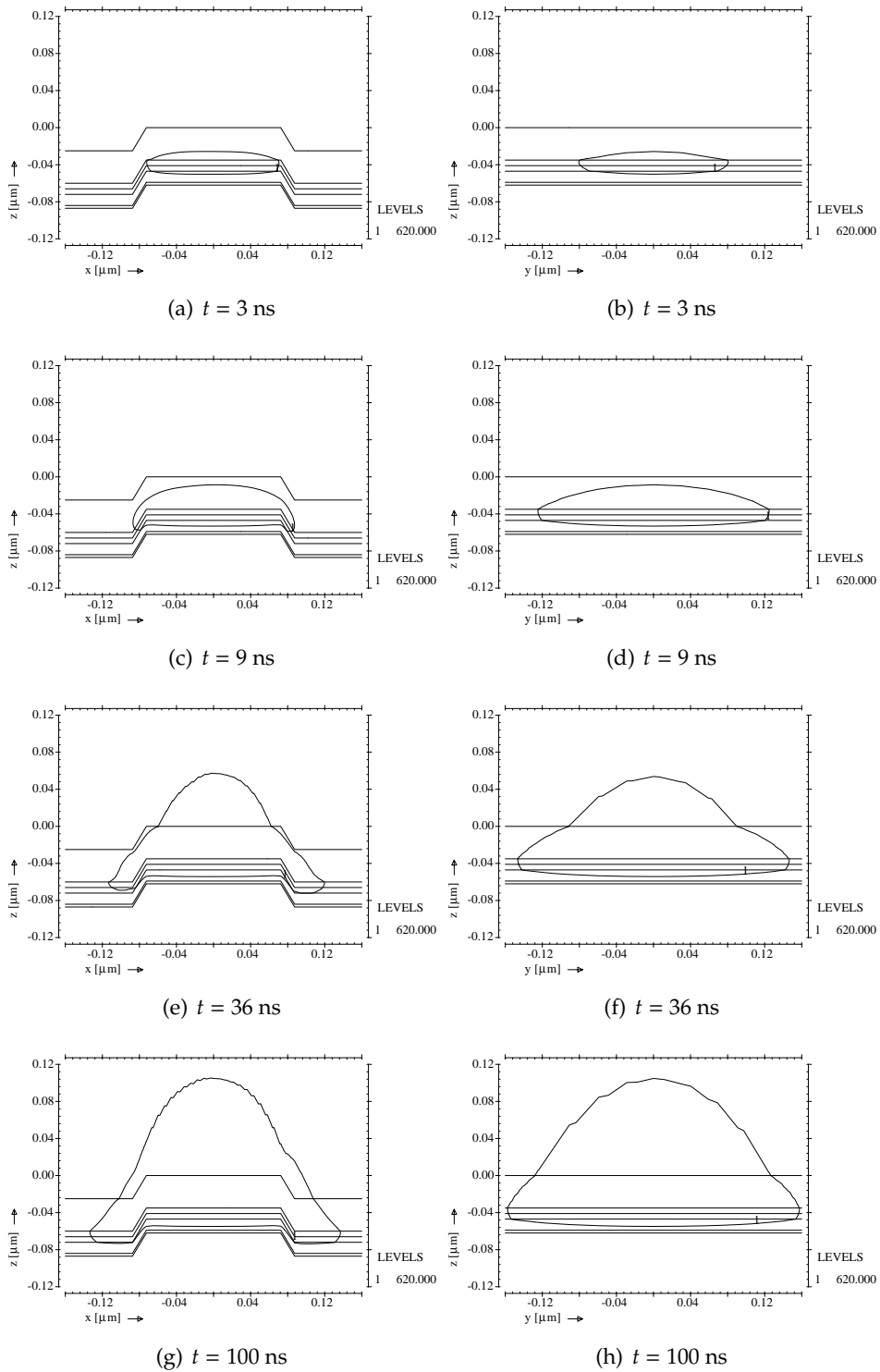
Figure 9.16: *Evolution in time of the melting front (T_m = 620 °C contour) for a TM polarized spot that is incident on the center of a land for the Blu-ray stack of Figure 4.15. The latent heat L = 640 J/cm^3.*

9.6 Conclusions

The temperature approach is the method of choice to be used in our Stefan model. Not only does it perform better than the enthalpy method by Nedjar, it can be easily integrated into an existing finite element code.

The convergence behavior of the Newton-Raphson iterative process can be improved by means of a line search procedure. In general, quadratic regression is sufficient to obtain the line search parameter α. For isothermal problems, the presence of a source term will in general lead to a breakdown of the employed numerical solution method. Therefore, an artificial mushy region is introduced. For the test problems considered, it is found that for the width of the mushy zone, a value of approximately 0.1% of the melting temperature is a feasible choice.

As expected, the adaptive local grid refinement provides a gain in accuracy, while at the same time the computational costs are reduced. Furthermore, results for the DVD test case are found to be in good agreement with the results reported in the literature. In order to be able to give a qualitative assessment of the results for the Blu-ray simulations, experimental validation is needed.

For these specific DVD and Blu-ray configurations, it is found that the effects of the inclusion of latent heat on the temperature distribution, and thus on the position of the melting front, are small. This is in agreement with the predictions of Meinders and Borg [42]. Nonetheless, we believe it is premature to conclude that the inclusion of latent heat can be fully neglected in phase-change recording simulations in general, since the effects of the inclusion of latent heat might be stronger for stack geometries and configurations that are different from those considered in this thesis.

CHAPTER 10

Conclusions

In optical rewritable recording media, such as the Blu-ray Disc, amorphous regions are formed on a crystalline background of a phase-change layer, by means of short, high power laser pulses. These amorphous regions are called marks. The shape and size of a mark are determined by the region that melts due the laser light, solidification and the effects of (re)crystallization.

In this thesis, a three-dimensional model is proposed for the melting component of the formation of a mark inside a grooved multilayered recording stack. It is assumed that the phase-change material melts at a melting point. For these so-called isothermal materials, a two-phase Stefan problem formulation is presented. The restriction to isothermal problems is not a limitation, since the work described in this thesis has been developed in such a way, that it can be easily extended to mushy problems.

To incorporate latent heat into the mark formation model, several numerical methods for solving two-phase Stefan problems have been evaluated. The considered methods either track the position of the moving interface explicitly, such as the level set based methods and the temperature approach, or implicitly, as in the enthalpy methods. Unfortunately, many methods are either only feasible in 1D, restricted to finite difference discretizations, do not easily allow for the breaking and merging of multiple fronts, cannot handle both mushy and isothermal cases, or are too elaborate to implement.

Two numerical techniques have been selected that meet the imposed requirements: an enthalpy method, in which a relaxed linearization of the enthalpy is employed, and a temperature based method, in which the integrals, appearing from the variational formulation, for elements intersected by the moving interface, are evaluated over the liquid and solid parts separately. Both methods have been discussed in detail and their performance

133

has been compared.

The enthalpy method is found to be the least suitable approach for solving our moving boundary problem. The most notable drawbacks of this approach are the step-like behavior observed for the temperature as function of time, which is inherent to enthalpy methods, slow convergence of the pseudo-Newton iterative process, and wiggles in the front position.

The temperature method is found to be the most accurate method, in particular on coarser meshes, and fast convergence rates for Newton-Raphson are observed for moderate values of the latent heat. However, the latent heat contribution is included in the temperature formulation in the form of a time dependent source term, which, for isothermal problems, is highly nonlinear. This means that, for relatively high values of the latent heat, one or two line search steps are required, to ensure convergence of Newton-Raphson process. Also, poor convergence has been observed in case a source term was added to the isothermal problem formulation. As a remedy, the addition of an artificial mushy region has been proposed and the choice of a suitable value for the width of the mushy zone has been addressed.

The computational domain that is used in the thermal computations for phase-change recording simulations, is relatively large with respect to the size of a mark. The dimensions of the domain are chosen such that at least three periods of the grooved structure are included and moreover, the boundary conditions on the fixed outer boundary should not influence the solution inside the region of interest, i.e., the location of the mark, at the center of the domain. Due to the size of the domain, a typical computational grid consists of millions of elements. In order to still accurately capture the moving interface, a local adaptive grid refinement procedure has been added to the mark formation model. The refined mesh is always constructed from the initial, or basis mesh. In this way, interpolation errors when transferring data from one mesh to the next, are either avoided or kept limited. The number of elements that is added to the mesh is also kept small, since only the basis elements intersected by the moving interface, and selected neighboring basis elements, are refined. Besides, the level of refinement decreases away from the intersected basis elements.

Finally, results are presented for DVD and Blu-ray disc recording simulations. For DVD, the results are in good agreement with numerical results available from the literature. However, experimental data is needed to validate the results for the specific Blu-ray Disc configuration considered in this thesis. The effect of the latent heat on the temperature distribution and the shape and size of the region that has molten, is found to be small for the considered recording stacks. Nonetheless, we believe it is premature to conclude that the inclusion of latent heat can be fully neglected in phase-change recording simulations in general, since the effects of the inclusion of latent heat might be stronger for stack geometries and configurations that are different from those considered in this thesis.

10.1   Recommendations for future research

The primary focus of the research presented in this thesis has been on modeling the melting component of the formation of marks for isothermal phase-change materials. However, only minor modifications to the present model formulation and the computer code are required in order to allow for arbitrary phase transitions. Other features, such as multi-pulse recording strategies and the movement of the spot/disc, have been implemented, but cannot be studied yet due to the limited available computer memory (~3 GB of RAM). Larger memory storage is also required in order to obtain more accurate results for the DVD and Blu-ray simulations.

The developed melting model, which provides an accurate position of the melting front, in combination with the adaptive local mesh refinement code, is expected to form a solid basis for the inclusion of for instance crystallization kinetics.

APPENDIX A

Crystallization

The processes of amorphization of molten regions during quenching and the crystallization of the amorphous state during erasing are very complicated. In order to model these processes, knowledge of the crystallization kinetics is of great importance.

A.1 Crystallization kinetics

Many of the existing descriptions of crystallization kinetics come from thermodynamics. They are mainly based upon two theories: Johnson-Mehl-Avrami-Kolmogorov (JMAK) theory and classical nucleation theory. In both theories it is assumed that crystallization occurs either by the nucleation of critical size particles and their subsequent growth within the untransformed region, or by the growth of crystallites at the boundary between the untransformed region and the surrounding crystalline matrix. With JMAK theory, the volume fraction of crystallized material can be computed in terms of nucleation and growth rates. The classical nucleation theory allows for the calculation of the nucleation and growth rates, and the distribution of the crystallite size.

According to Senkader et al. [57] both these approaches have inevitable limitations, mostly since in optical recording nucleation and growth occur within very short time scales. The authors remark that the nucleation in a real system not only involves clusters of critical size. The progress of the nucleation also depends on the interaction of the critical size nuclei with sub-critical and supercritical sized clusters of molecules. Therefore, Senkader et al. propose a model to compute the distribution of cluster sizes. For another example of a dynamic theory, based on cluster concentrations, the reader is referred to Reference [69].
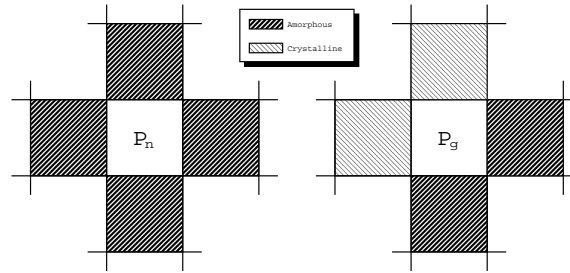
Figure A.1: *In the example of the simplified recrystallization model in the text, the probability that a cell transforms from the crystalline to the amorphous state depends on the state of its nearest neighbors.*

Despite the more realistic modeling that the dynamic models provide for and the limitations of models based on either JMAK theory or the standard theory of kinetics, we will in the following only consider the classical crystallization model. A motivation for this choice is that the classical model gives an explicit formula for the growth velocity.

Next, we will first give an outline of the general idea of the nucleation and growth model by considering a very simplified, but illustrative, two-dimensional example, based on the implementation by Peng et al. [52]. After the example we will subsequently discuss into detail the Gibbs free energy, nucleation and growth. In the sections on nucleation and growth we will mainly focus on the more general crystallization model as presented in Reference [52]. A slightly simplified model assuming spherical nucleus growth [25, 66], will also be considered.

A.1.1 A simplified example

The recrystallization of an amorphous region of a section of PC material of unit thickness can for instance be modeled as follows. First the section of interest is discretized into $n \times n$ unit control volumes. Each control volume (or cell) can either be in the amorphous solid phase or the crystalline solid phase.

Each step, for every amorphous control volume there is a statistical probability that atoms will cluster and form a stable crystalline nucleus. This probability depends on temperature (averaged over the control volume) and the status of the adjacent cells, see Figure A.1. If none of the four closest neighbors is crystalline, there is a probability $P_n(T)$ for a stable nucleus to be formed and the amorphous cell to become crystalline. Otherwise, when the amorphous cell has at least one crystalline neighbor, it has probability $P_g(T)$ to become crystalline through growth of the crystalline surroundings.

In case P_g is relatively large compared to P_n, the crystallization is called growth dominated. When P_n is relatively larger than P_g, the crystallization

is called nucleation dominated.

Figures A.2 and A.3 show results of a simulation of the recrystallization of a mark, consisting of three overlapping amorphous dots, in case of growth dominated crystallization and nucleation dominated crystallization, respectively. For simplicity, in these simulations P_n is assumed to be independent of temperature and the probability P_g has been replaced by a prescribed rate of growth: in the growth dominated case every step an amorphous cell with at least one crystalline neighbor becomes crystalline; for nucleation dominated crystallization this happens every fifth step. We stress that the probabilities and growth rate in this example have been chosen such that the difference between nucleation dominated and growth dominated crystallization is evident, and are not related to any realistic situation.

Even though the example uses a very simplified model, it clearly shows the distinct difference between nucleation dominated and growth dominated recrystallization. Before we come to describe the crystallization process, it is important to first understand the driving force behind this process, the so-called Gibbs free energy. The following section contains fragments taken from Reference [29].

A.1.2 Gibbs free energy

Some reactions are spontaneous because they give off energy in the form of heat ($L < 0$). Others are spontaneous because they lead to an increase in the disorder of the system ($\Delta S > 0$). Calculations of the change of enthalpy L and the change of entropy ΔS can be used to probe the driving force behind a particular reaction. In order to understand what happens when one of the potential driving forces behind a chemical reaction is favorable and the other is not, one can consider the balance between these forces, known as the Gibbs free energy. The Gibbs free energy G of a system at any moment in time is defined as the enthalpy of the system minus the product of the temperature times the entropy of the system: $G = H - TS$.

The Gibbs free energy of the system is a state function because it is defined in terms of thermodynamic properties that are state functions. The change in the Gibbs free energy of the system that occurs during a reaction is therefore equal to the change in the enthalpy of the system minus the change in the product of the absolute temperature T times the entropy of the system:

$$\Delta G = L - \Delta(TS). \tag{A.1}$$

If the reaction is run at constant temperature, this equation can be written as follows:

$$\Delta G = L - T\Delta S. \tag{A.2}$$

(a) $t = 0$

(b) $t = 5$

(c) $t = 10$

(d) $t = 15$

(e) $t = 20$

(f) $t = 25$
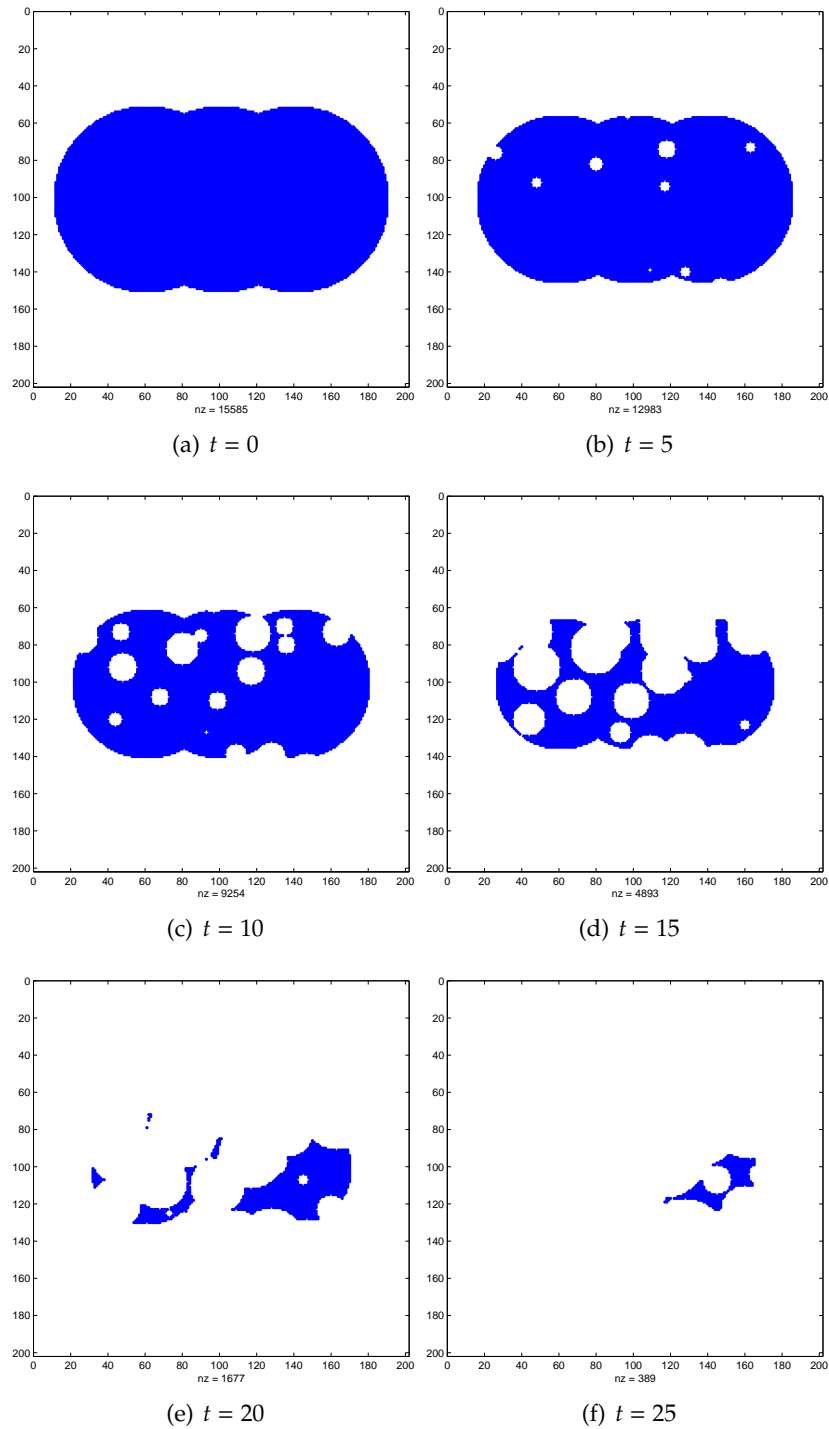
Figure A.2: *An example of growth dominated recrystallization. The amorphous/crystalline interface expands at one control volume per step. The nucleation probability P_n for an amorphous control volume is < 0.0001. The complete mark is erased at $t = 31$. nz is the number of amorphous control volumes.*

(a) $t = 0$

(b) $t = 5$

(c) $t = 10$

(d) $t = 15$

(e) $t = 20$

(f) $t = 25$
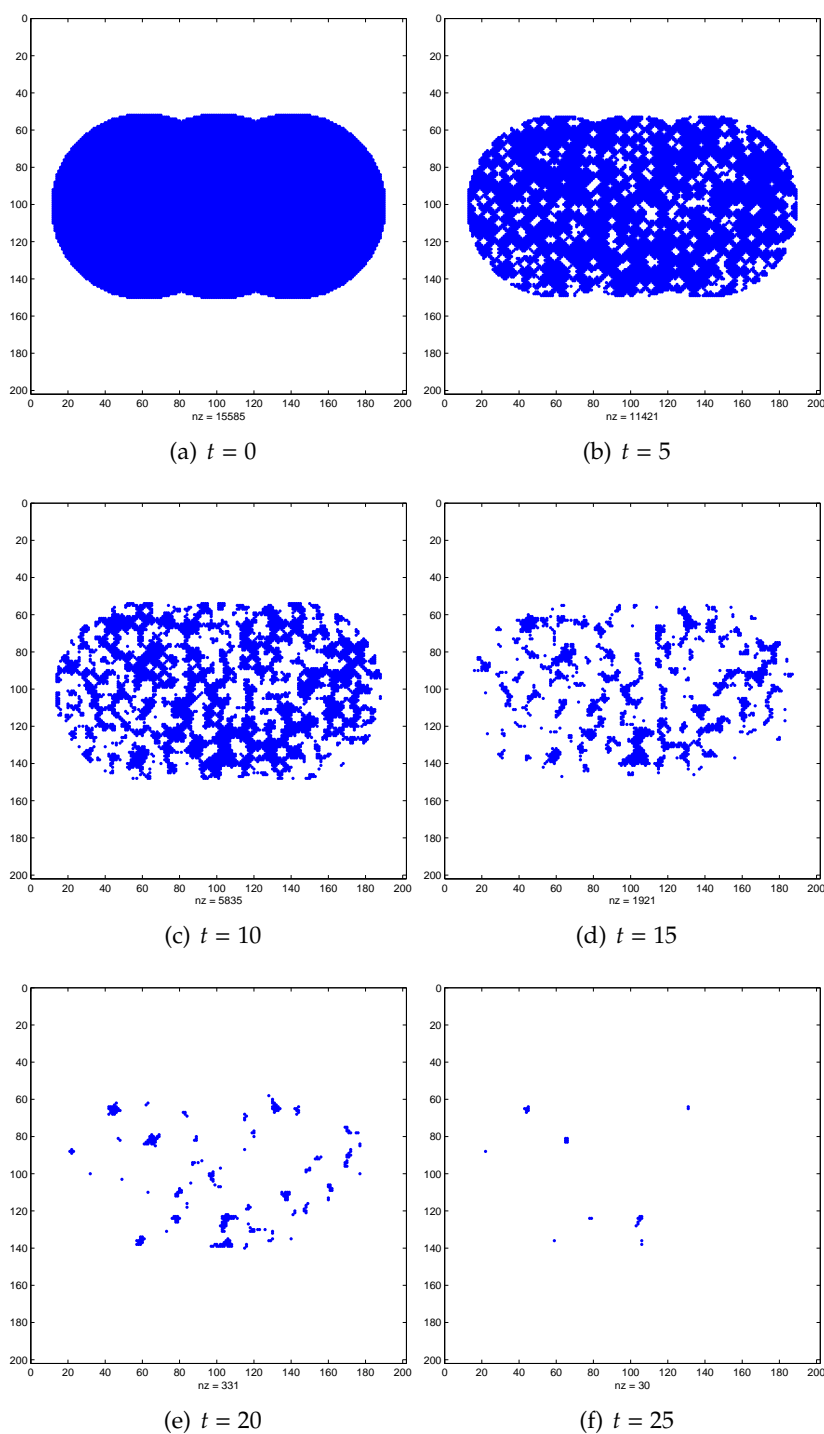
Figure A.3: *An example of nucleation dominant recrystallization. The amorphous/crystalline interface expands at one fifth of a control volume per step. The nucleation probability P_n for an amorphous control volume is < 0.005. The complete mark is erased at $t = 30$. nz is the number of amorphous control volumes.*

As we have seen, the enthalpy and entropy terms have different sign conventions. The entropy term is therefore subtracted from the enthalpy term when calculating ΔG for a reaction.

favorable	unfavorable
$L < 0$	$L > 0$
$\Delta S > 0$	$\Delta S < 0$

Because of the way the free energy of the system is defined, ΔG is negative for any reaction for which L is negative and ΔS is positive.

Reactions are classified as either exothermic ($L < 0$) or endothermic ($L > 0$) on the basis of whether they give off or absorb heat. Reactions can also be classified as exergonic ($\Delta G < 0$) or endergonic ($\Delta G > 0$) on the basis of whether the free energy of the system decreases or increases during the reaction.

The balance between the contributions from the enthalpy and entropy terms to the free energy of a reaction depends on the temperature at which the reaction is run. The equation used to define Gibbs free energy (A.2) suggests that the entropy term will become more important as the temperature increases. Since the entropy term is unfavorable, the reaction should become less favorable as the temperature increases.

A.1.3 Nucleation

In the amorphous phase, there is a statistical probability that atoms will momentarily form a crystalline cluster. These so-called embryos are potential nuclei for the crystallization process. Clusters that exceed some critical size can reduce the system free energy only through further growth and hence stable nuclei are capable of sustained existence. Sub-critical clusters decrease the system free energy via shrinking in size and thus will tend to dissolve back in to the parent phase [56]. The Gibbs free energy per volume of the crystalline state is lower than that of the amorphous phase. The change of Gibbs free energy ΔG_n, or excess Gibbs free energy, corresponding to the crystalline-to-amorphous transition is given by (A.2):

$$\Delta G_n = L - T\Delta S. \tag{A.3}$$

In order for an embryo to transform into a stable nucleus, the so-called heat of formation ΔG_f, which is the net Gibbs free energy between a stable nucleus and an embryo, has to exceed the activation energy ΔG^*, or energy barrier.

For spherical nuclei of radius r, the heat of formation is given by [66]:

$$\Delta G_f = f(\theta)\,(A\gamma - V\Delta G_n) = f(\theta)\left(4\pi r^2\gamma - \frac{4\pi r^3}{3}\Delta G_n\right), \tag{A.4}$$
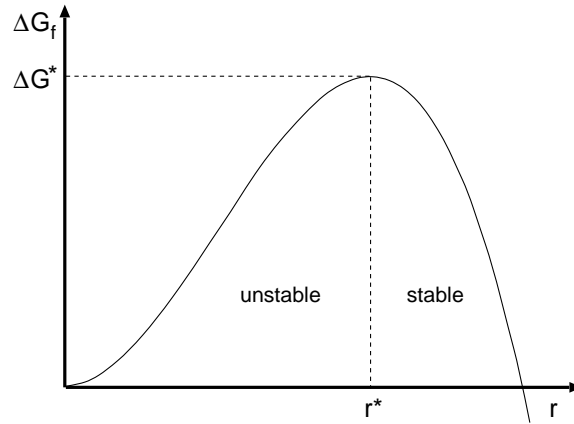
Figure A.4: *The heat of formation ΔG_f as a function of the radius r (for spherical nuclei). For a potential cluster to become stable, i.e. to form a crystalline nucleus, the net difference in Gibbs free energy between an unstable and a stable cluster must exceed the energy barrier ΔG^*.*

where V is the volume and A the surface area of the nucleus, γ is the interface energy and $f(\theta)$ is a function of contact angle θ. For homogeneous nucleation, $f(\theta) = 1$ and the energy barrier ΔG^* is equal to the maximum of $\Delta G_f(r)$. At the critical radius $r^* = 2\gamma/\Delta G_n$ this maximum is reached:

$$\Delta G^* = \frac{16\pi}{3} \frac{\gamma^3}{\Delta G_n^2} f(\theta). \tag{A.5}$$

In case of inhomogeneous nucleation, i.e. in the presence of impurities, which lower the interface energy, the critical free energy is reduced. Therefore, $f(\theta) < 1$ for inhomogeneous nucleation.

Table A.1: *Numerical values of the kinetics parameters of a $Ge_2Sb_2Te_5$ alloy as given in Reference [52].*

	value	unit
E_{a_1}	2.19	eV
E_{a_2}	2.23	eV
T_m	616	°C
T_N	405	°C
T_g	400	°C
L_1	418.9	J/cm^3
L_2	218.5	J/cm^3
α	4×10^{25}	s^{-1}

Note that for large radii r the volume related term in equation (A.4) is dominant, while for small clusters the surface term dominates. This is of special importance when considering the effect of the thickness of the PC layer on the crystallization behavior.

When arbitrarily shaped nuclei are considered the energy barrier is given by:

$$\Delta G^* = \tilde{A}\frac{\gamma^3}{\Delta G_n^2}f(\theta), \tag{A.6}$$

where $\tilde{A}$ is related to the volume and surface area of the nucleus and is temperature dependent. However, in agreement with Reference [52], we will assume $\tilde{A}$ to be temperature independent, in which case its value may be determined from the peak temperature T_N at which the rate of nucleation is at maximum.

The temperature dependence of the excess Gibbs free energy (A.3) may be approximated by

$$\Delta G_n = \begin{cases} L_2\left[1 - \frac{T}{T_g}\left(1 - \frac{L_1}{L_2}\frac{T_m - T_g}{T_m}\right)\right], & T \leqslant T_g, \\ L_1\frac{T_m - T}{T_m}, & T > T_g, \end{cases} \tag{A.7}$$

where L_1 and L_2 are the latent heat of the solid-to-liquid transition and the exothermic heat of the amorphous-to-crystalline transformation, respectively, T_g is the glass transition temperature and T_m is the melting temperature.

The (time-independent) rate of nucleation I can be expressed as:

$$I = \alpha\exp\left(-\beta\left[E_{a_1} + \Delta G^*\right]\right). \tag{A.8}$$

Here, α is a frequency factor related to the atomic jumping frequency; $\beta = 1/k_B T$, where k_B is the Boltzmann constant; E_{a_1} is the activation energy associated with the jump of an atom from the amorphous phase to the critical nucleus of the crystalline phase. For spherical nuclei, ΔG^* is given by equation (A.5). Otherwise, equation (A.6) applies.

The probability for an untransformed grid volume ΔV to become a crystalline nucleus during a time interval Δt is then given by

$$P_n = I\Delta t\Delta V. \tag{A.9}$$

A.1.4 Growth

Besides through nucleation, an amorphous region may become crystalline by growing from an adjacent nucleus or from the boundary of the surrounding crystalline regions. The growth velocity V_g of a crystallite is written as:

$$V_g = ga_0\alpha\exp(-\beta E_{a_2})[1 - \exp(-\beta\Delta G_n)], \tag{A.10}$$
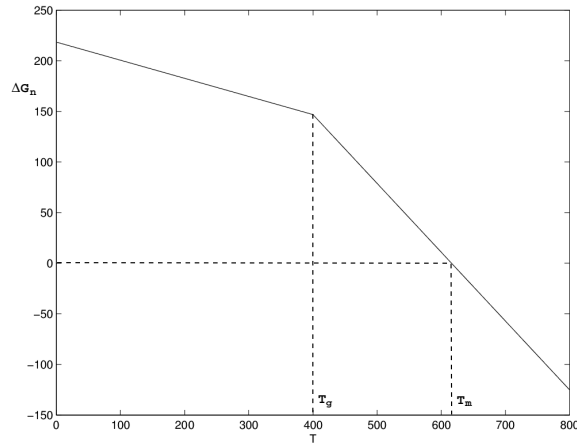
Figure A.5: *Approximation of the temperature dependence of the excess Gibbs free energy ΔG_n as in (A.7). The numerical values as in Table A.1 have been used.*

where g is a factor related to the growth mode; a_0 is the atomic jump distance; and E_{a_2} is the activation energy associated with the diffusion of atoms. In order to simulate lateral growth, Peng et al. assume g to be proportional to $\exp[-0.8/(1-T/T_m)]$ [52].

The growth probability for an untransformed grid volume ΔV is then given by

$$P_g = V_g \Delta t \Delta V. \tag{A.11}$$

In case spherical grain growth is assumed the nucleus radius can be directly calculated from the growth velocity as

$$r(t) = \sum_{t>\tau} V_g \Delta t/g, \tag{A.12}$$

where τ is the time at which this grain nucleated.

The numerical values of some of the quantities mentioned above are listed in Table A.1.

For the crystallization model as presented above, it is likely that a much finer grid is used than that of the melting and solidification model. As long as the crystallites are smaller than a grid cell of the coarser mesh, growth can be modeled using the above described growth model. As soon as the crystallites have grown beyond the grid size of the coarser mesh, the consecutive growth can be modeled using a moving boundary method.
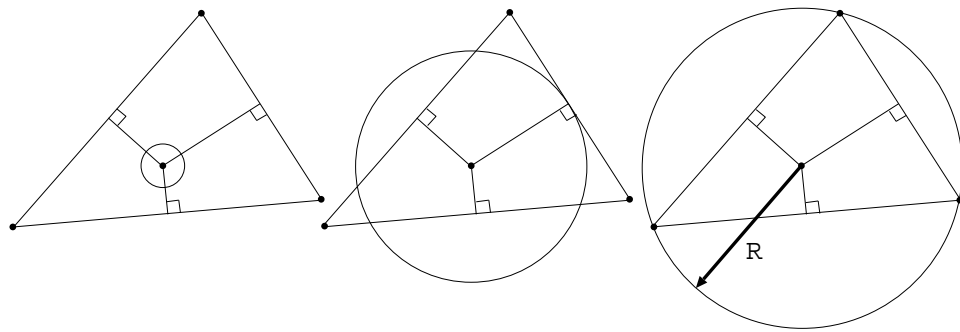
Figure A.6: *A spherical crystallite growing in the circumcenter of a mesh triangle.*

Remark: In case a FEM is used for computing the temperature distribution, a possible method of including a recrystallization model on the same mesh could be the following. Assume that in 2D a triangulation of the region of interest has been performed. As control volumes (areas) for the recrystallization model we then choose the triangles of the mesh. Each triangle which is fully amorphous then has a probability $\tilde{P}_n$ that a stable nucleus will form inside the triangle. When a nucleus has formed, we assume that it is located in the circumcenter of the triangle, see Figure A.6. The nucleus is then assumed to grow at a speed $\tilde{V}_g$. If the radius of the nucleus has become larger than the circumradius, the triangle is considered to be fully crystalline. Besides, since the nucleus has grown beyond the grid size of the mesh, it's consecutive growth can be modeled using a moving boundary method.

Curriculum vitae

- 2002-present: Delft University of Technology, The Netherlands, PhD student in Numerical Analysis, supported by the Netherlands Technology Foundation (STW), subject: *Mark formation model for optical rewritable recording*, daily advisors: dr.ir. C. Vuik and ir. A. Segal, Delft Institute of Applied Mathematics, Faculty of Electrical Engineering, Mathematics and Computer Science

- 2004-2006: Representative of the Numerical Analysis group of Delft University of Technology, Delft, in the J.M. Burgerscentrum PhD contact group. Chairman for one year (2004-2005)

- 2005: Organization of PhDays 2005

- 2004: Organization of outing, Delft Institute of Applied Mathematics, Delft

- 1996-2002: Delft University of Technology, Delft, MSc degree in Applied Mathematics, *cum laude*

- 1990-1996: Vlietland College, Leiden, VWO

- Born on June 3, 1978, in Leiden, The Netherlands

List of publications

- J.H. Brusche, A. Segal, C. Vuik, and H.P. Urbach. A comparison of an enthalpy and a temperature method for melting problems on composite domains. In P. Wesseling, E. Oñate, and J. Périaux, editors, Proceedings of ECCOMAS 2006, the European Conference on Computational Fluid Dynamics. TU Delft, Delft, 2006. CD ROM ISBN 90-9020970-0.

- J.H. Brusche, A. Segal, H.P. Urbach and C. Vuik. A Comparison of enthalpy and temperature methods for melting problems on composite domains. In A. Bermúdez de Castro, D. Gómez, P. Quintela, and P. Salgado, editors, *Numerical Mathematics and Advanced Applications*, Proceedings of ENUMATH 2005, the 6th European Conference on Numerical Mathematics and Advanced Applications, pages 585–592. Springer-Verlag, Berlin Heidelberg, 2006.

- J.H. Brusche, A. Segal and C. Vuik. Towards solving a moving boundary problem within a multi-layered recording stack. Technical report 06-12, Delft University of Technology, 2006.

- J.H. Brusche, A. Segal and C. Vuik. A study of enthalpy methods for mark formation modeling. Technical report 06-04, Delft University of Technology, 2006.

- J.H. Brusche, A. Segal, H.P. Urbach. A finite element model for phase-change recording. *J. Opt. Soc. Am. A*, **22**(4):773–786, 2005.

- J.H. Brusche. Numerical modeling of optical phase-change recording. Technical report 04-04, Delft University of Technology, 2004.

BIBLIOGRAPHY

[1] T. Akiyama, M. Uno, H. Kitaura, K. Narumi, K. Nishiuchi, and N. Yamada. Rewritable dual-layer phase-change optical disk utilizing a blue-violet laser. *Jpn. J. Appl. Phys. Part 1*, 40(3B):1598–1603, 2001.

[2] V. Alexiades and A.D. Solomon. *Mathematical modeling of melting and freezing processes*. Hemisphere Publishing Corporation, 1993.

[3] T. Barth and J.A. Sethian. Numerical schemes for the Hamilton-Jacobi and level set equations on triangulated domains. *J. Comput. Phys.*, 145(1):1–40, 1998.

[4] B. Basu and A.W. Date. Numerical modelling of melting and solidification problems: a review. *Sadhana*, 13(3):169–214, 1988.

[5] M. Bhattacharya, T. Basak, and K.G. Ayappa. A fixed-grid finite element based enthalpy formulation for generalized phase change problems: Role of superficial mushy region. *Int. J. Heat and Mass Transf.*, 45(24):4881–4898, 2002.

[6] H.J. Borg, P.W.M. Blom, B.J.A. Jacobs, B. Tieke, A.E. Wilson, I.P.D. Ubbens, and G. Zhou. AgInSbTe materials for high-speed phase change recording. In *Proceedings SPIE*, volume 3864, pages 191–193, 1999.

[7] H.J. Borg, M. van Schijndel, J.C.N. Rijpers, M. Lankhorst, G. Zhou, M.J. Dekkers, I.P.D. Ubbens, and M. Kuijper. Phase-change media for high-numerical-aperture and blue-wavelength recording. *Jpn. J. Appl. Phys. Part 1*, 40(3B):1592–1597, 2001.

[8] J.M. Brok and H.P. Urbach. Rigorous model of the scattering of a focused spot by a grating and its application in optical recording. *J. Opt. Soc. Am. A*, 20(2):256–272, 2003.

151

[9] J.H. Brusche. The integration of an optical and a thermal model for applications in optical recording. Technical report, Philips Research Laboratories, Eindhoven, the Netherlands, 2002.

[10] J.H. Brusche, A. Segal, and H.P. Urbach. Finite-element model for phase-change recording. *J. Opt. Soc. Am. A*, 22:773–786, 2005.

[11] J.H. Brusche, A. Segal, and C. Vuik. A study of enthalpy methods for mark formation modeling. Technical report 06-04, Delft University of Technology, 2006.

[12] J. Carriere, R. Narayan, W. Yeh, C. Peng, P. Khulbe, L. Li, R. Anderson, J. Choi, and M. Mansuripur. Principles of optical disk storage. In E. Wolf, editor, *Progress in optics*, volume 40, pages 101–102. Elsevier Amsterdam, 2000.

[13] S. Chen, B. Merriman, S. Osher, and P. Smereka. A simple level set method for solving Stefan problems. *J. Comp. Phys.*, 135(1):8–29, 1997.

[14] J. Chessa, P. Smolinski, and T. Belytschko. The extended finite element method (XFEM) for solidification problems. *Int. J. Numer. Meth. Engng.*, 53(8):1959–1977, 2002.

[15] D.L. Chopp. Some improvements of the fast marching method. *SIAM J. on Scientific Computing*, 23(1):230–244, 2001.

[16] C.K. Chun and S.O. Park. A fixed-grid finite-difference method for phase-change problems. *Num. Heat Transf., Part B*, 38(1):59–73, 2000.

[17] J. Crank. *Free and moving boundary problem*. Clarendon Press, Oxford, 1984.

[18] L.A. Crivelli and S.R. Idelson. A temperature-based finite element solution for phase-change problems. *Int. J. Numer. Meth. Engng.*, 23(1):99–119, 1986.

[19] A.J. Dalhuijsen and A. Segal. Comparison of finite element techniques for solidification problems. *Int. J. Numer. Meth. Engng.*, 23(10):1807–1829, 1986.

[20] S.H. Davis. *Theory of solidification*. Cambridge University Press, New York, 2001.

[21] DIFFRACT is a product of MM Research, Inc., Tucson. Its theoretical basis has e.g. been described by M. Mansuripur in: "Certain computational aspects of vector diffraction problems", J. Opt. Soc. Am. A, 6(5):786-805, 1989.

[22] J.P.W.B. Duchateau and B.A.J. Jacobs. Phase-change recording. Internal report M.S. 18.901, Philips Research Laboratories, Eindhoven, the Netherlands, 2001.

[23] C.M. Elliott and J.R. Ockendon. *Weak and variational methods for moving boundary problems*. Pitman Press, Boston, 1982.

[24] V.D. Fachinotti, A. Cardano, and A.E. Huespe. A fast convergent and accurate temperature model for phase-change heat conduction. *Int. J. Numer. Meth. Engng.*, 44(12):1863–1884, 1999.

[25] Z. Fan and D.E. Laughin. Three dimensional crystallization simulation and recording layer thickness effect in phase change optical recording. *Jpn. J. Appl. Phys.*, 42(2):800–803, 2003.

[26] J.W. Goodman. *Introduction to Fourier optics*. McGraw-Hill, New York, second edition, 1998.

[27] Blu-ray Disc Association.
`http://www.blu-raydisc.com`.

[28] ChemiCool.
`http://www.chemicool.com/dictionary.html`.

[29] Gibbs free energy.
`http://xenon.che.ilstu.edu/genchemhelphomepage/topicreview/bp/ch21/gibbs.html`.

[30] HD DVD Promotion Group.
`http://www.hddvdprg.com`.

[31] InPhase.
`http://www.inphase-tech.com/technology/index.html`.

[32] Philips Research Laboratories.
`http://www.research.philips.com/`.

[33] H. Hu and S.A. Argyropoulos. Mathematical modelling of solidification and melting: a review. *Modelling Simul. Mater. Sci. Eng.*, 4:371–396, 1996.

[34] V.S. Ignatowsky. Diffraction by an objective lens with arbitrary aperture. *Trans. Opt. Inst. Petrograd I(IV)*, pages 1–36, 1921.

[35] H. Iwasaki, M. Harigaya, O. Nonoyama, Y. Kageyama, M. Takahashi, K. Yamada, H. Deguchi, and Y. Ide. Completely erasable phase change optical disc II: Application of Ag-In-Sb-Te mixed-phase system for rewritable compact disc compatible with CD-velocity and double CD-velocity. *Jpn. J. Appl. Phys.*, 32(11):5241–5247, 1993.

[36] H. Ji, D. Chopp, and J.E. Dolbow. A hybrid extended finite element/level set method for modeling phase transformations. *Int. J. Numer. Meth. Engng.*, 54(8):1209 – 1233, 2002.

[37] J.B. Judkins and R.W. Ziolkowski. Finite-difference time-domain modeling of nonperfectly conducting metallic thin-film gratings. *J. Opt. Soc. Am. A*, 12(9):1974–1983, 1995.

[38] W.-C. Liu and M.W. Kowarz. Vector diffraction from subwavelength optical disk structures: two-dimensional modeling of near-field profiles, far-field intensities, and detector signals from a DVD. *Appl. Opt.*, 38(17):3787–3797, 1999.

[39] G.S.H. Lock. On the use of asymptotic solutions to plane ice-water problems. *J. of Glaciol.*, 8(53):285–300, 1969.

[40] J.A. Mackenzie and M.L. Robertson. The numerical solution of one-dimensional phase change problems using an adaptive moving mesh method. *J. Comp. Phys.*, 161(2):537–557, 2000.

[41] D.S. Marx and D. Psaltis. Optical diffraction and focused spots and subwavelength structures. *J. Opt. Soc. Am. A*, 14(6):1268–1278, 1997.

[42] E.R. Meinders and H.J. Borg. Numerical analysis of heat diffusion in multilayer phase-change disks. Technical note TN 2000/014 (*Company restricted*), Philips Electronics, 2000.

[43] E.R. Meinders and H.R. Lankhorst. Determination of the crystallisation kinetics of fast-growth phase-change materials for mark-formation prediction. *Jpn. J. Appl. Phys.*, 42(2):809–812, 2003.

[44] E.R. Meinders, M.H.R. Lankhorst, H.J. Borg, and M.J. Dekker. Thermal cross-erasure issues in high-data-density phase-change recording. *Jpn. J. Appl. Phys.*, 40(3):1558–1564, 2001.

[45] E.R. Meinders, A. Mijiritskii, L. van Pieterson, and M. Wuttig. *Optical Data Storage. Phase-change media and recording*, volume 4 of *Philips Research Book Series*. 2006.

[46] E.R. Meinders, M.A. Verheijen, A.V. Mijiritskii, J. Hellmig, M. Kuijper, and J.M. ter Meulen. TEM analysis of mark formation in single-stack and dual-stack Blu-ray Discs. Technical note TN 2002/137 (*Company restricted*), Philips Electronics, 2002.

[47] R. Merle and J. Dolbow. Solving thermal and phase change problems with the eXtended finite element method. *Comp. Mech.*, 28(5):339–350, 2002.

[48] N. Miyagawa, Y. Gotoh, E. Ohno, K. Nishiuchi, and N. Akahira. Land and groove recording for high track density on phase-change optical disks. *Jpn. J. Appl. Phys. Part 1*, 32(11):5324–5328, 1993.

[49] B. Nedjar. An enthalpy-based finite element method for nonlinear heat problems involving phase change. *Computers and Structures*, 80(1):9–21, 2002.

[50] Y. Nishi, T. Shimano, H. Kando, M. Terao, and T. Maeda. Simulations of marks formed on phase-change, land/groove disks. *Jpn. J. Appl. Phys.*, 41(5):2931–2938, 2002.

[51] S. Osher and J.A. Sethian. Fronts propagating with curvature-dependent speed: algorithms based on Hamilton-Jacobi formulations. *J. Comput. Phys.*, 79(1):12–49, 1988.

[52] C. Peng, L. Cheng, and M. Mansuripur. Experimental and theoretical investigations of laser-induced crystallization and amorphization in phase-change optical recording media. *J. Appl. Phys.*, 82(9):4183–4191, 1997.

[53] C. Peng and M. Mansuripur. Thermal cross-track cross talk in phase-change optical disk data storage. *J. Appl. Phys.*, 88(3):1214–1220, 2000.

[54] Numerical Recipes Software. *Numerical recipes in fortran 77: the art of scientific computing*. Cambridge university press, 1992.

[55] B. Richards and E. Wolf. Electromagnetic diffraction in optical systems. II. Structure of the image field in an aplanatic system. *Proc. R. Soc. London A*, 253(1274):358–379, 1959.

[56] D.J. Safarik and C.B. Mullins. Surface phase transformation kinetics: A geometrical model for thin films of nonvolatile and volatile solids. *J. Chem. Phys.*, 117(17):8110–8123, 2002.

[57] S. Senkader and C.D. Wright. Models for phase-change of $Ge_2Sb_2Te_5$ in optical and electrical memory devices. *J. Appl. Phys.*, 95(2):504–511, 2004.

[58] SEPRAN is a finite element package of SEPRA (Ingenieursbureau), Den Haag, the Netherlands. `www.sepra.nl`.

[59] J.A. Sethian. A fast marching level set method for monotonically advancing fronts. *Appl. Math.*, 93(4):1591–1595, 1996.

[60] J.A. Sethian. Fast marching methods. *SIAM Review*, 41(2):199–235, 1999.

[61] J.A. Sethian. *Level Set Methods and Fast Marching Methods*. Cambridge University Press, Cambridge, 1999.

[62] N. Shamsundar. Comparison of numerical methods for diffusion problems with moving boundaries. In D.G. Wilson, A.D. Solomon, and P.T. Boggs, editors, *Moving boundary problems*, pages 165–185, New York, 1978. Academic press.

[63] J. Stefan. Über die Theorie der Eisbildung, insbesondere über die Eisbildung im Polarmeere, Wien. *Akad. Mat. Naturw.*, 98(11a):965–983, 1889.

[64] M. Sussman, P. Smereka, and S. Osher. A level set approach for computing solutions to incompressible two-phase flows. *J. Comput. Phys.*, 114(1):146–159, 1994.

[65] H.P. Urbach and R.T.M. Merkx. Finite element simulation of electromagnetic plane wave diffraction at gratings for arbitrary angles of incidence. In G. Cohen, L. Halpern, and P. Joly, editors, *Mathematical and Numerical Aspects of Wave Propagation Phenomena*, pages 89–99, Philadelphia, 1992. Society of Industrial and Applied Mathematics.

[66] W.A. van Helden. Phase change optical recording, a literature survey. Technical note tn 025/99 (*Company restricted*), Philips Electronics, 1999.

[67] V.R. Voller, C.R. Swaminathan, and B.G. Thomas. Fixed grid techniques for phase change problems: a review. *Int. J. Numer. Meth. Eng.*, 30(4):875–898, 1990.

[68] H.A. Wierenga. Phase-change recording: options for 10 to 20 GB (dual layer, high NA, and blue). In S.R. Kubota, T.D. Milster, and P.J. Wehrenberg, editors, *Optical Data Storage '98*, volume 3401, pages 64–70. The International Society for Optical Engineering, 1998.

[69] E.M. Wright, P.K. Khulbe, and M. Mansuripur. Dynamic theory of crystallization in $Ge_2Sb_{2.3}Te_5$ phase-change optical recording media. *Appl. Opt.*, 39(35):6695–6701, 2000.

[70] N. Yamada, E. Ohno, K. Nishiuchi, and N. Akahira. Rapid-phase transitions of $Ge-Te-Sb_2-Te_3$ pseudobinary amorphous thin-films for an optical disc memory. *J. Appl. Phys.*, 69(5):2849–2856, 1991.

[71] W.-H. Yeh, L. Li, and M. Mansuripur. Vector diffraction and polarization effects in an optical disk system. *Appl. Opt.*, 37(29):6983–6988, 1998.

[72] F. Zijp, M.B. van der Mark, J.I. Lee, C.A. Verschuren, B.H. Hendriks, M.L. Balistreri, H.P. Urbach, M.A. van der Aa, and A.V. Padiy. Near-field read-out of a 50-GB first-surface disc with NA=1.9 and a proposal for a cover-layer-incident, dual-layer near-field system. In B.V.K. Vijaya Kumar and H. Kobori, editors, *Optical Data Storage 2004*, volume 5380, pages 209–223. The International Society for Optical Engineering, 2004.